Simulation and Prediction of North Pacific Sea Surface Temperature

by

Fabian Lienert
M.Sc., ETH Zurich, Switzerland, 2007

A Dissertation Submitted in Partial Fulfillment of the
Requirements for the Degree of

DOCTOR OF PHILOSOPHY

in the School of Earth and Ocean Sciences

Simulation and Prediction of North Pacific Sea Surface Temperature

by

Fabian Lienert
M.Sc., ETH Zurich, Switzerland, 2007

Supervisory Committee

Dr. John C. Fyfe, Co-Supervisor
(School of Earth and Ocean Sciences)

Dr. Andrew J. Weaver, Co-Supervisor
(School of Earth and Ocean Sciences)

Dr. William J. Merryfield, Departmental Member
(School of Earth and Ocean Sciences)

Dr. Dan J. Smith, Outside Member
(Department of Geography)

Supervisory Committee

Dr. John C. Fyfe, Co-Supervisor
(School of Earth and Ocean Sciences)

Dr. Andrew J. Weaver, Co-Supervisor
(School of Earth and Ocean Sciences)

Dr. William J. Merryfield, Departmental Member
(School of Earth and Ocean Sciences)

Dr. Dan J. Smith, Outside Member
(Department of Geography)

ABSTRACT

The first part of this thesis is an assessment of the ability of global climate models to reproduce observed features of the leading Empirical Orthogonal Function (EOF) mode of North Pacific sea surface temperature (SST) anomalies known as the Pacific Decadal Oscillation (PDO). The simulations from 13 global climate models I am analyzing were performed under phase 3 of the coupled model intercomparison project (CMIP3). In particular, I am investigating whether these climate models capture tropical influences on the PDO, and the influences of the PDO on North American surface temperature and precipitation.

My results are that 1) the models as group produce a realistic pattern of the PDO. The simulated variance of the PDO index is overestimated by roughly 30%. 2) The tropical influence on North Pacific SSTs is biased systematically in these models. The simulated response to El Niño-Southern Oscillation (ENSO) forcing is delayed compared to the observed response. This tendency is consistent with model biases toward deeper oceanic mixed layers in winter and spring and weaker air-sea feedbacks

in the winter half-year. Model biases in mixed layer depths and air-sea feedbacks are also associated with a model mean ENSO-related signal in the North Pacific whose amplitude is overestimated by roughly 30%. Finally, model power spectra of the PDO signal and its ENSO-forced component are "redder" than observed due to errors originating in the tropics and extratropics. 3) The models are quite successful at capturing the influence of both the tropical Pacific related and the extratropical part of the PDO on North American surface temperature. 4) The models capture some of the influence of the PDO on North American precipitation mainly due to its tropical Pacific related part.

In the second part of this thesis, I investigate the ability of one such coupled ocean-atmosphere climate model, carefully initialized with observations, to dynamically predict the future evolution of the PDO on seasonal to decadal time scales. I am using forecasts produced by the Canadian climate data assimilation and prediction system employing the Canadian climate model CanCM3 for seasonal (CHFP2) and CanCM4 for decadal (DHFP1) predictions. The skill of this system in predicting the future evolution of the PDO index is then inferred from a set of historical "forecasts" called hindcasts. In this manner, hindcasts are issued over the past 30 years (seasonal), or over the past 50 years (decadal) when they can be verified against the observed historical evolution of the PDO index.

I find that 1) CHFP2 is successful at predicting the PDO at the seasonal time scale measured by mean-square skill score and correlation skill. Weather "noise" unpredictable at the seasonal time scale generated by substantial North Pacific storm track activity that coincides with a shallow oceanic mixed layer in May and June appear to pose a prediction barrier for the PDO. PDO skill therefore depends on the start season of the forecast. PDO skill also varies as a function of the target month. Variations in North Pacific storminess appear to impact PDO skill by means of a lagged response of the ocean mixed layer to weather "noise". In CHFP2, times of increasing North Pacific storm track activity are followed by times of reduced PDO skill, while the North Pacific midwinter suppression of storm track activity with decreasing storminess is followed by a substantial recovery in PDO skill. 2) This system is capable of forecasting the leading 14 EOF modes of North Pacific SST departures, that explain roughly three quarters of the total SST variance. CHFP2 is less successful at predicting North Pacific SSTs, i.e., the combination of all the EOF modes, at the seasonal time scale. 3) Besides the skill in Pacific SST, CHFP2 skillfully predicts indices that measure the atmospheric circulation regime over the

North Pacific and North America such as the Pacific/North American pattern (PNA) (skillful for three out of four start seasons) and the North Pacific index (NPI) (skillful for all four start seasons). 4) CHFP2 is successful at forecasting part of the influence of Pacific SST on North American climate at the seasonal time scale. Measured by 12-month average anomaly correlation skill, in this system the PDO is a better predictor for North American precipitation (skillful for all four start seasons) than temperature (skillful for one out of four start seasons). In CHFP2, ENSO is a better predictor for North American temperature (skillful for all four start seasons) than the PDO. Both ENSO and the PDO are, however, good predictors for North American precipitation (skillful for all four start seasons).

Finally, DHFP1 is less successful at forecasting the PDO at the decadal time scale. Ten-year forecasts of the PDO index exhibit significantly positive correlation skill exclusively in the first year of the forecast. When the correlation skill of the predicted index averaged over lead years is considered, the PDO skill in this system stays significantly positive during the first three years of the decadal forecast. In other words, this climate data assimilation and prediction system is expected to skillfully predict the future three year averaged evolution of the PDO index, but not the evolution of the index in each year individually.

Contents

List of Tables

List of Figures

ACKNOWLEDGEMENTS

I would like to thank John C. Fyfe and William J. Merryfield for all their support and for thoroughly reading this thesis. I would also like to thank all the committee members for their time and effort. I benefited immensely from being a student in the Global Ocean-Atmosphere Prediction and Predictability (GOAPP) network funded mainly by the Canadian Foundation for Climate and Atmospheric Sciences (CFCAS). I would like to thank all the members of the Canadian Centre for Climate Modelling and Analysis (CCCma) seasonal and decadal climate prediction group for the introduction into the field of coupled climate prediction on seasonal and decadal time scales that includes William J. Merryfield, Woo-Sung Lee, George J. Boer, Viatcheslav V. Kharin, John F. Scinocca and Gregory M. Flato. I would like to express my deepest gratitude to William J. Merryfield for his inspiring mentorship and tireless support. I would also like to thank Viatcheslav V. Kharin for his statistical advice. I am grateful to Woo-Sung Lee for producing all the hindcasts I've been using. I would like to thank Mike Berkely for the Linux support. I could not have done this without the continuous support of my family (Cilia Lienert) and all my dear friends.

Chapter 1

Introduction

Climate in the North Pacific varies on seasonal to decadal and longer time scales. At times when warm sea surface temperature (SST) anomalies, defined as departures from the long-term mean, occur along the west-coast of North America cold anomalies usually coincide in the central North Pacific and vice versa. Prominent North Pacific climate variability affects the physical, biological and human environment in both the North Pacific and the adjacent continents (e.g., Latif and Barnett [1994], Mantua et al. [1997], Overland et al. [2010]). When SST is, e.g., anomalously warm in the northeast Pacific ocean biological productivity is generally enhanced along the west coast of Alaska, and reduced towards the south (Mantua et al. [1997]). Part of this North Pacific climate variability is believed to originate in the tropical Pacific. Current Atmosphere-Ocean Global Climate Models (AOGCMs) include the interaction between the ocean and the atmosphere and are therefore potentially capable of simulating North Pacific climate variability.

The international effort on global coupled climate modelling coordinated by the World Climate Research Programme's Coupled Model Intercomparison Project Phase 3 (CMIP3) focused mainly on climate projection on centennial time scales. In CMIP3, which was in support of the IPCC Fourth Assessment Report (IPCC [2007]), AOGCMs simulating the "long-term" response of the climate system to transient forcing should have little memory of the initial state of the experiment. Thus the main goal of CMIP3 was to address the question whether and to what extent external forcings such as greenhouse gases and aerosols impact the long-term trend. CMIP3 did not attempt to predict variability that is internal to the climate system. More recently, however, some groups started to use AOGCMs to forecast future climate on seasonal, interannual and decadal time scales. On these time scales, the variability internal to

the climate system is comparable to or dominates the forced trend itself. In some years, climate departures counteracting the long-term trend can offset the increase in global temperature considerably (Smith et al. [2007]). Seasonal to decadal forecasts of future climate departures are thus crucial for useful climate information for societies and stakeholders in affected regions.

Much like weather forecasting, AOGCMs are carefully initialized with observations up to the start date of each forecast. In this manner, the models are capable of predicting some of the future climate anomalies, especially when close to the initialized state, before the skill vanishes far into the forecast when the memory of the initial state is lost and the model state falls back into its equilibrium (Weisheimer et al. [2009], Dunstone and Smith [2010]).

Recent efforts on improving seasonal, interannual, and decadal prediction using coupled climate models are based on the expectation that including the interaction between the atmosphere and the ocean could impart some predictive skill on these time scales. The ocean has a relatively long memory of past atmospheric forcings, because it responds to it sluggishly. Boundary conditions like sea surface temperature anomalies force the atmosphere, and the atmospheric response in turn can create or destroy SST anomalies. SST anomalies can persist for months and years (Alexander et al. [2002]), and are a potential source of predictability on these time scales (Rowell [1998], Boer [2010]). In CMIP5 (CMIP Phase 5), which is in support of the IPCC Fifth Assessment Report, "near-term" (i.e., decadal) retrospective and future climate forecasts will be part of the core activities to be carried out by the participating modelling groups.

In the North Pacific, the temporal evolution of the pattern of SST anomalies that can explain the largest fraction of the total SST variance (Figures 1.1 and 1.2) is known as the Pacific Decadal Oscillation (PDO) (Mantua et al. [1997]). The PDO is identified by the leading Empirical Orthogonal Function (EOF) mode of North Pacific SST anomalies. The PDO impacts North American climate, in a manner that differs depending on whether El Niño-Southern Oscillation or ENSO and the PDO are in-phase or out-of-phase (Yu and Zwiers [2007]). Theoretical studies indicate that there is a potential for both pentadal (Boer and Lambert [2008]) and decadal climate prediction of surface temperature in the extratropical North Pacific (Boer [2004]). Up to 20% of the next-decade internal climate variance there is potentially predictable (Boer [2010]).

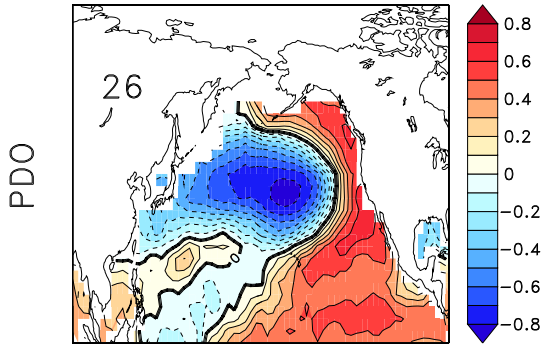

Figure 1.1: Observed linear correlation between the PDO and SST anomalies (HADISST). The percent variance explained is shown in the top left corner.

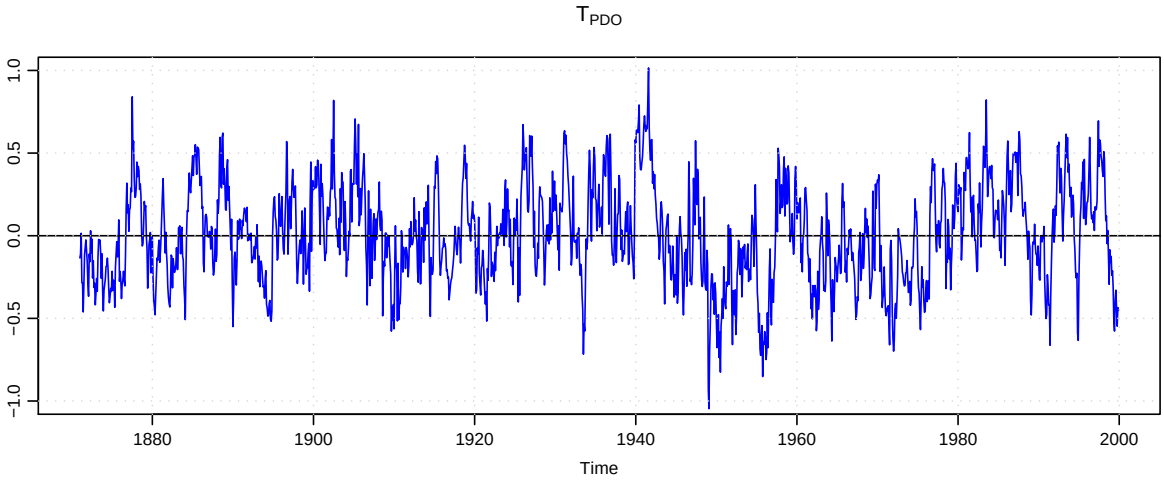

Figure 1.2: Observed evolution of the PDO index (HADISST).

Whatever the causes or the nature of the PDO, the manner in which AOGCMs reproduce observed features of the PDO is likely to affect the skill of climate model predictions on time scales from seasons to decades. In Chapter 2, Section 2.1 of this thesis, I show how realistic the PDO and its part originating in the tropical Pacific are represented in a multi-model ensemble of 13 state-of-the-art CMIP3 climate models. Then in Chapter 2, Section 2.2, I show how realistically these models represent influences of the PDO on North American climate departures. In Chapter 3, I show how skillful the past observed evolution of the PDO is forecast by a seasonal to decadal climate data assimilation and prediction system employing a global climate model that is initialized with observations. Besides, I establish the skill of this system in

predicting the EOF modes of North Pacific SST at the seasonal time scale. Seasonal PDO skill is then compared to seasonal ENSO skill. In addition to the skill in Pacific SST, I investigate the performance of this climate data assimilation and prediction system in forecasting indices that measure the atmospheric circulation regime over the North Pacific and North America such as the PNA and the NPI. Then, the fidelity of this system to predict Pacific SST-related climate departures in North America at the seasonal time scale is established. Finally, the main results are summarized and discussed in Chapter 4.

1.1 The Pacific Decadal Oscillation

I start with a review of the PDO. North Pacific climate variations on decadal and longer time scales has attracted considerable scientific attention over the past 20 years. In 1994, Trenberth and Hurrell [1994] found that atmospheric low pressure systems in the vicinity of the Aleutian islands (Aleutian low) were unusually deep from 1976-1988 compared to the previous and subsequent period. Atmospheric circulation regime shifts tend to alter the spatial distribution of heat content in the ocean. At times when the climatological Aleutian low (i.e., sea level pressure averaged over the winter months) is deeper than the long-term mean state, warmer and moister air is advected poleward along the west-coast of North America thereby warming the ocean while cooler and drier air is advected into the central North Pacific thereby cooling the ocean. Latif and Barnett [1994] described a variation that redistributes upper ocean anomalous heat content across the North Pacific, that takes roughly 20 years to complete in their global climate model. This variation was later defined as the Pacific Decadal Oscillation (PDO), identified by the leading mode of North Pacific sea surface temperature (SST) anomalies, i.e., departures from the long-term mean (Mantua et al. [1997]).

Recent work suggests that the PDO is in part the North Pacific expression of ENSO (Schneider and Cornuelle [2005]), or the ENSO-like pattern of SST variability termed the Interdecadal Pacific Oscillation (IPO) (IPCC [2007]). The PDO might then be a signature of random interdecadal changes in ENSO activity in which case their predictability is thought to be low (Power et al. [2006]). The excitation of low frequency off-equatorial Rossby waves propagating westward is another process which can generate long-term extratropical SST anomalies (Power and Colman [2006]). In a model, the east-west transit time for off-equatorial Rossby waves along 25^o in each

hemisphere is between 16-20 years setting the multidecadal time scale (Meehl and Hu [2006]). These wind-driven Rossby waves have been linked to decadal mega-drought events. In their model, Power and Colman [2006] found simulated sub-surface variability that is predictable on interannual time scales. This includes westward propagating internal Rossby waves within about 25^o of the equator that take up to 4 years to reach the western boundary. However, since this sub-surface predictability is decoupled from the surface which forces the atmosphere, it is of limited use for coupled climate prediction. In 1997, the Gu and Philander [1997] study started the discussion on whether there exists a decadal-scale mechanism that couples the North and tropical Pacific by means of subduction of subtropical waters along the tropical thermocline. However, no such tropical-extratropical coupling mechanism has been found to be significant in the observational dataset (Schneider et al. [1999]).

More recently, Schneider and Cornuelle [2005] report that 80% of the PDO pattern can be reconstructed using an AR1 model by the forcings of Aleutian Low variability, ENSO, and zonal advection anomalies in the Kuroshio-Oyashio-Extension region, and thus was not even a dynamical mode but a combination of forcings. Based on the nature of the individual components of forcings, a statistical forecast of annual mean values of the PDO was possible at a lead time of up to a few years. In a statistical linear inversion model assuming North Pacific variability is a combination of red noise forcings, Newman [2007] reports that annual mean values of North Pacific SST anomalies outside the eastern Subtropics are predictable at a lead time of one year, in the western and northern part of up to two years, respectively.

In a study based on a long equilibrium model integration, some North Pacific decadal variability seems to be internal with only weak connections to the Tropics (Latif [2006]). A multidecadal spectral peak of about 40 years was identified in their model explained by spatial resonance of the full ocean adjustment in response to the variations in the air-sea fluxes. In an earlier study, Latif and Barnett [1994] describe a decadal-scale variation of North Pacific upper ocean heat anomalies due to unstable air-sea interactions between the strength of the subtropical gyre and the Aleutian low. Barnett et al. [1999] set up a series of simulations with different degrees of interaction between the atmosphere and the ocean: an atmospheric model either forced by prescribed SSTs, coupled to an ocean mixed layer column model, or coupled to a dynamic global ocean model. They claim that even in the atmosphere-only case with fixed SSTs where the atmosphere can not feed back on the ocean, there was a PDO-type variability pattern in the atmosphere. The pattern was progressively more

energetic in the mixed-layer-only case, and twice as energetic in the fully-coupled case where the atmosphere is coupled to a global ocean model. Their PDO-type variability pattern in all their model experiments was internal to the North Pacific and not forced by the Tropics because of a lacking model ENSO.

Despite the spectral power on decadal time scales in the North Pacific's leading mode of SST variability, many processes generating extratropical SST anomalies operate on a shorter (e.g., seasonal, interannual) time scale. Anomalous tropical convection induced by ENSO influences global atmospheric circulation and therefore alters surface fluxes over the North Pacific, forcing SST anomalies that peak a few months after the ENSO maximum in tropical east Pacific SSTs (Newman et al. [2003], Alexander et al. [2002]). This atmospheric ENSO response explains up to about half of the variance of January-March mean SST anomalies in the central North Pacific. Changes in net surface heat flux were identified as the dominant process in generating extratropical SST anomalies (Alexander et al. [2002]). Strong and Magnusdottir [2009] recently expanded the conceptual model of the extratropical atmospheric ENSO response and the PDO involving tropospheric Rossby wave breaking (RWB). ENSO forced extratropical atmospheric anomalies can alter the spatial and temporal distribution of RWB directly, via modification of the background flow, and indirectly, via modification of the probability density function of the Pacific/North American teleconnection pattern (PNA). Superposed with RWB anomalies generated by other atmospheric variability patterns, the resulting RWB anomalies integrated anomalous temperature and moisture advection patterns over several months to alter surface heat flux patterns that lead to a PDO-like SST anomaly pattern.

The reemergence mechanism, through which SST anomalies are being decoupled from the surface in summer and reemerge through entrainment into the mixed layer the following winter, indicates that North Pacific SST anomalies have a multiyear memory during the cold season (Alexander et al. [1999], Newman et al. [2003]). The origin of midlatitude SST variability is believed to be due to the fact that the ocean mixed-layer integrates random forcing by weather, approximated as white noise, leading to red noise with increased power at lower frequencies (Frankignoul and Hasselmann [1977]). More recently, it has been proposed that the PDO is not only the result of red noise but also from a reddening of the ENSO signal (Newman et al. [2003]). This simple conceptual model has later been picked up and refined in other studies (Schneider and Cornuelle [2005]). In this framework, a significant part of the PDO is not internal to the North Pacific but forced by tropical variability. In model

simulations controlling the amplitude of atmospheric noise forcing the ocean, Yeh and Kirtman [2004] report that when the noise was reduced, stronger ENSO variance goes with stronger ENSO-PDO correlation. This suggested that local North Pacific internal atmospheric dynamics overwhelms ENSO forcing in the model. Newman [2007] models North Pacific variability as a multivariate red noise process assuming that the forcing is the sum of univariate red noises behaving linearly on interannual time scales. Each noise term was allowed to have its individual decorrelation time scale. Eigenanalysis of the decorrelation time scale matrix using a linear inverse model revealed two propagating eigenmodes with defined periods of 30 and 5 years, respectively. No single eigenmode was identified as the PDO indicating that the PDO represents not a single mode but rather a superposition of different modes acting on different time scales. In this framework on interannual time scales, the ENSO-PDO coherence was suppressed when the Tropics did not force the North Pacific. On decadal time scales, ENSO-PDO coherence was dependent on both tropical and North Pacific forcing. The response of the atmospheric circulation to North Pacific SST anomalies that remotely forces wind stress and SST anomalies in the tropical Pacific is a mechanism that links tropical and North Pacific variability (Vimont et al. [2001]). Based on the PDO review I now introduce the methods used in this study.

1.2 Methodology

1.2.1 Empirical Orthogonal Functions

I begin with a review of Empirical Orthogonal Functions (EOFs) which form part of the methods used in this thesis. EOFs are widely used in climate science to reduce the dimensionality of a dataset. EOFs identify different modes in time-varying geophysical fields such as sea surface temperature at each grid point from observations or global climate models (GCMs) (von Storch and Zwiers [1999], Monahan et al. [2009]). To find the EOFs one first organizes the climate data as a vector $\vec{S}(t)$ and then constructs the covariance matrix, whose elements $C_{i,j}$ are the covariances $\overline{S_i S_j}$ where the overline represents the expected value (i.e., the temporal average) of all the realizations that have been sampled over time. The original data are projected onto the orthogonal eigenvectors of the covariance matrix $C_{i,j}$. By design, the eigenvectors are ranked by the fraction of the total variance that is associated with each of them. An EOF mode consists of a spatial pattern E_m and the time-varying amplitude of

the pattern called a principal component (PC) $p_m(t)$. In an EOF decomposition, a field S in space $\vec{x}$ and time t is equal to the sum of all EOF modes (k is the number of modes)

$$S(\vec{x},t) = \sum_{i=1}^{k} p_i(t) E_i(\vec{x}). \tag{1.1}$$

The temporal covariance between the principal components is zero and hence they are uncorrelated with each other

$$\overline{p_n p_m} = 0 \qquad \text{for} \qquad m \neq n \tag{1.2}$$

where the overbar indicates the average over time. The average of the multiplication of the spatial patterns of the different modes is zero

$$\langle E_n E_m \rangle = 0 \qquad \text{for} \qquad m \neq n \tag{1.3}$$

where the angled brackets indicate the spatial average.

1.2.2 Processing of Climate Forecasts

The 12-month long climate forecasts used in this thesis are started every month from 1979–2008 with an ensemble size of ten. Each ensemble member is initialized with slightly different initial conditions. From these forecasts, monthly mean quantities are considered.

PDO Projection

In this thesis, a predicted PDO time series is derived from the projection of the predicted SST anomaly field onto the pattern of the leading EOF of the observed SST anomaly field (the departure from the long-term monthly mean) in the North Pacific. A linear trend has been removed from the observed SSTs prior to the EOF analysis to ensure, as much as possible, that predictive skill is only due to the predicted internal variability and not due to the signal associated with the well-mixed greenhouse gases. For the prediction of surface temperature, all the ensemble members f_l are averaged

$$f_{EM} = \frac{1}{n} \sum_{l=1}^{n} f_l \tag{1.4}$$

where n indicates the ensemble size and f_{EM} the ensemble mean quantity. For a given year y and forecast month m, the predicted temperature anomaly with respect to the mean of all forecasts in a certain month with the same lead time is defined as

$$[f'_{EM}]_{ym} = [f_{EM}]_{ym} - \overline{f_{EM}}_m \tag{1.5}$$

where the overbar indicates the temporal average over all years. In what follows, "EM" will be dropped and forecast quantities will be understood to be ensemble means thereafter. Considering anomalies with respect to the forecast climatology approximately removes biases intrinsic to the forecast model.

The PDO is defined as the leading EOF of North Pacific SST anomalies. Recalling that a field S in space $\vec{x}$ and time t is equal to the sum of all EOF modes $S(\vec{x},t) = p_1(t)E_1(\vec{x}) + p_2(t)E_2(\vec{x}) + \ldots$, given $E_n(\vec{x})$ observed we can find the predicted PC $p_n(t_{new})$ at a new time t_{new} based on the predicted anomalies $S(\vec{x},t_{new})$ as follows

$$S(\vec{x},t_{new}) = p_1(t_{new})E_1(\vec{x}) + p_2(t_{new})E_2(\vec{x}) + \ldots \tag{1.6}$$

Multiplying both sides by $E_1(\vec{x})$ yields

$$\langle S(\vec{x},t_{new})E_1(\vec{x})\rangle = p_1(t_{new})\langle E_1(\vec{x})E_1(\vec{x})\rangle + p_2(t_{new})\langle E_2(\vec{x})E_1(\vec{x})\rangle + \ldots \tag{1.7}$$

with $\langle E_2(\vec{x})E_1(\vec{x})\rangle$ being zero due to orthogonality, the projection becomes

$$p_1(t_{new}) = \frac{\langle S(\vec{x},t_{new})E_1(\vec{x})\rangle}{\langle E_1^2(\vec{x})\rangle} \tag{1.8}$$

where the angled brackets indicate the spatial average.

1.2.3 Skill Measures

In order to calculate the fidelity of a predicted ensemble-mean quantity, the anomalous predicted values relative to the forecast climatology are usually compared to the anomalous observed values relative to the observed climatology. Recalling that the anomalous predicted quantity $f'_{ym}(t)$ as a function of lead time t from the forecast issued in month m of year y with respect to the mean of all the forecasts issued in month m is defined as

$$f'_{ym}(t) = f_{ym}(t) - \overline{f}_m \tag{1.9}$$

where the overbar indicates the temporal average over all years, $f'_{ym}(t)$ is being verified against the anomalous observed quantity v'_{ym} in month m of year y with respect to the mean observed quantity in month m

$$v'_{ym} = v_{ym} - \overline{v}_m \tag{1.10}$$

where the overbar indicates the temporal average over all years.

In this thesis, I am using three different ways to express forecast quality: standard error, mean-square skill score and anomaly correlation. The standard error provides a dimensional measure of the typical error magnitude. On the other hand, the mean-square skill score is a dimensionless measure of mean square error in relation to that of a "null" climatological forecast. Finally, the dimensionless anomaly correlation bears on the ability of a forecast system to predict the sign of the anomaly.

Standard Error

The standard error $SDE(t)$ gives an estimate of the deviation of the predicted value f' relative to the verification v' from the observational dataset. It is the square root of the mean of the squared differences between corresponding elements of the forecasts and observations. For seasonal forecast skill, e.g., the average standard error over all the forecasts started in month m is

$$SDE_m(t) = \sqrt{\overline{(f'_{ym}(t) - v'_{ym})^2}} \tag{1.11}$$

where the overbar indicates the temporal average over all years. The standard error $SDE(t)$ is the square root of the error variance $EV(t)$, thus $EV(t)$ is defined as

$$EV_m(t) = \overline{(f'_{ym}(t) - v'_{ym})^2} \tag{1.12}$$

where the overbar indicates the temporal average over all years.

Mean-Square Skill Score

The mean-square skill score $MSSS(t)$ for forecasts started in month m can be expressed as

$$MSSS_m(t) = 1 - \frac{EV_m(t)}{EV_{clim}}, \tag{1.13}$$

where EV_m denotes the error variance of the forecast relative to the verification and EV_{clim} the error variance of the "climatological forecast", i.e., a forecast of zero anomaly. The error variance of the "climatological forecast" is

$$EV_{clim} = \overline{(0 - v'_{ym})^2} \tag{1.14}$$

and therefore is equal to the climatological variance

$$EV_{clim} = \overline{(v'_{ym})^2} \tag{1.15}$$

where the overbar indicates the temporal average over all years. A perfect forecast with zero error variance ($EV = 0$) yields an MSSS of 1, a forecast with an error variance as large as the climatological variance ($EV = EV_{clim}$) that provides no more skillful information than inferred from the climatology yields an MSSS of 0. A forecast that is less skillful in terms of error variance than the climatology yields a negative MSSS.

Anomaly Correlation

The anomaly correlation coefficient $AC(t)$ is a measure of the linear relationship between the anomalous predicted quantity and the anomalous verified quantity from the observations. In order to infer seasonal forecast skill for forecasts started in month m, e.g., the anomaly correlation is

$$AC_m(t) = \frac{\overline{f'_{ym}(t)v'_{ym}}}{\sqrt{\overline{(f'_{ym}(t))^2}}\sqrt{\overline{(v'_{ym})^2}}} \tag{1.16}$$

where the overbar indicates the temporal average over all years. For further interpretation regarding signal and noise in climate forecasts see Merryfield et al. [2010].

Chapter 2

The Pacific Decadal Oscillation Represented in Global Climate Models

While model intercomparisons concerning ENSO have been conducted (Achutarao and Sperber [2006], Guilyardi [2006], Merryfield [2006]), only one study has been reported for the PDO (Newman [2007]). Several single-model studies have focused on simulated North Pacific SST variability. In the CCCMA CGCM1, e.g., Yu and Zwiers [2007] find that the PDO was reasonably simulated, and had dominant spectral power from 6 to 15 years. The ECHAM3/LSG CGCM, discussed above, has a robust mode of North Pacific SST variability with a dominant spectral peak at 40 years (Latif [2006]). As discussed in Meehl and Hu [2006], the IPO in the NCAR PCM model shows a PDO pattern that is reasonably simulated. A PDO-type variability appears in the atmosphere and ocean models, discussed above, in earlier versions of the ECHO and the NCAR CCSM models with a spectral peak near 20 years (Barnett et al. [1999]).

In this thesis, the spatial structure of the PDO is identified as in Mantua et al. [1997] with the leading EOF of monthly anomalies of de-trended SST over the North Pacific from 20°N to 65°N. I denote the corresponding normalized principal component that defines the PDO index time series as $T_{PDO}(t)$. Despite its name, the PDO has spectral power not only on decadal and longer, but also on seasonal and interannual time scales. Following Merryfield [2006], the spatial structure of ENSO is similarly described as the leading EOF of monthly anomalies of de-trended SST over

the tropical Pacific from 10°S to 10°N, whose corresponding normalized PC defines an ENSO index time series.

2.1 Tropical Origins of North Pacific Sea Surface Temperature Variability

2.1.1 Introduction

The leading EOF of monthly SST anomalies in the North Pacific, identified with the PDO, indicates that cooler than usual SSTs in the west to central North Pacific often occur in conjunction with warmer than usual SSTs in the northeast Pacific and vice versa. The associated principal component, which defines the PDO index, exhibits prominent variability on decadal to multidecadal time scales as implied by its name, and also across a range of shorter time scales. (I thus refer to such variability as the PDO even when shorter time scales are considered.) It is well known that swings from one phase to another of the PDO index (defined as the associated principal component) can have significant physical, biological, and societal impacts (Mantua et al. [1997], Overland et al. [2010], Schwing et al. [2010]). For example, when the PDO shifts towards its warm phase with anomalously warm temperatures along the west coast of North America, coastal ocean biological productivity is generally enhanced along the west coast of Alaska, and diminished towards the south (Mantua et al. [1997]).

Climate models are increasingly being used to forecast future climate on timescales of seasons to decades. Since the quality of such predictions of the future evolution of the PDO likely depends on the models' ability to represent observed PDO characteristics, it is important that the PDO in climate models be evaluated. A substantial fraction of PDO-related SST variability in the North Pacific is attributable to remote forcing by ENSO variability in the tropical Pacific (Newman et al. [2003], Shakun and Shaman [2009]). This has important implications for the prediction of SST evolution in the North Pacific on seasonal, decadal, and longer time scales (Newman [2007]). The focus of this section is on the ability of global climate models to represent tropical influences on PDO-related SST variability in the North Pacific.

2.1.2 Data and Methodology

The observed monthly mean SST anomalies used in this section are from the HADISST version 1 (Rayner et al. [2003]) dataset for 1871 to 1999. Because of various issues concerning the quality of SST datasets (Deser et al. [2010]), the analysis reported here was repeated using the ERSST version 3b dataset (Smith et al. [2008]), and very similar results were obtained. Results also remain essentially the same whether I use the full record length (of 129 years) or the most reliable data from recent decades. The model data are from the "twentieth century" runs of 13 Atmosphere-Ocean Global Climate Models (AOGCMs) driven with observed greenhouse gas and sulphate aerosol forcing, and in some cases volcanic forcing. From these simulations I extract 129 years of model output to match the observational record. The model simulations are from the Third Coupled Model Intercomparison Project (CMIP3) which was in support of the IPCC Fourth Assessment Report (IPCC [2007]). The models considered are CCCMA-CGCM3.1, CCCMA-CGCM3.1-T63, CNRM-CM3, CSIRO-MK3.0, CSIRO-MK3.5, GFDL-CM2.0, GFDL-CM2.1, INM-CM3.0, IPSL-CM4, MIROC3.2 MEDRES, MIUB-ECHO-G, MRI-CGCM2-3.2A, and NCAR-CCSM3.0. Model documentation can be found at http://www-pcmdi.llnl.gov. Mixed layer depths are computed by applying the algorithm of Kara et al. [2000] to the observed Steele et al. [2001] and modeled monthly ocean climatologies.

By some estimates, it takes about two weeks for the atmosphere to begin to respond to ENSO forcing and to subsequently alter North Pacific surface heat fluxes and influence the ocean mixed layer (Trenberth et al. [1998], Alexander et al. [2002]). On seasonal to interannual time scales, North Pacific SST variability of tropical origin is believed to be dominated by these atmospheric influences, whereas on decadal time scales the dynamical ocean response, such as the advection of zonal temperature anomalies, may also play a role (Schneider and Cornuelle [2005]) but is not considered here. Here, the North Pacific response to ENSO forcing is estimated using an idealized ocean mixed layer model

$$\rho c_p z_m \frac{d}{dt} T_{ENSO}(t) = -\lambda\, T_{ENSO}(t) + F(t) \tag{2.1}$$

where $T_{ENSO}(t)$ denotes the response of North Pacific averaged SSTs to ENSO variability, $\rho c_p z_m$ is the heat capacity of the mixed layer of depth z_m, λ is a feedback parameter describing the damping of ENSO-related SST anomalies, and $F(t)$ is the anomalous flux of sensible and latent heat in the eastern tropical Pacific. The anoma-

lous heat fluxes given by $F(t)$ are obtained in a manner analogous to Thompson et al. [2009] and Fyfe et al. [2010] by 1) subtracting monthly mean SST anomalies over the North Pacific from SST anomalies averaged over the cold-tongue region to form a *difference* cold-tongue index (CTI; the tropical cold-tongue region is defined as 5°N-5°S, 180°-90°W) and 2) multiplying the result by (a) the fractional area of the cold-tongue region (assumed to be 21%) and (b) a coefficient of 10 W m^{-2} K^{-1} (cf. Fig. 17 from Barnett et al. [1991]). Given climatological monthly mean values of z_m and monthly mean values of $F(t)$, then climatological monthly mean values of λ were determined empirically so that the correlation coefficient between $T_{ENSO}(t)$ and $T_{PDO}(t)$ is maximized. Specifically, I assume that $\lambda \approx A + B\sin(2\pi t/12) + C\cos(2\pi t/12)$ and find the constants A, B and C yielding the best correlation coefficients. The mixed layer model was initialized starting in 1871 and the output $T_{ENSO}(t)$ was retained for the period from January 1900 to December 1999.

2.1.3 Results

I now evaluate the ability of the global climate models to reproduce the observed relationship between tropical Pacific forcing associated with ENSO and North Pacific SST variability associated with the PDO. On the time scales considered here, it is reasonable to assume that one of the key elements in this relationship is the climatological depth of the North Pacific mixed layer. In Figure 2.1 I compare the observed (left) and model mean (right) North Pacific mixed layer depth averaged over the winter months when the mixed layer is at its deepest. While the simulated spatial pattern is reasonably realistic, the models as a group clearly overestimate winter mixed layer depth, especially in the west-to-central North Pacific. In what follows I consider the impact of this bias, and others, on the ability of the models to reproduce the timing and magnitude of the North Pacific response to tropical forcing.

Figure 2.2a shows the monthly climatology of observed (red) and model mean (black) mixed layer depth averaged over the North Pacific (i.e. the Pacific Ocean north of 20°N). The models significantly overestimate the observed annual mean z_m, as well as the amplitude of its seasonal cycle. On a month-by-month basis the greatest discrepancy is in February, March and April, when the model mean z_m is about 50% deeper than observed. Another factor to consider is the strength of air-sea feedbacks in the North Pacific, represented in my simplified mixed layer model by the empirically-derived parameter λ. Figure 2.2b shows the observed (red) and model mean (black)

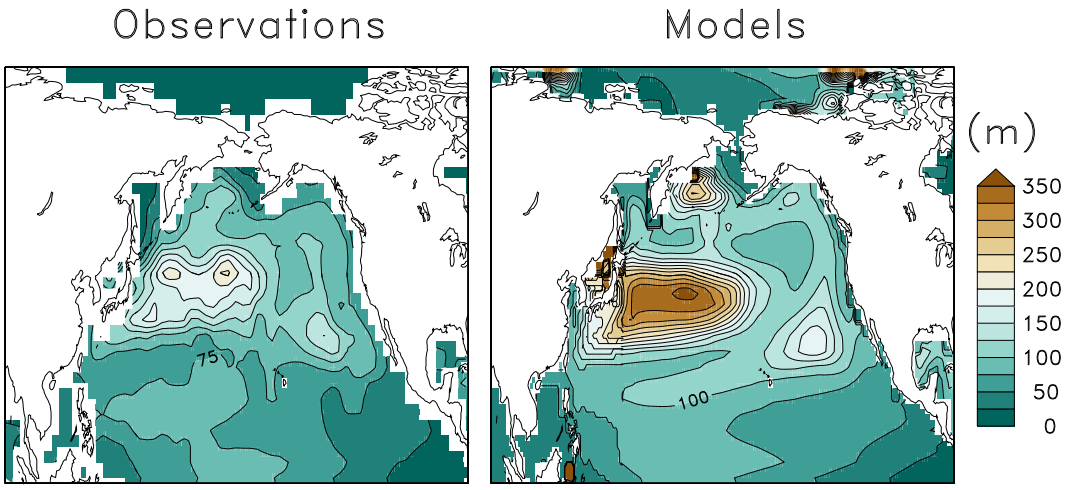

Figure 2.1: Observed (left) and model mean (right) mixed layer depth averaged over the winter months of December, January and February (DJF). Simulated values of mixed layer depth are available for 10 of the 13 models used in this study.

λ. It is reassuring that my empirical approach produces an observed λ variation that is in reasonable accord with previous estimates (cf. Figure 5a from Park et al. [2006], Yu et al. [2009]). Importantly, Figure 2.2b shows that the models on average underestimate the observed air-sea feedbacks throughout the winter half-year.

Another quantity I consider is the coupling parameter $\beta = \lambda/\rho c_p z_m$. Figure 2.2c shows that the combination of weaker feedbacks (λ in the numerator) and deeper mixed layers (z_m in the denominator) produces a model mean β that is significantly underestimated through the winter half-year. Figure 2.2d quantifies the impact of this bias on response time (left axis) and relative magnitude (right axis). Here, response time τ refers to the time lag between the forcing $F(t)$ and the response $T_{ENSO}(t)$, while relative magnitude γ refers to the standard deviation of the response divided by the standard deviation of the forcing scaled to units of temperature, i.e., $\gamma = \sigma(T_{ENSO})/\sigma(F\,\lambda^{-1})$. My estimated observed response time of about 4.6 months is within the range of other estimates (e.g., Newman et al. [2003], Park et al. [2006]). I also note that models with small annual mean β (horizontal axis) tend to have large τ and small γ. These inter-model relationships are consistent with model mean $\tau \approx 6.1 \pm 1.3$ months and $\gamma = 0.6 \pm 0.1$ that are biased high and low, respectively. τ is inferred from the peak of a quadratic fit to the lagged correlation coefficients between $F(t)$ and $T_{ENSO}(t)$. In short, the simulated tropical signals in the North

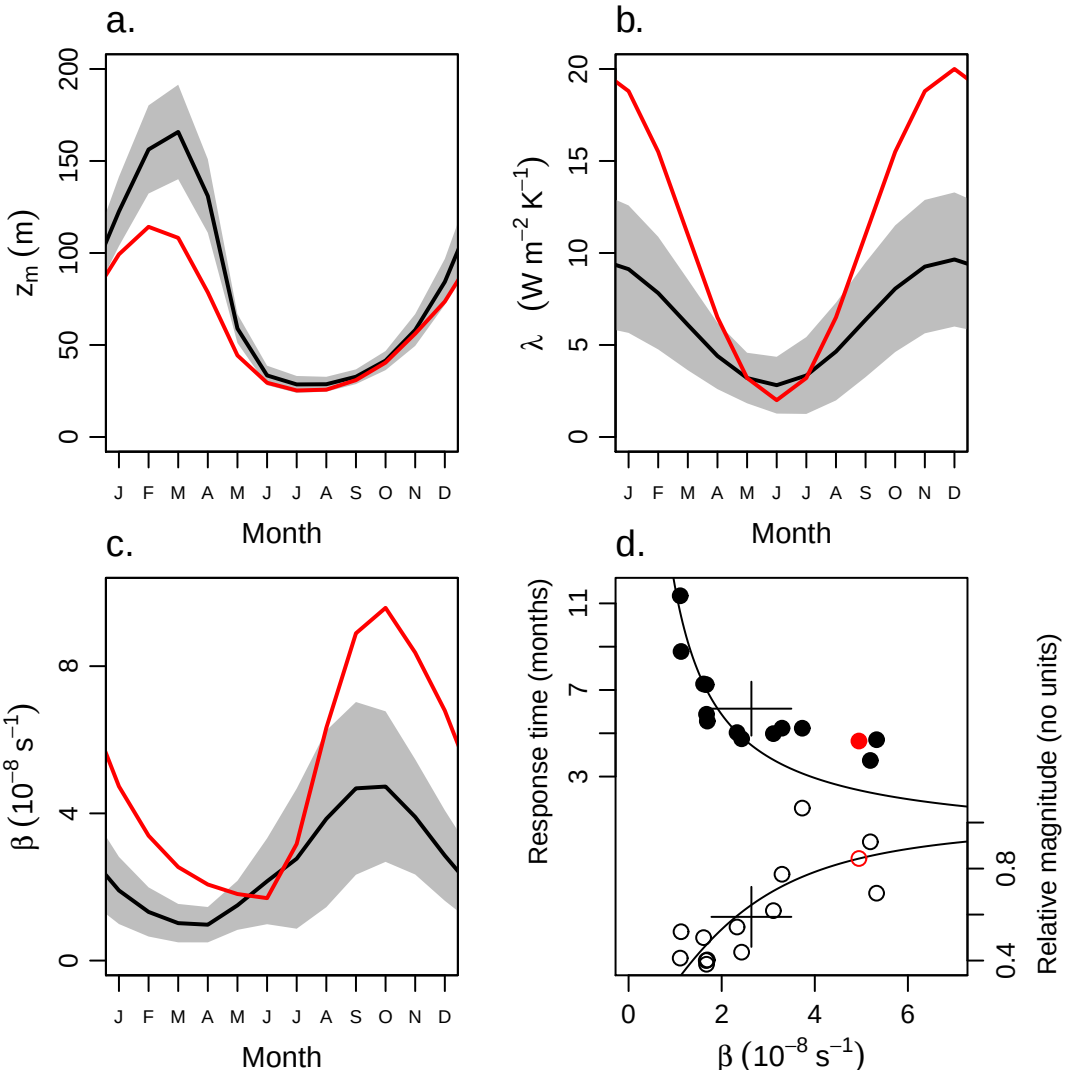

Figure 2.2: Monthly climatology of observed (red) and model mean (black) (a) mixed layer depth averaged over the North Pacific z_m, (b) air-sea feedback parameter λ and (c) coupling parameter $\beta = \lambda/\rho c_p z_m$. Ninety-five percent confidence intervals on the model means are shown with grey shading. (d) Response time (solid circles) and relative magnitude (open circles) as a function of annual mean coupling parameter. Cross-hairs show the 95% confidence intervals for the model mean values. Theoretically-derived values (see text for a detailed description) are shown with black curves.

Pacific tend to be more delayed and of smaller relative magnitude than observed due to the combined effect of mixed layers that are too deep, and air-sea feedbacks that are too weak.

The above relationships can be further understood by considering the mixed layer model with annual mean coefficients, and solutions proportional to $e^{i\omega t}$ where ω represents a single "effective" frequency. In this case analytical solutions to the mixed layer model are available as

$$\tau = \omega^{-1} \tan^{-1}(\frac{\omega}{\beta}) \quad \text{and} \quad \gamma = [1 + (\frac{\omega}{\beta})^2]^{-1/2}. \tag{2.2}$$

The bottom curve in Figure 2.2d was obtained using the known values of γ and β in the second equation to compute a set of ω, and then back-substituting their average into the same equation. The top curve was obtained by substituting the individual ω's and β's into the first equation. These curves illustrate the underlying theoretical relationships that exist between β and the response parameters τ and γ.

I now compare the absolute amplitudes of $T_{PDO}(t)$ and $T_{ENSO}(t)$ in relation to the strength of the ENSO heat fluxes represented by $F(t)$. The observed standard deviations of $T_{PDO}(t)$, $T_{ENSO}(t)$ and $F(t)$ are about 0.30°C, 0.12°C and 1.7 W m^{-2}, respectively. The corresponding model mean values of $T_{PDO}(t)$, $T_{ENSO}(t)$ and $F(t)$ are about 0.34 ± 0.04°C, 0.16 ± 0.04°C and 1.9 ± 0.4 W m^{-2}, respectively. As a group the models overestimate the amplitude of ENSO-related variability in the North Pacific (by about 30%), and thus also the amplitude of the PDO signal (by about 15%). I also note that the model mean amplitude of $F(t)$ is statistically indistinguishable from observed, from which I conclude that the overestimates in the amplitudes of $T_{PDO}(t)$ and $T_{ENSO}(t)$ result from errors intrinsic to the North, rather than tropical, Pacific, e.g., are due to mixed layer depth and air-sea feedback errors. Figure 2.3a, showing the observed and individual model standard deviations as a function of forcing amplitude, suggests a proportionality of about 0.05°C per W m^{-2} between the strength of the ENSO forcing and the amplitude of its North Pacific response. The top curve in Figure 2.3a also indicates that, while ENSO contributes to PDO variability, significant PDO variability occurs independently of ENSO.

Figure 2.3b shows observed (red) and model mean (black) cumulative power spectra $P(f)$, where f is frequency in cycles per year, for $T_{PDO}(t)$ and $T_{ENSO}(t)$. The simulated spectra generally lie above the observed spectra, consistent with our earlier finding that the simulated time series generally contain more variance than the observed time series (see Figure 2.3a). I also note that the simulated $T_{PDO}(t)$ spectra generally flatten towards lower frequencies less rapidly than the observed $T_{PDO}(t)$ spectrum, or other words, the models tend to exhibit a greater proportion of lower

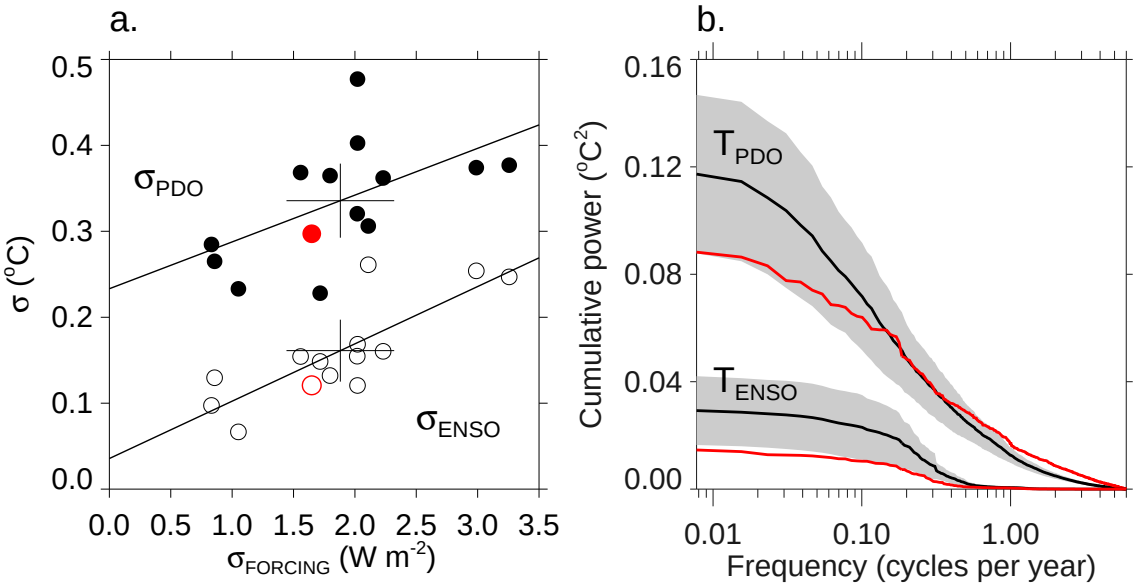

Figure 2.3: a. Standard deviation of the PDO (solid circles) and ENSO-related signals (open circles) as a function of standard deviation of the ENSO forcing. Black circles are for models and red circles are for observations. Cross-hairs show the 95% confidence intervals for the model mean values. Lines are statistically significant (95% confidence level) linear fits to the model values. b. Cumulative power spectra for the PDO and ENSO-related signals. Black curves are for models and red curves are for observations.

frequency variability relative to higher frequency variability than is observed, i.e., the simulated signals are "redder". This is confirmed by noting that the negative slope α of $\log(p(f))$ over the frequency range from 0.02 to 1.0 cycles per year (i.e. periods of 1 to 50 years) is significantly larger in the model mean than for the observations. This is similarly true for the simulated $T_{ENSO}(t)$, from which I infer that the red bias in the simulated $T_{PDO}(t)$ is partly tropical in origin.

The spatial patterns of the observed and modeled SST variability are illustrated in Figure 2.4. The top panels in Figure 2.4 show the observed and model mean patterns of SST associated with the PDO signal, as described by the linear correlation of SST anomalies against $T_{PDO}(t)$. The linear correlation between the observed and simulated patterns is 0.79 for the model mean and 0.67 ± 0.07 for the individual models (over the plotted domain). By these measures the models do a reasonable job of simulating the SST pattern associated with PDO variability. The middle panels of Figure 2.4 show the corresponding patterns associated with the ENSO response

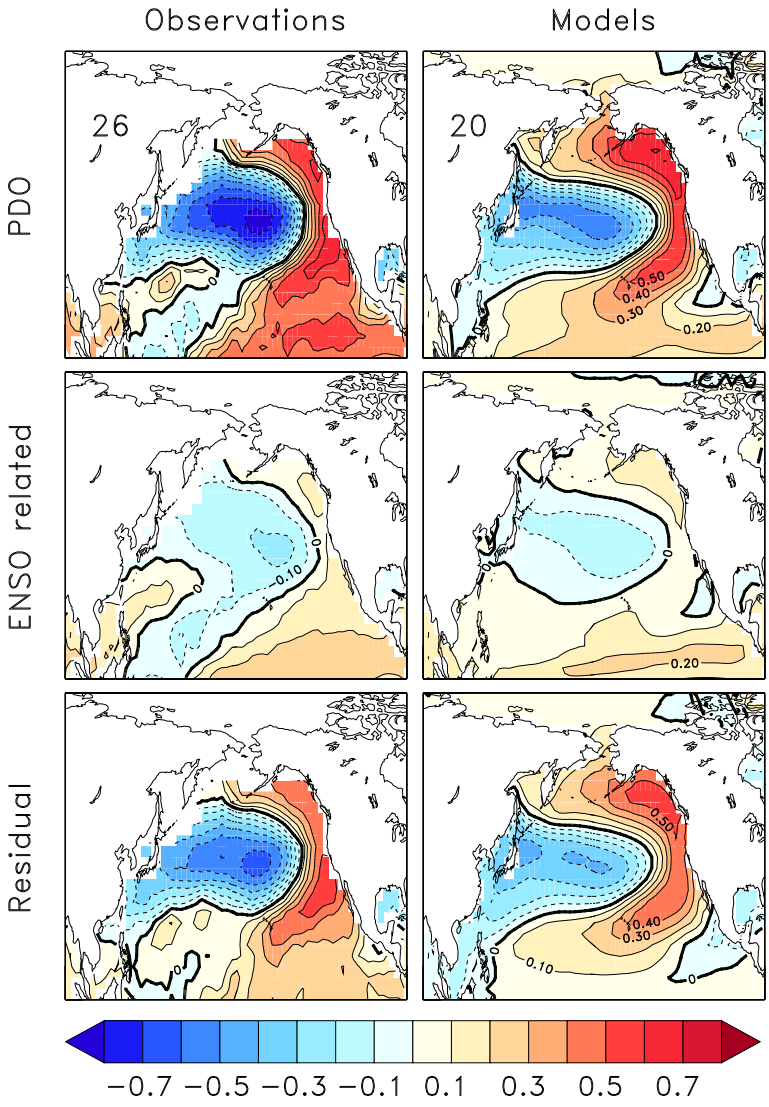

Figure 2.4: (Top) Linear correlation between $T_{PDO}(t)$ and SST anomalies, denoted $r_{PDO,SST}$. The percent variance explained is shown in the top left corner. (Middle) Scaled linear correlation between $T_{ENSO}(t)$ and SST anomalies, denoted $(\sigma_{ENSO}/\sigma_{PDO})\, r_{ENSO,SST}$. (Bottom) Scaled linear correlation between $T_{RES}(t)$ and SST anomalies, denoted $(\sigma_{RES}/\sigma_{PDO})\, r_{RES,SST}$ where $T_{RES}(t) = T_{PDO}(t) - T_{ENSO}(t)$. Note that the top panel is identically the sum of the lower panels.

time series $T_{ENSO}(t)$. Here the linear correlation between the observed and simulated patterns drops to 0.72 for the model mean and 0.60 ± 0.06 for the individual models. Clearly the models are less successful at simulating the ENSO response than the PDO signal itself, in part due to the common tendency in models for SST anomalies to

extend with a single sign across the equatorial Pacific instead of reversing in sign near the Dateline. Finally, the bottom panels of Figure 2.4 show the observed and model mean patterns of SST associated with the residual time series $T_{PDO}(t) - T_{ENSO}(t)$. In this case the linear correlation between the observed and simulated patterns is 0.84 for the model mean and 0.71 ± 0.07 for the individual models, indicating relatively good agreement with observations when the ENSO response is removed from the PDO signal.

2.1.4 Conclusions and Discussion

In this section I have assessed the ability of 13 global climate models to represent the tropical influences on North Pacific SST variability associated with the PDO. I find that the simulated response to ENSO forcing is generally delayed relative to the observed response, a tendency that is consistent with model biases toward deeper oceanic mixed layers and weaker air-sea feedbacks. I also find that the simulated amplitude of the ENSO-related signal in the North Pacific is overestimated by about 30%. Model power spectra of the PDO signal and its ENSO-forced component are redder than observed due to errors originating in the tropics and extratropics.

These results have implications for the ability of climate models to forecast North Pacific variability on seasonal to decadal time scales. Because the simulated North Pacific response lags ENSO unrealistically, seasonal forecasts may tend to exhibit insufficient North Pacific responses to developing El Niño and La Niña events in the first few forecast months. At longer forecast lead times, North Pacific SST anomalies driven by ENSO may tend to be overestimated in models having an overly strong ENSO as the models drift away from observation-based initial conditions and this bias sets in. Finally, the relative preponderance of low frequency variability in the models suggests that climate forecasts may tend to overestimate decadal to multi-decadal variability in the North Pacific.

For reference, variance preserving (i.e., frequency·power) power spectra of the ENSO and PDO time series in the observational dataset and in each CMIP3 model can be found in Figure A.1 in the Appendix. In addition, coherence between the ENSO and the PDO time series as well as their phase spectrum, observed and in each CMIP3 model, can be consulted in the Appendix (Figures A.2, A.3).

2.2 North Pacific Influences on North American Temperature and Precipitation

2.2.1 Introduction

The alignment of atmospheric circulation regimes allows changes in the spatial distribution of surface ocean heat content in the North Pacific to remotely impact climate variability downstream over North America (Latif and Barnett [1994]). Patterns of SST anomalies in the North Pacific can determine where atmospheric Rossby waves transporting energy and moisture into the North American continent are initiated (Yu and Zwiers [2007]). Both anomalous temperature and anomalous precipitation over North America often follow swings in North Pacific SST anomalies associated with the PDO (Cayan et al. [1998], Biondi et al. [2001], Moore et al. [2002], McCabe et al. [2004], Meehl and Hu [2006], Ault and St. George [2010]). For example, a positive PDO phase with warm SST anomalies in the eastern North Pacific can trigger an atmospheric response that often leads to warmer and wetter conditions than usual in the western United States. On the other hand, in the 1950s, e.g., severe droughts in the central and southern Rocky Mountains occurred during a period of a persistently negative PDO (Gray et al. [2003]). The western United States are prone to long-lasting droughts during times when the Interdecadal Pacific Oscillation (IPO), and thus its North Pacific expression the PDO, stays negative (Meehl and Hu [2006]), because a negative PDO phase raises the chances of high sea level pressure systems to form in the North Pacific blocking the advection of moist air into the western United States.

Coupled climate models initialized with observations are being employed to produce seasonal to decadal climate forecasts, the skill of which likely depends on the models' ability to represent observed North Pacific influences, originating in the tropical or North Pacific, on North American climate variability. In this section I report on the ability of climate models to reproduce the observed response of North American temperature and precipitation to the PDO, its ENSO-related and the residual part.

2.2.2 Data

As in the previous section, the observed SSTs used in this section are from the HADISST version 1 (Rayner et al. [2003]) dataset for the period from 1901 to 2000. Because of various issues concerning the quality of SST datasets (Deser et al. [2010]), the analysis reported here was repeated using the ERSST version 3b (Smith et al. [2008]) dataset, and very similar results were obtained. The observed land temperature are from the CRU version 2.1 dataset for the period from 1901 to 2000 (Mitchell and Jones [2005]). The observed land precipitation are from the UDEL-AirT-Precip (Legates and Willmott [1990]) dataset for the period from 1950 to 1999 provided by the NOAA/OAR/ESRL PSD, Boulder, Colorado, USA, from their Web site at http://www.cdc.noaa.gov. The model SST, surface temperature and precipitation data are from the "twentieth century" runs of 13 Atmosphere-Ocean Global Climate Models (AOGCMs) driven with observed greenhouse gas and sulphate aerosol forcing, and in some cases volcanic forcing. The models considered are CCCMA-CGCM3.1, CCCMA-CGCM3.1-T63, CNRM-CM3, CSIRO-MK3.0, CSIRO-MK3.5, GFDL-CM2.0, GFDL-CM2.1, INM-CM3.0, IPSL-CM4, MIROC3.2 MEDRES, MIUB-ECHO-G, MRI-CGCM2-3.2A, and NCAR-CCSM3.0. From these "twentieth century" simulations I extract 100 years of model output for surface temperature and 50 years of model output for precipitation to match the observational record length.

2.2.3 Results

I now assess the ability of the global climate models to capture the observed North American surface temperature and precipitation response to North Pacific SST anomalies that originate in the tropical Pacific, and to North Pacific SST anomalies that are being generated without tropical influences.

North American Temperature Response

The observed and model mean maps of the linear correlation of anomalous North American surface temperature with $T_{PDO}(t)$ are shown in Figure 2.5 (top). The models simulate the observed temperature departures over North America associated with the PDO with a linear correlation between the simulated and observed pattern of 0.90 for the model mean and 0.79±0.04 for the individual models (where the ± refers to the 95% confidence intervals over the multi-model ensemble based on

the Student's t-test). The models therefore capture the pattern of North American temperature departures associated with the PDO reasonably well. The model mean pattern is closer to the observed than any pattern produced by the individual models. In addition, the linear correlation of the observed with the model mean *regression* patterns and the spread among the regression patterns produced by the individual models are roughly the same (shown in the Appendix in Figure A.5, top). By this measure, the models also simulate the magnitude of PDO-related North American temperature anomalies reasonably well.

The observed and model mean maps of the linear correlation of anomalous North American surface temperature with the ENSO-related part of the PDO $T_{ENSO}(t)$ are shown in Figure 2.5 (middle). The linear correlation between the simulated and observed pattern falls to 0.80 for the model mean and 0.66±0.08 for the individual models whose spread is larger than for the PDO correlation pattern (Figure 2.5, top). Regarding the North American surface temperature anomalies associated with the ENSO-related part of the PDO, the linear correlation of the observed with the model mean regression patterns (shown in the Appendix in Figure A.5, middle) and their spread are roughly the same as for the corresponding correlation patterns.

The observed and model mean maps of the linear correlation of anomalous North American surface temperature with the residual part of the PDO $T_{PDO}(t) - T_{ENSO}(t)$ are shown in Figure 2.5 (bottom). Here, the linear correlation between the simulated and observed pattern jumps to 0.91 for the model mean and 0.78±0.05 for the individual models whose spread is smaller than for the $T_{ENSO}(t)$ correlation pattern (Figure 2.5, middle). As for the ENSO-related part of the PDO, the linear correlations for the regression patterns of the residual part of the PDO $T_{PDO}(t) - T_{ENSO}(t)$ (shown in the Appendix in Figure A.5, bottom) and their spread are roughly the same as for the corresponding correlation patterns.

The influence of the PDO on anomalous temperature over North America with warm anomalies often occurring in the north west and cold anomalies in the south east are the sum of both the north-south contrast in the ENSO-related and east-west contrast in the residual PDO influence. The CMIP3 models are capable of reproducing this observed relationship including the magnitude (inferred from the regression patterns) reasonably well.

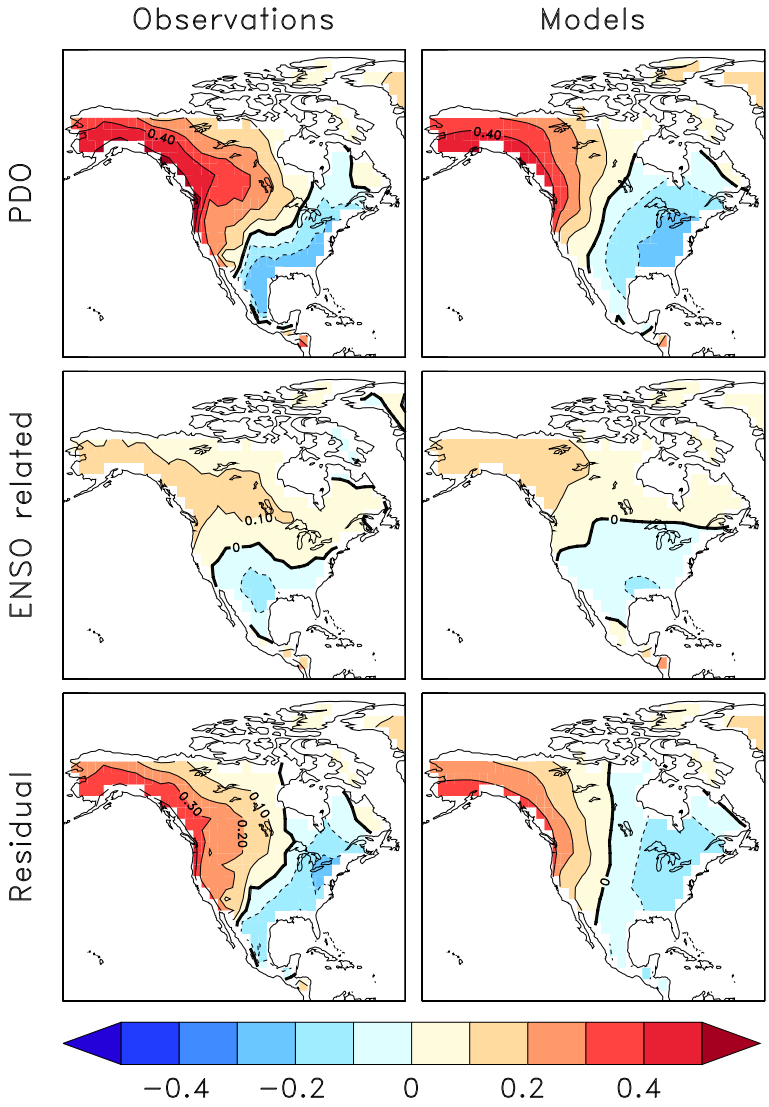

Figure 2.5: Linear correlation between $T_{PDO}(t)$ and anomalous surface temperature, $r_{PDO,ST}$ (top). Scaled linear correlation between $T_{ENSO}(t)$ and anomalous surface temperature, $(\sigma_{ENSO}/\sigma_{PDO})r_{ENSO,ST}$ (middle). Scaled linear correlation between $T_{RES}(t)$ and anomalous surface temperature, $(\sigma_{RES}/\sigma_{PDO})r_{RES,ST}$ where $T_{RES}(t) = T_{PDO}(t) - T_{ENSO}(t)$ (bottom). Note that the top panel is identically the sum of the lower panels.

North American Precipitation Response

The observed and model mean maps of the linear correlation of anomalous precipitation with the PDO $T_{PDO}(t)$ over North America are shown in Figure 2.6 (top). The models simulate the observed North American precipitation variability associated with the PDO with a linear correlation between the simulated and observed

pattern of 0.21 for the model mean and 0.11±0.08 for the individual models. The model mean correlation pattern is again closer to the observed than any pattern simulated by the individual models. In this case, the linear correlation of the observed with the model mean regression patterns (shown in the Appendix in Figure A.6, top) is 0.23 and 0.13±0.06 for the individual models. Certainly, the models are not successful at reproducing all the complex smaller-scale features evident in the observed PDO precipitation response pattern. However, the models do capture some of the larger-scale features of the pattern and, to a greater degree, some of the magnitude (inferred from the regression patterns) of the observed North American precipitation response to the PDO reasonably well.

The observed and model mean maps of the linear correlation of anomalous precipitation over North America with the ENSO-related part of the PDO $T_{ENSO}(t)$ are shown in Figure 2.6 (middle). Here, the linear correlation between the simulated and observed pattern increases to 0.25 for the model mean and 0.18±0.08 for the individual models. The models reproduce the observed pattern of anomalous North American precipitation regressed onto the ENSO-related part of the PDO (shown in the Appendix in Figure A.6, middle) with a linear correlation of 0.41 for the model mean and 0.26±0.04 for the individual models.

The observed and model mean maps of the linear correlation of anomalous precipitation with the residual part of the PDO $T_{PDO}(t) - T_{ENSO}(t)$ over North America is shown in Figure 2.6 (bottom). In this case, the linear correlation between the simulated and observed pattern falls to 0.04 for the model mean and 0.00±0.10 for the individual models. The models capture the observed pattern of anomalous North American precipitation regressed onto the residual part of the PDO (shown in the Appendix in Figure A.6, bottom) with a linear correlation of 0.01 for the model mean and 0.00±0.07 for the individual models. By this measure, the models perform worst for anomalous North American precipitation associated with the residual PDO. The model mean pattern of the magnitude of the precipitation response does not fare systematically better than the individual patterns.

In summary, the models capture the larger-scale structure of the correlation pattern between North American precipitation variability and the PDO as well as its magnitude (inferred from the corresponding regression patterns) reasonably well. Some model biases arise from the model's obvious inability to resolve and reproduce the smaller-scale structures seen in the observed correlation pattern. In addition, systematic biases in the simulated precipitation variability over North America associated

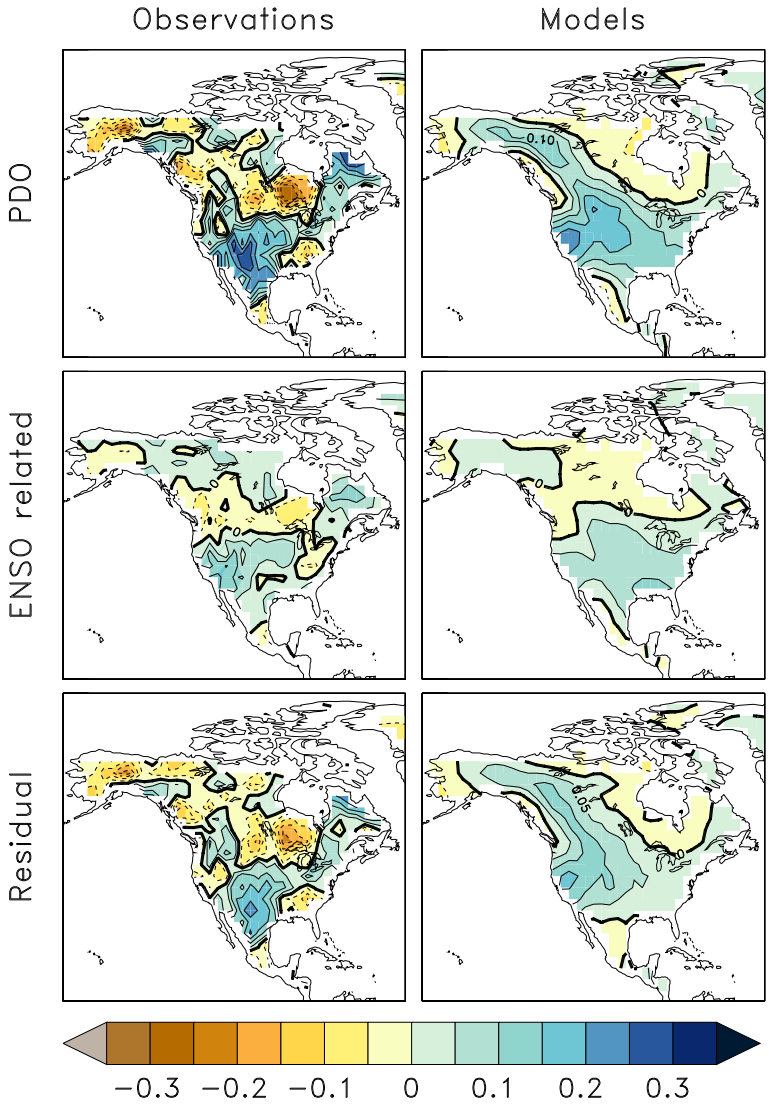

Figure 2.6: As Figure 2.5, but for anomalous precipitation.

with the PDO are in part due to the fact that the models are less successful at simulating the precipitation variability associated with the residual part of the PDO than the ENSO-related part. For example, times when the PDO is in positive phase with warm SST anomalies along the west-coast of North America that were caused by an El Niño often coincide with times of precipitation above the long-term average in the south western United States (Figure 2.6, middle), a relationship that is captured by the models. In this region, positive PDO phases not caused by tropical influences, however, often coincide with times of below average precipitation in the observational

dataset. This observed relationship is obviously not reproduced by the models (Figure 2.6, bottom).

2.2.4 Conclusions and Discussion

In this section, I have investigated the fidelity of global climate models to reproduce observed influences of North Pacific SST on North American surface temperature and precipitation. The models represent North American temperature departures associated with the PDO, its part originating in the tropics as well as in the extratropics seen in the observations reasonably well. They are not very successful at capturing the observed smaller-scale features of North American precipitation departures associated with the PDO. However, the models realistically reproduce some larger-scale features of the influence of the PDO exclusively due to its tropical Pacific-related part on North American precipitation.

Obviously, the individual models perform worse on average and with an enhanced range of success at representing the pattern and magnitude of the North American temperature response to the ENSO-related part of the PDO. In Figure 2.5 (middle), the warm anomaly associated with the North Pacific ENSO response, e.g., extends farther east into the continent in the observations than is simulated by the models adding to the model bias in the temperature anomaly pattern associated with the PDO. Part of this model bias might arise from an unrealistic spatial pattern of the response of North Pacific SST to ENSO in the models that could modify their atmospheric Rossby wave trains and thus temperature variability over North America downstream (Trenberth et al. [1998]).

Chapter 3

The Prediction of the Pacific Decadal Oscillation

In this chapter, I am addressing the question how skillfully the PDO is predicted by a seasonal to decadal coupled climate prediction system that has been carefully initialized with observations. I am using forecasts from the second Canadian Centre for Climate Modelling and Analysis (CCCma) coupled climate data assimilation and prediction system (CHFP2) which is an improved version of the system employed in the Coupled Historical Forecasting Project (CHFP1) (Merryfield et al. [2010]). Besides numerous other improvements, simple SST nudging initialization has been replaced by nudging of SST and sea ice together with an ocean data assimilation procedure for three-dimensional temperature and salinity with atmospheric and land surface initial conditions based on synoptic data. Therefore the entire coupled system including ice, land, atmosphere, and the ocean is initialized after assimilating numerous observational datasets. The predictive skill of CHFP2 is quantified by retrospective forecasts (referred to as "hindcasts") of the past 30 years. Each month from 1979–2008, an ensemble of ten hindcasts are started from different ocean/atmospheric initial conditions. In addition, I am using decadal hindcasts from CCCma's first Decadal Historical Forecasting Project (DHFP1) whose ten ensemble members are initialized every 5 years starting on January 1st 1961. A prediction is considered skillful if the MSSS or anomaly correlation skill is significantly positive on a 95% confidence level using the bootstrap. These extensive sets of retrospective forecasts allow for a thorough assessment of the ability of this seasonal to decadal climate prediction system to predict the future evolution of the PDO in an operational deployment.

3.1 Models and Experiments

3.1.1 Models

CCCma's contributions to World Climate Research Programme's CHFP seasonal prediction experiment and to the decadal prediction component of CMIP5 comprise forecasts from two models: CanCM3 couples the atmospheric model CanAM3 (T63 horizontal spectral resolution, approximately 220 km in longitude by 310 km in latitude in the midlatitudes, with 31 vertical levels) used for CMIP3 to a new ocean model CanOM4 (1.4° by 0.94° horizontal resolution, with 40 vertical levels). CanCM4 couples CanOM4 to a new atmospheric model CanAM4 (T63 horizontal spectral resolution with 35 vertical levels). The earth-system version of CanCM4, which includes coupled climate carbon interactions, forms the basis for CCCma's contribution to the climate change simulation component of CMIP5. CanCM3 includes basic time-dependent radiative effects of greenhouse gases and aerosols whereas CanCM4 incorporates a more complete treatment including solar and volcanic forcing. Both models exhibit improved ENSO-like variability in freely running simulations compared to the model version used for CMIP3, with typical amplitudes moderately less than observed in CanCM3, and moderately greater than observed in CanCM4. In this thesis, I am using CCCma's seasonal (12 months) retrospective forecasts from CanCM3, and decadal (10 years) retrospective forecasts from CanCM4.

3.1.2 Initialization

Seasonal Prediction

The assimilation of observational datasets for CCCma's seasonal (CHFP2) predictions is done in multiple steps as sketched in Figure 3.1. A full-field data assimilation strategy is used which aims at initializing the coupled model with the true observed values rather than anomalies. The initialized model state is therefore close to the observed state not the model attractor, i.e., the state of the freely running model. In order not to shock the coupled model, a long spinup run is performed while relaxing the model state to the observed state. The initial conditions for the forecasts are generated by an ensemble of coupled assimilation runs. The CanCM3-based assimilation runs begin in 1948 from initial conditions drawn from different years of two CanCM3 control runs. Each such run assimilates 6-hourly atmospheric winds, temperatures

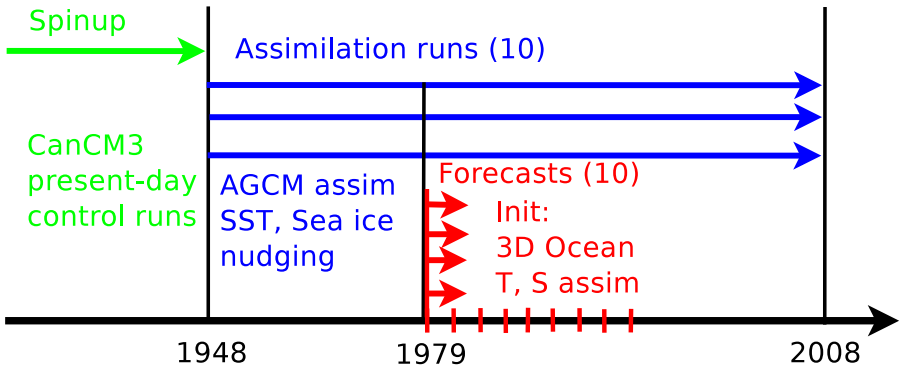

Figure 3.1: Observational data assimilation strategy for CHFP2.

and moistures from the NCEP reanalysis (Kalnay et al. [1996]) and ERA (Uppala et al. [2005]) (ERA40 and ERA interim) reanalyses thereafter on synoptic scales using a constant incremental nudging (CIN) procedure. SST is relaxed to ERSST (Smith et al. [2008]) values (before 1981) or weekly OISST V2 (Reynolds et al. [2002]) (1981 to present) values. Sea ice concentration is relaxed to the monthly HadISST dataset (Rayner et al. [2003]). Then before 12 month long forecasts are issued (from 1979 and onwards), the three-dimensional ocean temperatures from the monthly Global Ocean Data Assimilation System (GODAS) analysis are assimilated into the model following the method of Tang et al. [2004], with a subsequent salinity adjustment following the method of Troccoli et al. [2002].

Decadal Prediction

The DHFP1 hindcasts I am using here are similarly initialized as in CHFP2, except that the CanCM4-based assimilation runs begin in 1958 from initial conditions drawn from different years of a long (roughly 350 year) spinup run. In addition, no three-dimensional ocean temperatures are assimilated before the start of the forecast. However, in DHFP1 the ocean contains a memory of the history of atmospheric assimilation and SST. In contrast to CHFP2, in DHFP1 volcanic activity and its associated aerosol forcing is prescribed as observed.

3.2 Seasonal prediction

The response of the atmosphere to SST departures in the Pacific remotely influences climate over North America. In this section, I therefore begin with an evaluation

of the CHFP2 predictive skill in Pacific SST. Then, the performance of this system to forecast the evolution of atmospheric circulation regimes over the Pacific ocean and North America is assessed. Finally, I establish the skill of CHFP2 to forecast the influence of Pacific SST on temperature and precipitation departures over North America.

3.2.1 PDO

For the seasonal hindcasts from CHFP2 covering the period from 1979–2008, Figures 3.2, 3.3 and 3.4 (left) show the SDE, MSSS and AC of the PDO prediction as a function of lead time (0–11 months) for forecasts initialized on March 1st (03), June 1st (06), September 1st (09) and December 1st (12), respectively. The solid lines indicate the estimates of the mean skill measures over all the forecasts started in years 1979–2008. The mean skill measures are accompanied by a bootstrapped 95% confidence interval (dashed lines) estimating the uncertainty of the skill estimates that stems from forecasting the PDO in different years. In each plot, the dots and error bars on the right show the mean skill estimate and its 95% confidence interval over the 12-month of forecast range. The former are summarized in Tables 3.1, 3.2 and 3.3. The PDO skill measures as a function of calendar month are shown in Figures 3.2, 3.3 and 3.4 (right). For the SDE *low* scores indicate a skillful forecast, while for the MSSS and AC *high* scores indicate a skillful forecast.

It is evident that the PDO prediction standard error growth with lead time is systematically reduced for forecasts started in June (red) compared to forecasts started in March (blue), September (green) or December (yellow). For the SDE averaged over the 12-month forecast range (Table 3.1), this difference is statistically significant (Figure 3.2, left) when the SDE of forecasts started in June (0.23) is, e.g., compared to the SDE of forecasts started in March (0.27).

The fidelity of CHFP2 to forecast North Pacific SST departures associated with the PDO measured by the MSSS (Figure 3.3) is significantly positive for all forecast start months (March, June, September, December) when averaged over the seasonal forecast range. The discussed reduced error growth for June started PDO forecasts relative to those in all other months is reflected in the variance measure MSSS. Here, forecasts initialized in June exhibit a significantly higher 12-month mean MSSS (0.36) than in March (0.12) (Table 3.2). The MSSS of PDO forecasts started in June stays significantly above zero during six months until lead month five (November). The fact

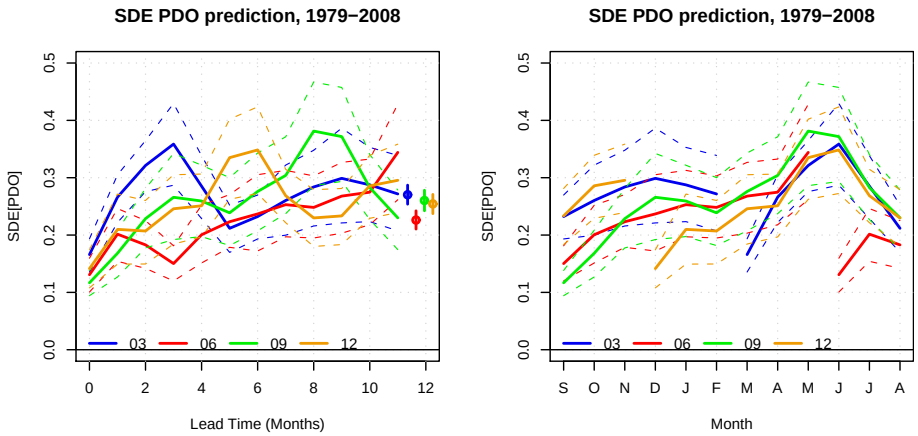

Figure 3.2: SDE (solid lines) and bootstrapped 95% confidence interval (dashed lines) between the predicted and the observed PDO index as a function of lead time where the dots, lines on the right show the mean, 95% confidence interval over the forecast range (left panel) and target month (right panel) for four different start months of the forecast (03: March; 06: June; 09: September; 12: December).

that the evolution of the MSSS drops rapidly to values below 0.5 over the course of a forecast, but remains positive is due to an underestimated variance of the predicted signal relative to the observed variance (on average roughly 37% of the observed PDO variance). The observed PDO variance is 0.09, while in CHFP2 forecasts the PDO variance is 0.04 ± 0.02 (March initialized), 0.03 ± 0.01 (June initialized), 0.03 ± 0.02 (September initialized) and 0.03 ± 0.02 (December initialized) where the $\pm$ refers to the 95% confidence intervals over the ensemble members based on the Student's t-test.

CHFP2 is relatively successful at predicting the sign of PDO associated North Pacific SST departures as indicated by the AC scores (Figure 3.4). CHFP2 AC skill is not affected by variance bias, unlike the MSSS. The correlation skill of CHFP2 to forecast the PDO is significantly positive for all start months when their skill is averaged over the 12-month forecast range. They are close to the estimate by Newman [2007] from an empirical model that is comparable or better than persistence in predicting North Pacific SSTs (except in the south-eastern part). As for the MSSS, correlation skill (Table 3.3) is significantly higher for the most skillful forecast ini-

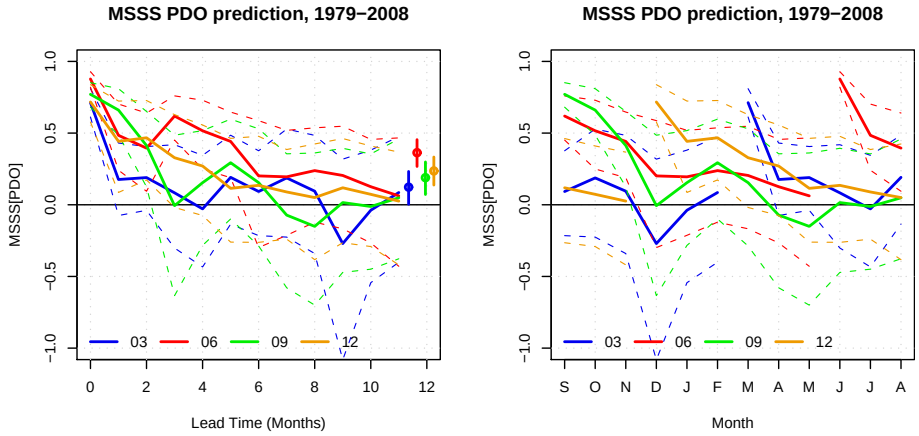

Figure 3.3: MSSS (solid lines) and bootstrapped 95% confidence interval (dashed lines) between the predicted and the observed PDO index as a function of lead time where the dots, lines on the right show the mean, 95% confidence interval over the forecast range (left panel) and target month (right panel) for four different start months of the forecast (03: March; 06: June; 09: September; 12: December).

tialized in June (0.58) than for the least skillful forecast initialized in March (0.42). A PDO forecast started in June stays significantly above zero correlation skill up to lead month ten, before the AC is no longer statistically distinguishable from zero in the last month of the forecast.

The difference in CHFP2 fidelity of June versus March initialized forecasts may be in part due to a PDO prediction barrier in May and June. The SDE in predicting the PDO as a function of month for all four start months of the forecast is shown in Figure 3.2 (right). In this Figure, the standard error peaks in May and June for forecasts initialized in March, September and December. Forecasts initialized after or during this PDO prediction barrier in May and June benefit from smaller standard error growth and therefore a better MSSS and AC (Figures 3.3, 3.4, right).

Impact of Storminess on PDO Variance

Along with the SDE growth of PDO forecasts, the annual cycle of the observed PDO variance shown in Figure 3.5 peaks in May and June as well. CHFP2 forecasts obviously fail to predict a substantial part of the PDO signal when the observed PDO

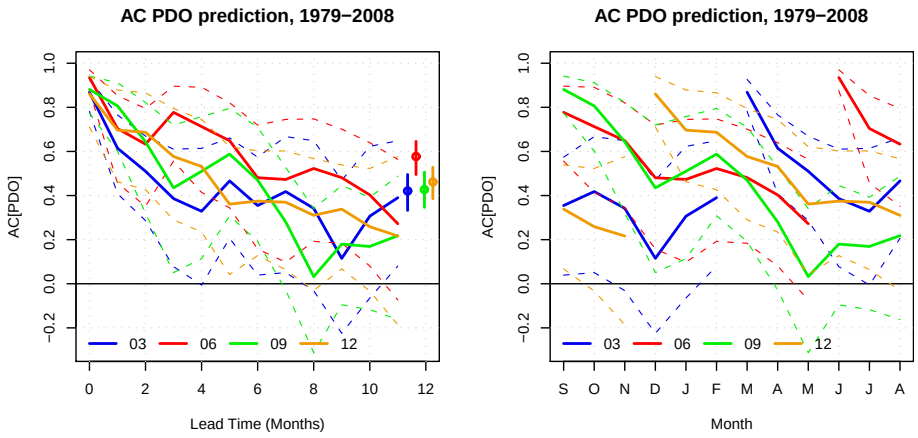

Figure 3.4: AC (solid lines) and bootstrapped 95% confidence interval (dashed lines) between the predicted and the observed PDO index as a function of lead time where the dots, lines on the right show the mean, 95% confidence interval over the forecast range (left panel) and target month (right panel) for four different start months of the forecast (03: March; 06: June; 09: September; 12: December).

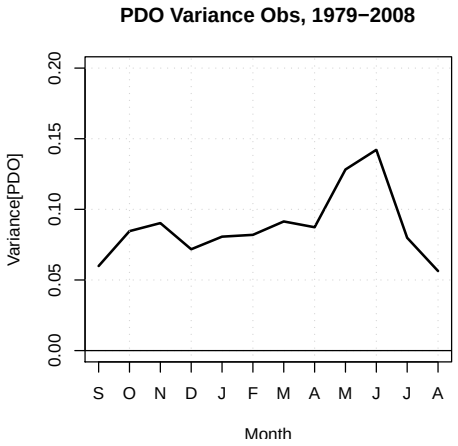

Figure 3.5: Observed variance of the PDO index.

variance is enhanced. A likely explanation for this phenomenon is that part of the enhanced PDO variance in May and June is generated by atmospheric weather "noise" unpredictable at the seasonal time scale. In the observation-based ERA40/ERA

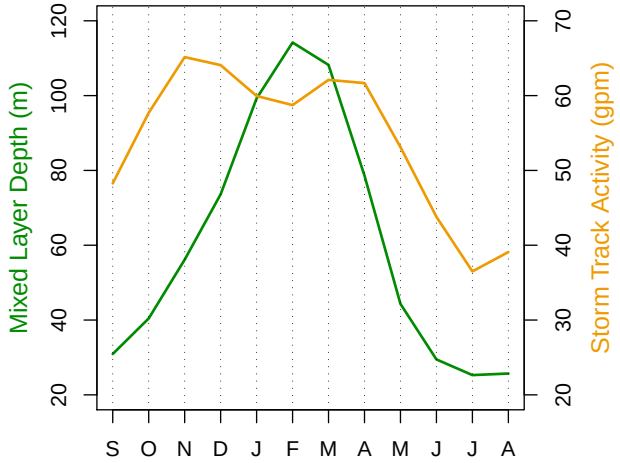

Figure 3.6: Observed North Pacific mixed layer depth (green), ERA40/ERA interim North Pacific storm track activity (yellow).

interim dataset, the annual cycle of North Pacific weather "noise", inferred from the storm track activity based on the standard deviation of band-pass filtered (retaining periods between 2.5 and 8 days) 500 hPa geopotential height data (yellow line in Figure 3.6) reaches its minimum in July. The still substantial amount of atmospheric weather "noise" in May and June coincides with an relatively shallow North Pacific mixed layer (green line in Figure 3.6) whose ability to integrate atmospheric variability is minimal. I also note that, the PDO prediction barrier occurs one to two months after the ENSO-prediction barrier (Saha et al. [2006]).

For reference, maps of monthly mean North Pacific mixed layer depth for the CMIP3 version of the Canadian climate model (left), the observations (middle) and the difference between the model and observations (right) can be found in Figure A.4 in the Appendix.

Impact of Midwinter Suppression on PDO Skill

Another apparent feature in CHFP2's PDO skill measures (Figures 3.2, 3.3, 3.4, right) is the sudden rise in standard error and drop in MSSS and correlation skill, e.g., in December and their recovery thereafter. The MSSS and AC for forecasts initialized in March, September and, to a lesser extent, June, e.g, reach local minima in December (Figures 3.3, 3.4, right). The December drop in MSSS is significant for March (blue)

Table 3.1: Mean SDE over 12-month forecast range indicated by the overbar for the PDO, North Pacific SSTs (K), ENSO, NINO3.4 prediction (K).

Month	$\overline{SDE}$ PDO	$\overline{SDE}$ NP SST	$\overline{SDE}$ ENSO	$\overline{SDE}$ NINO3.4
03	0.27	0.66	0.39	0.63
06	0.23	0.64	0.30	0.51
09	0.26	0.64	0.27	0.49
12	0.25	0.63	0.36	0.61

Table 3.2: Mean MSSS over 12-month forecast range indicated by the overbar for the PDO, North Pacific SSTs, ENSO, NINO3.4 prediction.

Month	$\overline{MSSS}$ PDO	$\overline{MSSS}$ NP SST	$\overline{MSSS}$ ENSO	$\overline{MSSS}$ NINO3.4
03	0.12	0.03	0.44	0.45
06	0.36	0.04	0.66	0.61
09	0.19	0.05	0.61	0.51
12	0.24	0.13	0.40	0.33

Table 3.3: Mean AC over 12-month forecast range indicated by the overbar for the PDO, North Pacific SSTs, ENSO, NINO3.4 prediction. Mean partial AC (AC_p) over 12-month forecast range indicated by the overbar for the PDO prediction with the ENSO-related part removed.

Month	$\overline{AC}$ PDO	$\overline{AC}$ NP SST	$\overline{AC}$ ENSO	$\overline{AC}$ NINO3.4	$\overline{AC_p}$ PDO
03	0.42	0.28	0.66	0.68	0.38
06	0.58	0.30	0.79	0.78	0.52
09	0.43	0.28	0.76	0.73	0.38
12	0.46	0.34	0.62	0.62	0.43

initialized forecasts if their 95% confidence interval two months earlier in October is taken as a benchmark. In this case, the MSSS in December is outside its 95% confidence interval two months earlier in October.

I argue that this sudden drop and recovery in skill is associated with the climatological baroclinic wave activity in the North Pacific that is maximal in November, suppressed in January and February and then maximal in March and April (Nakamura [1992]). It is well known that AGCMs are able to reproduce this behaviour of North Pacific storm track activity reasonably well (e.g., Christoph et al. [1997]).

It has recently been argued that the reduction of the number and the amplitude of the disturbances entering the North Pacific from midlatitude Asia is the cause for a midwinter suppression in storminess over the western and central North Pacific downstream (Penny et al. [2010]).

In order to verify whether CHFP2 is reproducing this observed midwinter suppression, I have applied a recursive band pass filter to extract signals with periods between 2.5 and 8 days in the daily geopotential height at 500 hPa for each grid point for all June and December initialized forecasts (from 1979–2008). Following Christoph et al. [1997] the measure for the storm track activity is then taken as the standard deviation of a 31-day moving window of band-pass filtered data. As shown in Figure 3.7 (bottom), daily storm track activity in CHFP2 is suppressed in January and February in the North Pacific for forecasts started in June (left) and for those started in December (right). In this model, North Pacific storminess increases in October reaching a first local maximum in late November/early December followed by a period of suppressed storminess in late January/early February and subsequently a period of enhanced storminess that peaks in late May and ends in April.

To investigate how realistically CHFP2 is capturing the seasonal cycle of North Pacific storminess, the discussed filtering procedure has also been applied to ERA40/ERA interim reanalysis data for all the years in which CHFP2 forecasts have been initialized. Compared against storm track activity in the reanalysis shown in Figure 3.7 (top) CHFP2 is reproducing the seasonal march of storm track activity in the North Pacific reasonably well. However, the degree of midwinter suppression is larger in the reanalysis than in CHFP2. I also note that the interannual variability indicated by the bootstrapped 95% confidence interval is underestimated in CHFP2 compared to ERA40/ERA interim. This may be due to the ENSO-like variability in the freely running simulations of CanCM3, employed in CHFP2, that is moderately less than observed (W.J. Merryfield [2011], personal communication). The simulated suppression is within the bootstrapped 95% confidence interval and therefore not significant. However, the suppression in the ERA40/ERA interim reanalysis is also within the uncertainty and thus not significant either.

In seasonal forecasts initialized in June in each year, the simulated location of the region of maximal storm track activity in meters of geopotential height (Figure 3.8, right) in the North Pacific in November, January and March is reasonably close to ERA40/ERA interim (Figure 3.8, left). However, there is generally less storm track activity in the North Pacific in November in CHFP2 than the observation-based

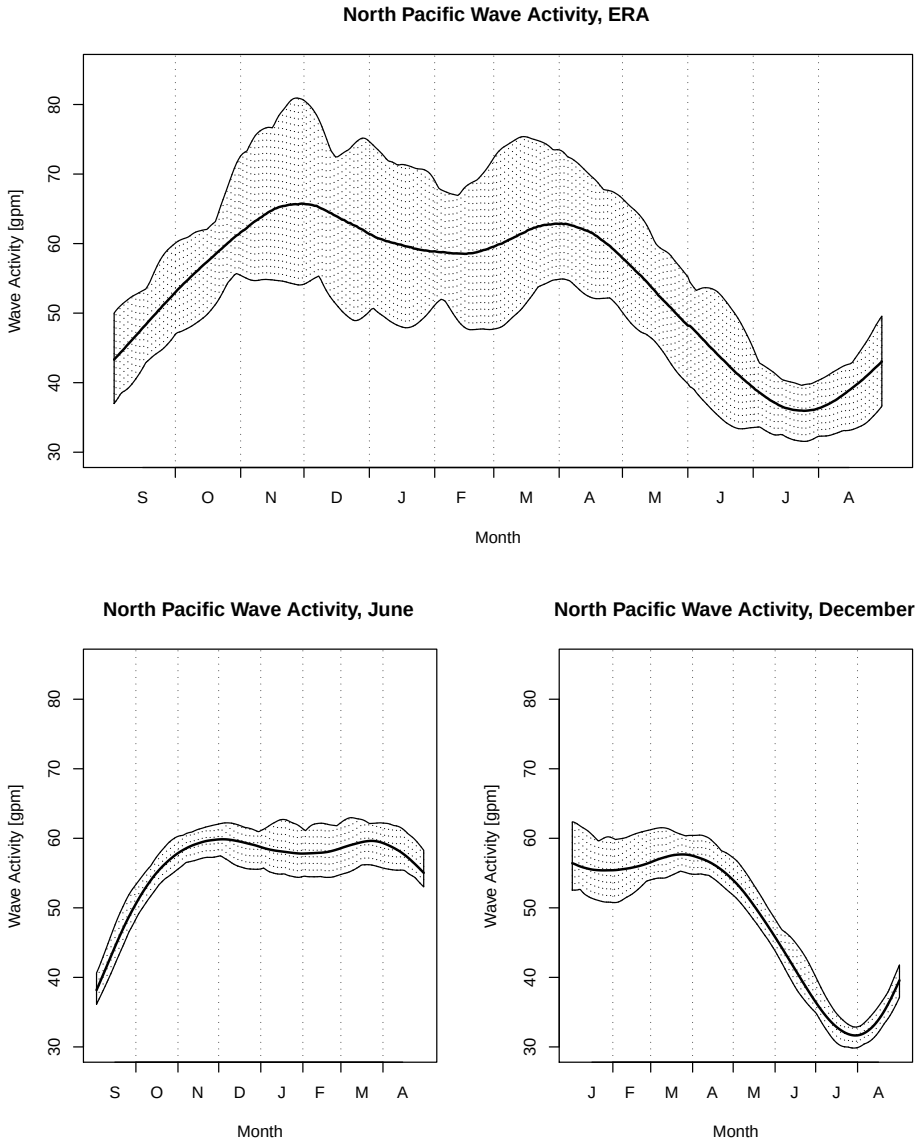

Figure 3.7: ERA40/ERA interim daily storm track activity (top) in meters of geopotential height and bootstrapped 95% confidence interval from September through August (1979–2008) over the North Pacific (150°E–120°W; 40°N–70°N). Simulated daily storm track activity from September through April for June (bottom left), and from January through August for December (bottom right) initialized forecasts, respectively.

reanalysis with maximal values in the North Pacific of roughly 75 gpm in November compared to the observed peak of roughly 80 gpm. In January, the center of action in CHFP2 with a peak value of roughly 75 gpm moves equatorward, so does the observed center of action that looses more strength than in CHFP2 with a maximum of about 75 gpm. In March, the center of action in CHFP2 extends slightly poleward peaking at roughly 75 gpm, so does the center of action in ERA40/ERA interim.

Figure 3.9 (top right), shows the difference in simulated storm track activity between November and January. It is evident that storm track activity in the North Pacific is up to 12 gpm stronger in November than in January, and roughly 6 gpm larger over midlatitude Asia. Figure 3.9 (bottom right), shows the difference in simulated storm track activity between January and March. I note that storm track activity is lower by up to roughly 8 gpm in the North Pacific, and about 4 gpm lower over midlatitude Asia. In CHFP2, both the North Pacific suppressed storm track activity in January and the recovery thereafter go along with similar changes in eddy activity over Asia.

For the observation-based reanalysis, Figure 3.9 (top left) shows the difference in storm track activity between November and January, while Figure 3.9 (bottom left), shows the difference in storm track activity between January and March. Compared against the reanalysis the spatial pattern of the North Pacific suppression in storminess in boreal midwinter is reasonably well represented in CHFP2, besides the discussed larger drop in storm track activity between November and January in the reanalysis (left). The connection between the January suppression in storminess over Asia that goes along with a suppression in North Pacific storminess downstream simulated by CHFP2 is also evident in ERA40/ERA interim. In both the model and the reanalysis, the recovery of North Pacific storm track activity in March relative to January coincides with a recovery of storm track activity over Asia (Figure 3.9, bottom). CHFP2 apparently reproduces the reported suppression of disturbances over Asia in January leading to decreased storm track activity over the North Pacific (Penny et al. [2010]).

In conclusion, seasonal variations in North Pacific storminess may impact PDO skill in CHFP2 by means of a lagged response of the ocean mixed layer to weather "noise" unpredictable at the seasonal time scale. In this framework, the increasing storm track activity in October and November leads to a decrease in PDO skill in November and December. The decreasing storminess starting in December and ending in early February coincides with PDO skill recovery in January and February. The

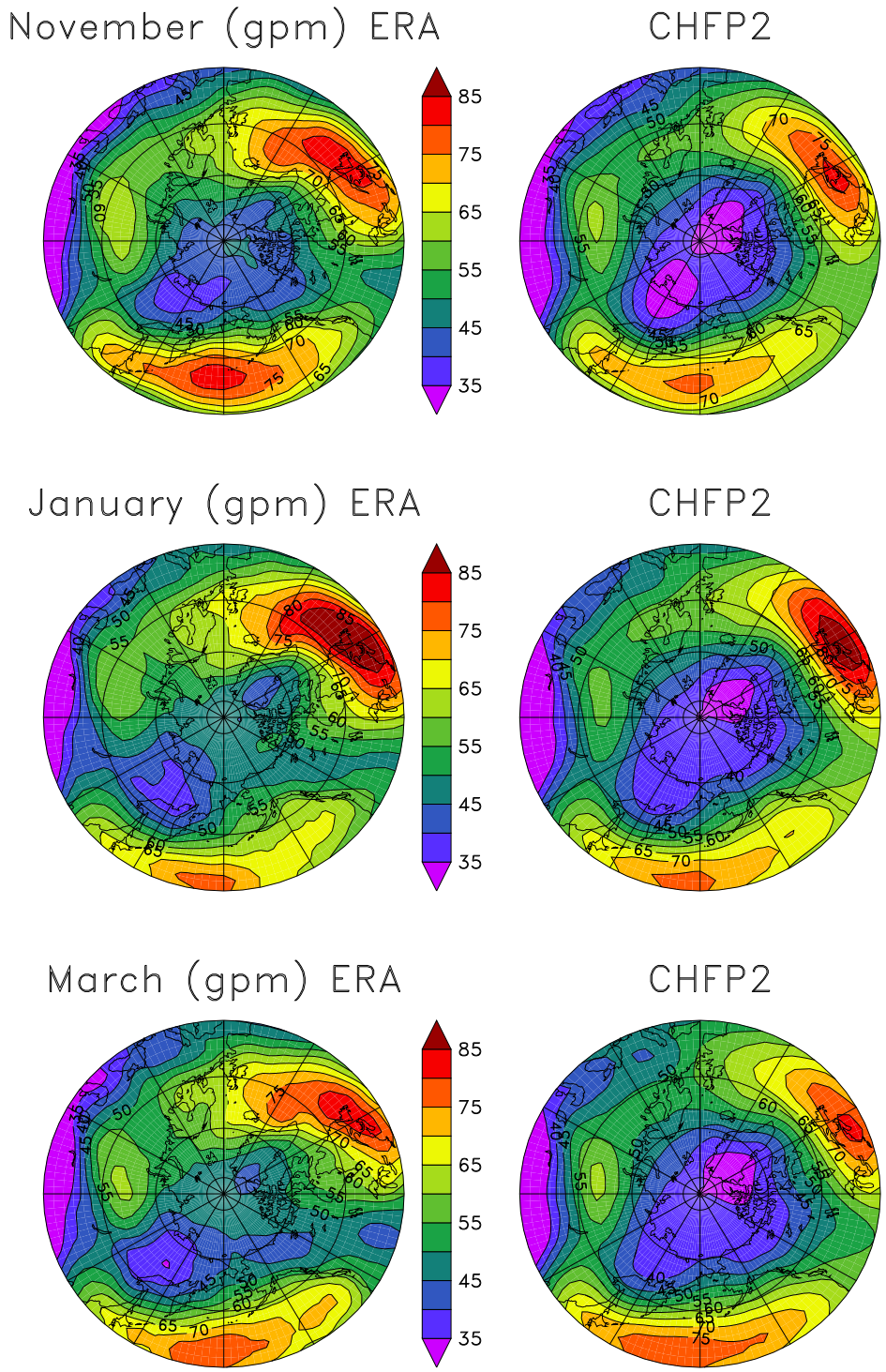

Figure 3.8: ERA40/ERA interim storm track activity (1979–2008) in meters of geopotential height poleward of 40°N (left) in November (top), January (middle) and March (bottom), respectively. Simulated storm track activity (right) in November (top), January (middle) and March (bottom), respectively.

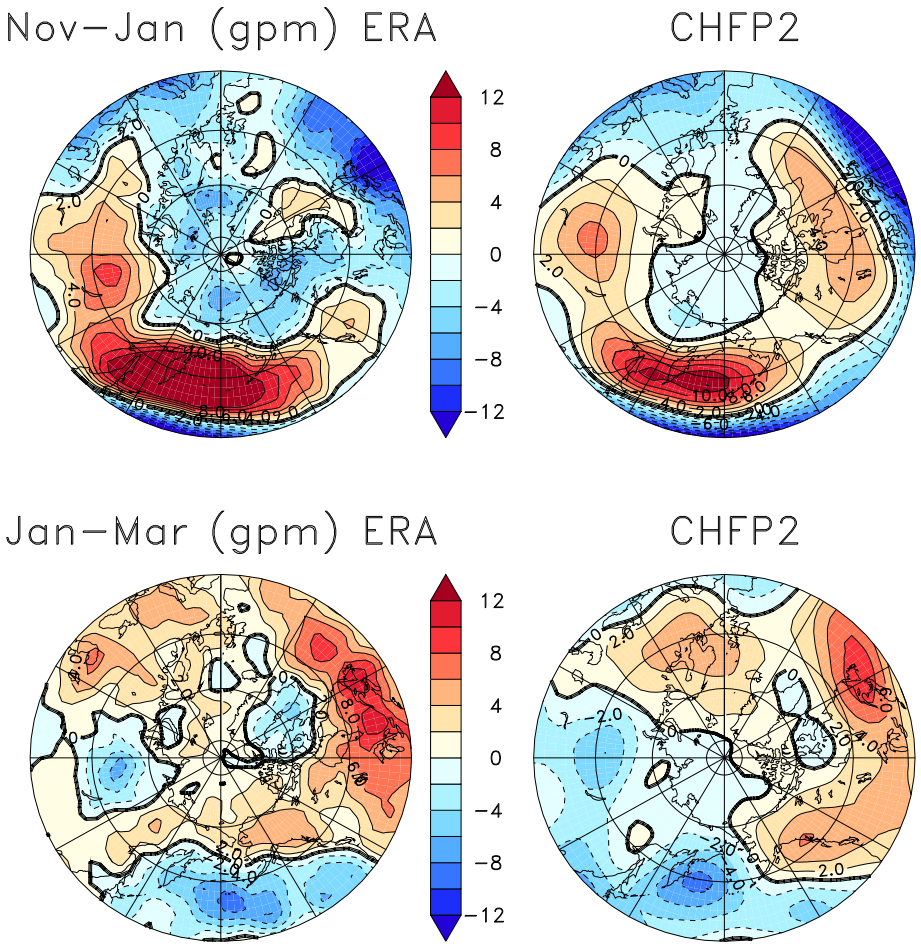

Figure 3.9: Difference between the ERA40/ERA interim (left) storm track activity (1979–2008) in November and January (top), and between January and March (bottom) in meters of geopotential height poleward of 40°N. Difference between the simulated storm track activity (right) in November and January (top), and between January and March (bottom) in meters of geopotential height poleward of 40°N.

subsequent period of increasing storm track activity from mid February through late March coincides with a decrease in PDO skill in March and April.

Storminess Prediction

The strength of North Pacific storminess in the observation-based ERA40/ERA interim reanalysis varies interannually, along with the Pacific/North American pattern (PNA). The PNA measures the state of the atmospheric circulation regime over the Pacific and North America (Wallace and Gutzler [1981]). For example, JFM-mean North Pacific storm track activity tends to be enhanced when the PNA is in its negative state and vice versa. North Pacific storminess and the PNA are therefore

anticorrelated when their JFM average state is concerned indicated by the correlation coefficient of roughly -0.71 (Table 3.4). In addition, North Pacific storm track activity is anticorrelated with ENSO and the PDO (Table 3.4). Here, the relationship is weaker with correlation coefficients between -0.37 (ENSO) and -0.23 (PDO).

Table 3.4: Correlation coefficients ρ between JFM-mean North Pacific storm track activity and the PNA, ENSO, PDO.

ρ STA,PNA	ρ STA,ENSO	ρ STA,PDO
-0.71	-0.37	-0.23

Assuming that North Pacific storminess impacts CHFP2 skill to predict the future evolution of the PDO at the seasonal time scale, the prediction of the magnitude of North Pacific storminess could indicate the skillfulness of a PDO forecast and is of interest itself. In this framework, a seasonal PDO forecast is expected to be more skillful when initialized in years when North Pacific storminess is below the climatological mean state. In order to investigate whether the activity of North Pacific storm tracks is predictable, Figure 3.10 shows the annual mean winter (January, February and March) departures in storm track activity from the 1979–2008 mean activity in the North Pacific in the reanalysis (blue) and predicted by CHFP2 forecasts (red) started in June (top) and December (bottom). The ability of the June initialized forecasts to predict North Pacific storminess six to nine months ahead is limited. In this case, the correlation between CHFP2 and ERA40/ERA interim is 0.17 which is not significantly above zero on a 95% confidence level. Shorter range forecasts of JFM-mean storminess in the North Pacific are not more skillful. Here, the correlation between CHFP2 and the reanalysis is 0.11 and not significantly positive (95% confidence level) either.

For reference, CHFP2 forecasts of JFM-mean storminess in the North Atlantic can be found in Figure A.7 in the Appendix. In this case, the correlation between CHFP2 and the reanalysis is 0.30 for June initialized forecasts, which is not significantly above zero on a 95% confidence level. For December initialized forecasts of North Atlantic storm track activity the correlation is close to zero. This is consistent with a previous study (Pavan and Doblas-Reyes [2000]) that found low correlation skill in seasonal forecasts of North Atlantic storminess.

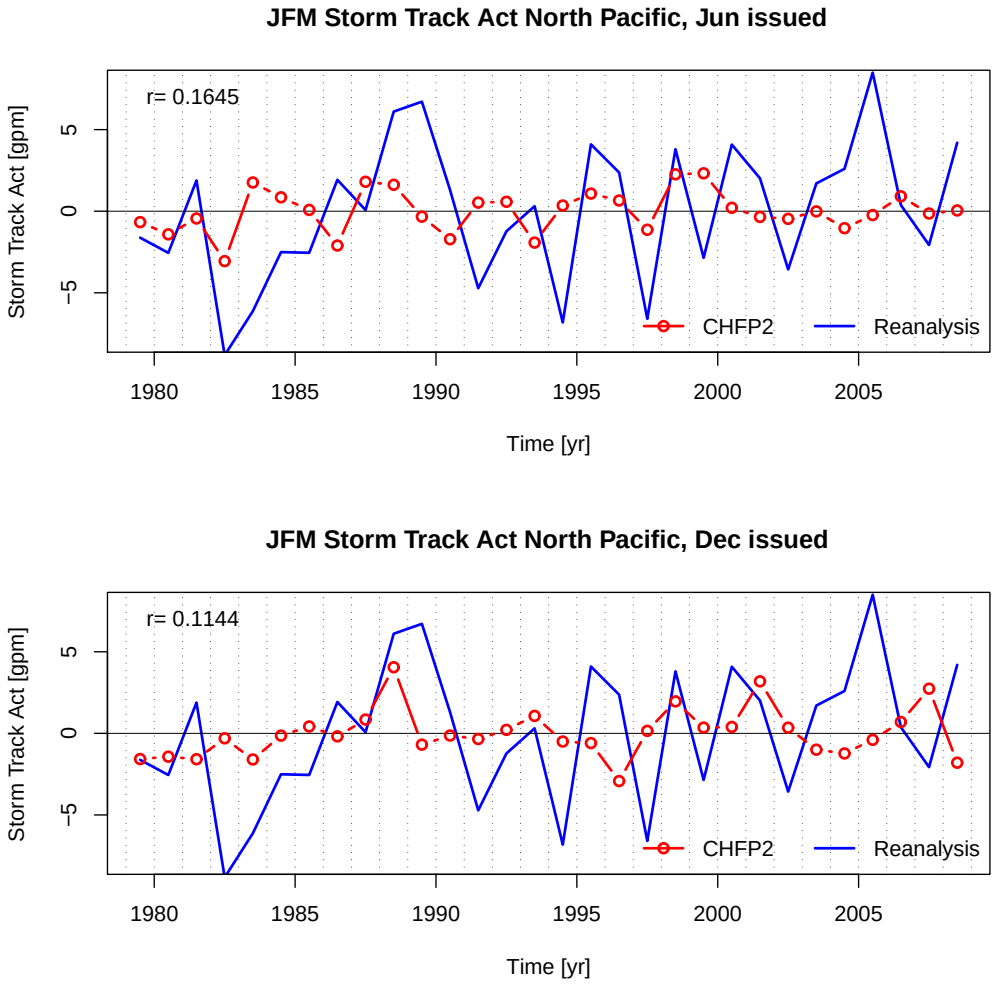

Figure 3.10: North Pacific annual storm track activity (mean of January, February, March) in ERA40/ERA interim (blue) and predicted by CHFP2 forecasts (red) initialized in June (top), and December (bottom), respectively.

North Pacific SST Prediction Compared to PDO Prediction

In order to assess how the discussed PDO skill compares to the skill in predicting pointwise North Pacific SST anomalies, Figures 3.11, 3.12 and 3.13 show the corresponding SDE, MSSS and AC of CHFP2 predicted anomalous North Pacific SSTs, at every grid point averaged over the North Pacific. Verified against the observational SST dataset, the growth in standard error of CHFP2 predicted North Pacific SSTs averaged over the course of a seasonal forecast is roughly 0.64 K, independently of

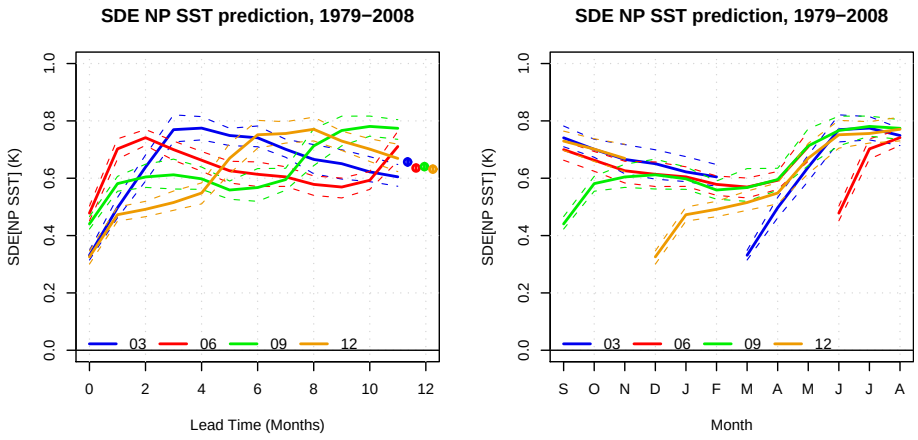

Figure 3.11: SDE (solid lines) and bootstrapped 95% confidence interval (dashed lines) between the predicted and the observed North Pacific SSTs as a function of lead time where the dots, lines on the right show the mean, 95% confidence interval over the forecast range (left panel) and target month (right panel) for four different start months of the forecast (03: March; 06: June; 09: September; 12: December).

the start month (Table 3.1). The standard error (Figure 3.11, right) is generally less in winter (DJF) and larger in summer (JJA).

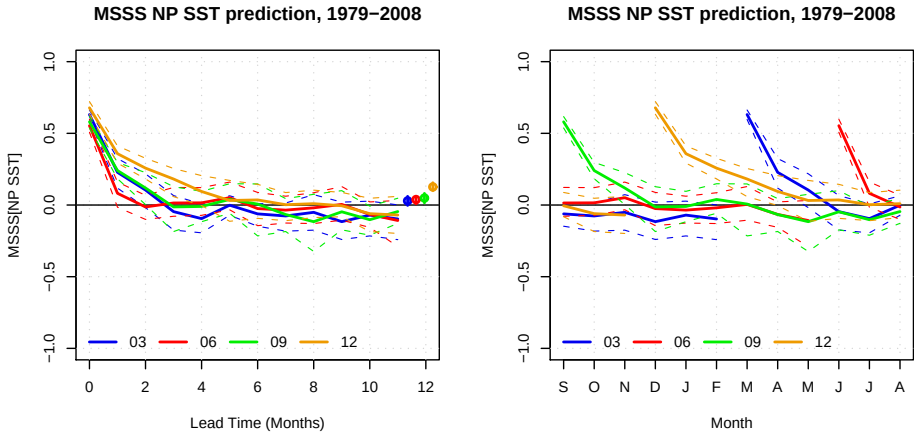

Figure 3.12: MSSS (solid lines) and bootstrapped 95% confidence interval (dashed lines) between the predicted and the observed North Pacific SSTs as a function of lead time where the dots, lines on the right show the mean, 95% confidence interval over the forecast range (left panel) and target month (right panel) for four different start months of the forecast (03: March; 06: June; 09: September; 12: December).

The seasonality seen in the SDE of predicted North Pacific SSTs is reflected in the

MSSS as well. Over the course of a forecast, the MSSS of CHFP2 forecasts started in December stays significantly positive during four months, whereas the MSSS of forecasts started in June is positive for only the first month (Figure 3.12). In this case, CHFP2 predictive skill of North Pacific SSTs averaged over the seasonal forecast range is 0.13 for December initialized forecasts and close to zero for all other start months (Table 3.2).

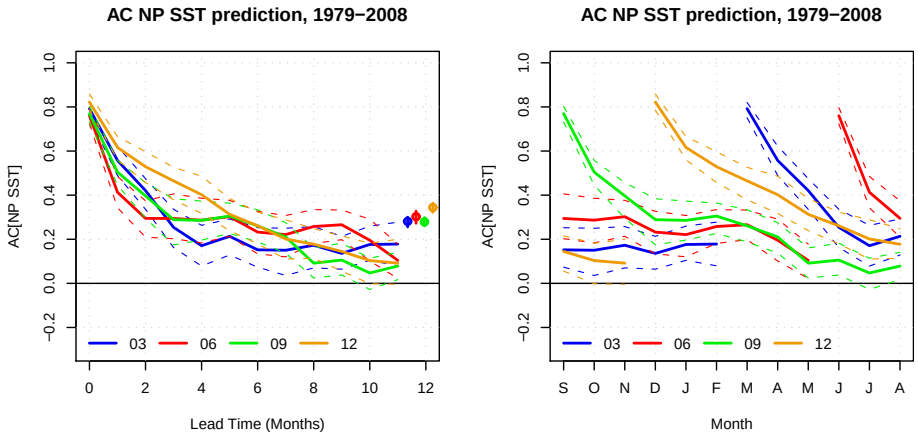

Figure 3.13: AC (solid lines) and bootstrapped 95% confidence interval (dashed lines) between the predicted and the observed North Pacific SSTs as a function of lead time where the dots, lines on the right show the mean, 95% confidence interval over the forecast range (left panel) and target month (right panel) for four different start months of the forecast (03: March; 06: June; 09: September; 12: December).

North Pacific SST correlation skill of CHFP2 forecasts is overall higher than the MSSS (Figure 3.13). However, AC skill drops off rapidly in a similar manner as the MSSS. Averaged over the seasonal forecast range, North Pacific SST AC skill estimates are significantly positive and range between 0.28 (September initialized forecasts) 0.34 (December initialized forecasts) (Table 3.3)

The correlation skills of the PDO and North Pacific SSTs of Figures 3.4 and 3.13 are compared in Figure 3.14 for March (top left), June (top right), September (bottom left) and December (bottom right) initialized forecasts. For all these start months, the mean AC over the 12-month forecast range (as indicated by the dot and error bar on the right in each plot) of the predicted PDO is significantly higher than for the predicted North Pacific SSTs. The most substantial difference in the correlation skill from predicting the PDO compared to SSTs is expected for forecasts started in June.

The skill of CHFP2 to forecast North Pacific SST departures is obviously lower

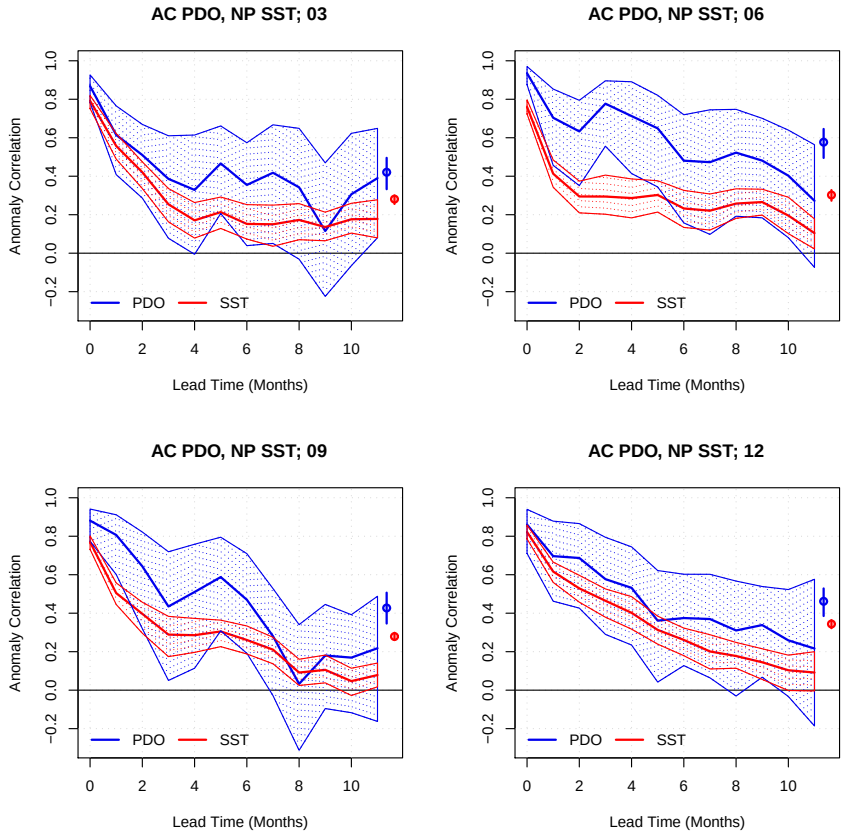

Figure 3.14: AC and bootstrapped 95% confidence interval of the predicted PDO versus the AC of the predicted North Pacific SSTs as a function of lead time where the dots, lines on the right show the mean, 95% confidence interval over the forecast range for four different start months of the forecast (03: March; 06: June; 09: September; 12: December).

than the skill to forecast the leading mode of North Pacific SST departures (PDO). One reason for this difference is the fact that by projecting the SST anomalies onto the observed PDO pattern much of the smaller scale weather "noise" is filtered. To highlight this, CHFP2 predicted North Pacific SST anomalies have been projected onto the pattern of each EOF mode of observed North Pacific SST anomalies. The predicted PC time series have then been verified against the observed PC time series. Figure 3.15 shows the AC skill estimate (with the bootstrapped 95% confidence interval) averaged over the seasonal forecast range for the first 100 EOF modes, that together explain roughly 98% of the total observed SST variance in the North Pacific

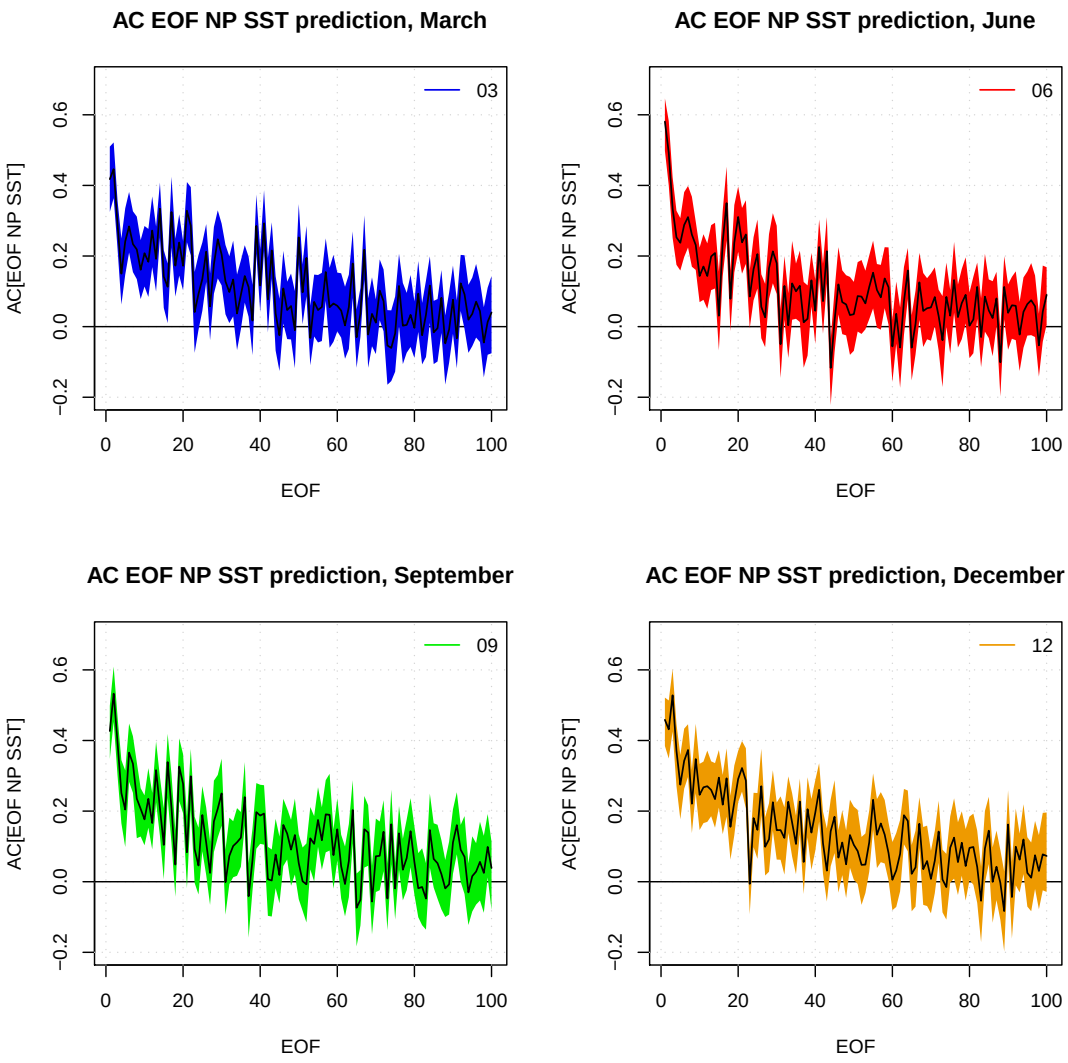

Figure 3.15: AC (solid lines) and bootstrapped 95% confidence interval (dashed lines) between the predicted and observed EOF modes of North Pacific SST, averaged over the 12-month forecast range for four different start months of the forecast (03: March; 06: June; 09: September; 12: December).

for forecasts started in March (top left), June (top right), September (bottom left), December (bottom right). With some exceptions, the lower EOF modes of North Pacific SST are generally more skillfully predicted by CHFP2 than the higher modes. The prediction of North Pacific SSTs, the sum of all the EOF modes, is thus less skillful than, e.g., the leading EOF mode (PDO).

Table 3.5: Mean AC over 12-month forecast range for the leading 5 EOF modes of North Pacific SST.

Month	$\overline{\rho}$ EOF1	$\overline{\rho}$ EOF2	$\overline{\rho}$ EOF3	$\overline{\rho}$ EOF4	$\overline{\rho}$ EOF5
03	0.42	0.45	0.29	0.15	0.24
06	0.58	0.49	0.34	0.25	0.24
09	0.43	0.53	0.40	0.25	0.20
12	0.46	0.43	0.53	0.37	0.28

For the first 14 CHFP2 predicted EOF modes of North Pacific SST the 12-month averaged correlation skill is significantly positive for all the start months of the forecast. The first 14 modes combined explain roughly 74% of the total SST variance. The 12-month mean AC skill estimates of the first five EOF modes (Table 3.5) explaining roughly 20%, 13%, 8%, 7%, 5% of the total variance indicate that besides December initialized forecasts, the leading two modes are the most skillfully predicted. The second mode of North Pacific SST often referred to as the Victoria mode, has the following physical characteristics: a dipole with warm anomalies in the subtropical part and cold anomalies towards the north (Bond et al. [2003]). The Victoria mode coincides with dramatic ecological shifts (Di Lorenzo et al. [2008]) in the northeast Pacific ocean that can not be explained by variations in the PDO index.

3.2.2 ENSO

In seasonal climate prediction employing coupled dynamical models initialized with observations, predictive skill is commonly assessed for ENSO associated SST anomalies in the tropical Pacific (e.g., Palmer et al. [2004], Saha et al. [2006], Weisheimer et al. [2009]). In this case, the NINO3.4 index, the predicted SST anomalies averaged over the region 5°S–5°N, 170°W–120°W, is often taken to represent ENSO skill. In order to put the discussed PDO skill in context with ENSO skill, I am evaluating ENSO predicted by CHFP2 in two manners: first, the ENSO index (hereafter ENSO) is derived similarly as for the PDO, namely by projecting the predicted SST anomalies onto the leading EOF pattern of observed detrended SST anomalies in the tropical Pacific (120°E–90°W, 10°S–10°N), second, the NINO3.4 index (hereafter NINO3.4). Although ENSO is a complex atmosphere-ocean coupled phenomenon that needs to be described by more than one mode (e.g., Meinen and McPhaden [2000]), the first

mode of anomalous SSTs can be used to approximate the ENSO state in models and observational datasets (Merryfield [2006]).

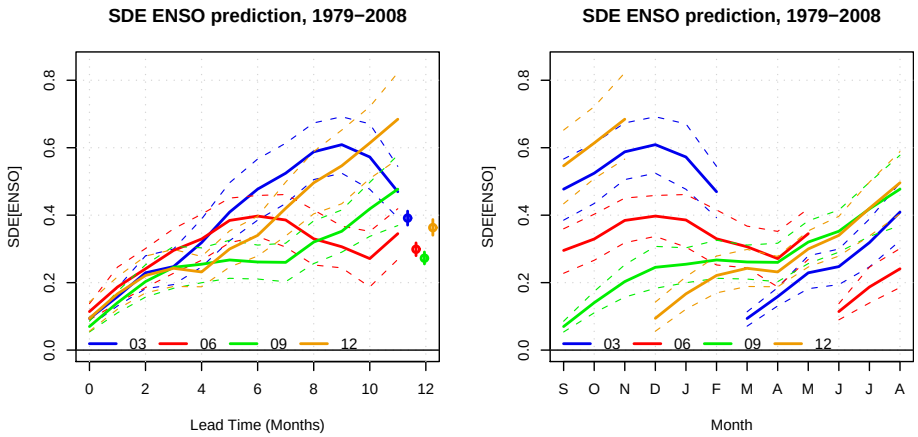

Figure 3.16: SDE (solid lines) and 95% confidence interval (dashed lines) between the predicted and the observed ENSO index as a function of lead time where the dots, lines on the right show the mean, 95% confidence interval over the forecast range (left panel) and target month (right panel) for four different start months of the forecast (03: March; 06: June; 09: September; 12: December).

In CHFP2, the standard error growth of forecasting ENSO as shown in Figure 3.16 during the first five months is smaller and more uniform and thus less dependent on the season of the start of the forecast than for the PDO. However, the standard errors grow more rapidly in April and thereafter known as the "spring" (during spring in the Northern Hemisphere) prediction barrier (Saha et al. [2006]), when the mixed layer in the eastern tropical Pacific is shallow. A shallow ocean mixed layer means that a smaller amount of water is well mixed and in contact with the atmosphere reducing the memory of the atmosphere-ocean coupled system and therefore the signal to noise (i.e., weather "noise") ratio of the predictable component.

The rapid error growth in ENSO prediction in boreal spring is reflected in the variance measure MSSS (Figure 3.17). In this case, CHFP2 ENSO forecasts initialized in June are significantly more skillful in terms of MSSS than those initialized in March. The MSSS estimate averaged over the 12-month forecast range for a June started forecast reaches roughly 0.66 whereas for March started forecast this measure reaches roughly 0.44 (Table 3.2).

CHFP2 correlation skill in forecasting the ENSO index are shown in Figure 3.18. As for the MSSS, the AC skill of ENSO forecasts initialized in June are significantly

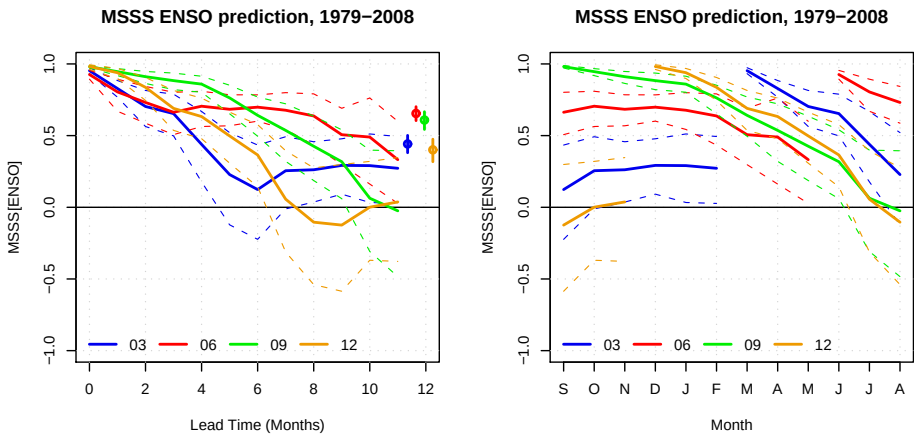

Figure 3.17: MSSS (solid lines) and 95% confidence interval (dashed lines) between the predicted and the observed ENSO index as a function of lead time where the dots, lines on the right show the mean, 95% confidence interval over the forecast range (left panel) and target month (right panel) for four different start months of the forecast (03: March; 06: June; 09: September; 12: December).

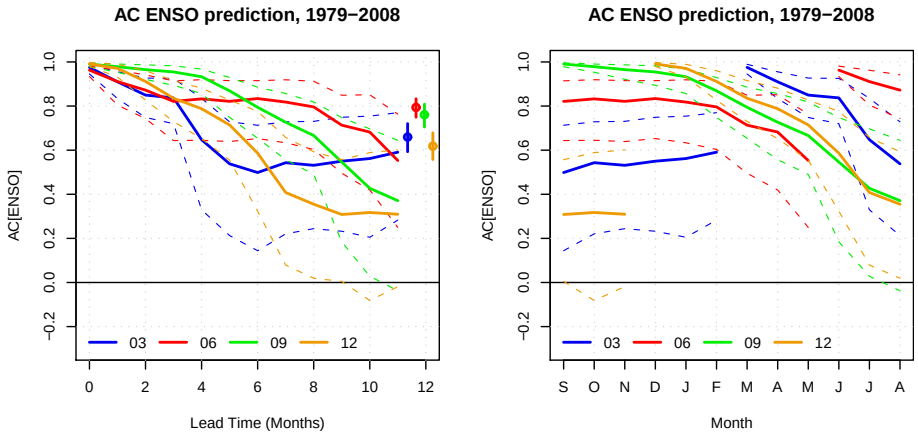

Figure 3.18: AC (solid lines) and 95% confidence interval (dashed lines) between the predicted and the observed ENSO index as a function of lead time where the dots, lines on the right show the mean, 95% confidence interval over the forecast range (left panel) and target month (right panel) for four different start months of the forecast (03: March; 06: June; 09: September; 12: December).

more skillful than March initialized forecasts. Here, the 12-month mean correlation skill estimates are roughly 0.79 (June), and 0.66 (March), respectively (Table 3.3). Over the course of a forecast, the AC stays significantly positive up to lead month eight independently of the month the forecast is started.

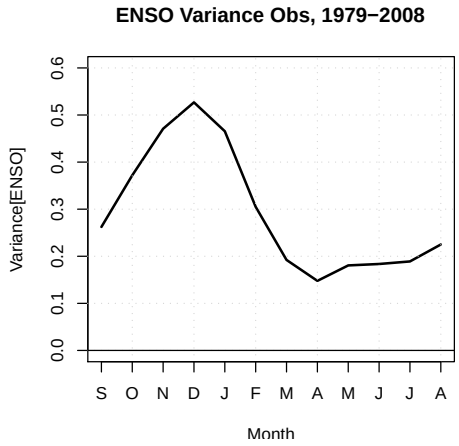

Figure 3.19: Observed variance of the ENSO index.

For reference, the corresponding SDE, MSSS and AC for the CHPF2 predicted NINO3.4 index are found in Figures A.8, A.9, A.10 in the Appendix. The NINO3.4 performance measured by the MSSS and AC are similar to the discussed ENSO index performance. In terms of their mean skill measures over the 12-month forecast range, NINO3.4 MSSS and AC are lower for June and September initialized forecasts (Tables 3.2, 3.3). ENSO index forecasts started in December are more skillful than NINO3.4 in terms of MSSS, but virtually identical in terms of AC.

In CHFP2, seasonal prediction of the PDO is significantly less skillful in terms of AC than seasonal ENSO prediction for forecasts initialized in all seasons (March, June, September, December). The most skillful June started PDO forecasts, however, compete in terms of forecast fidelity with the least skillful ENSO forecasts started in December. Their correlation skills are statistically indistinguishable.

3.2.3 PDO without ENSO influence

An attempt to identify extratropical correlation skill with the tropical Pacific-related part removed is presented in Figure 3.20. Here, the AC between the predicted PDO and ENSO indices is removed from the AC between the predicted and the observed PDO indices based on partial correlations. On the seasonal time scale in CHFP2, the PDO correlation skill over the 12-month forecast range decreases by roughly 10% when the ENSO contribution is removed in this way (Table 3.3). The annual cycle

of the variance of the observed ENSO signal (Figure 3.19) indicates that the ENSO signal is strong in November through January when the mixed layer in the central and eastern tropical Pacific is anomalously deep (Figure 7 in Wang et al. [2000]). Therefore, the ENSO influence in the North Pacific is likely enhanced during the first few months of September initialized forecasts and explain a larger fraction of the PDO signal. For forecasts started in December, the part of the PDO correlation skill that is due to skill in the tropical Pacific drops to roughly 8%. In this case, only two months of anomalously deep mixed layer remain until the forecasts encounter relatively shallow climatological mixed layer depths in February and March (Figure 7 in Wang et al. [2000]). For all start months of the forecasts, the PDO correlation skill with the ENSO skill removed is lower than the PDO correlation skill (Figures 3.4, 3.20). However, the drop in PDO correlation skill without ENSO is still within the confidence interval and therefore the uncertainty of the PDO skill.

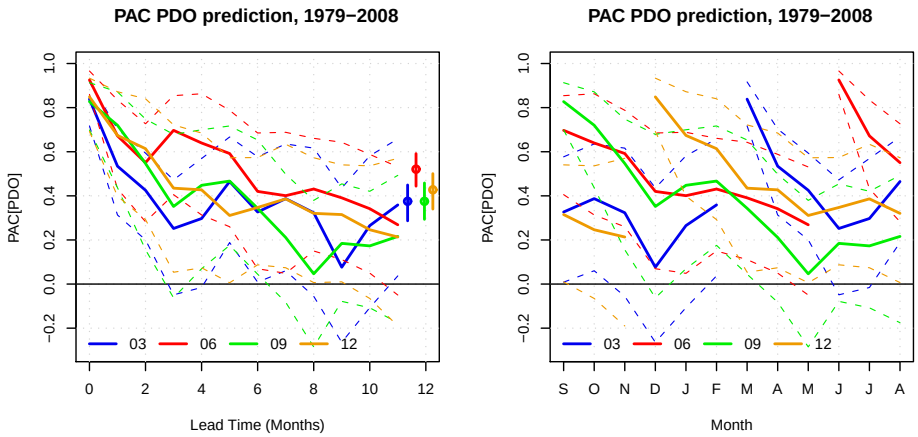

Figure 3.20: Partial AC (solid lines) and bootstrapped 95% confidence interval (dashed lines) between the predicted and the observed PDO index with the predicted ENSO correlated part removed as a function of lead time where the dots, lines on the right show the mean, 95% confidence interval over the forecast range (left panel) and target month (right panel) for four different start months of the forecast (03: March; 06: June; 09: September; 12: December).

3.2.4 PNA and NPI

The link between the PDO and synoptic atmospheric circulation can be highlighted by regressing the 500 hPa geopotential height field from November through March onto the PDO index (Mantua et al. [1997]). The loading pattern of this linear regression is similar to the prominent Pacific/North American pattern (PNA), an index measuring

changes in the prevalent atmospheric circulation regime over the Pacific ocean and the North American continent at 500 hPa geopotential height. The PNA consists of four centers of action, the first is located near Hawaii (20°N, 160°W), the second near the Aleutians in the North Pacific (45°N, 165°W), the third over western Canada (55°N, 115°W), and the fourth over the south-eastern US (30°N, 85°W) (Wallace and Gutzler [1981]). Another well known atmospheric index that is linked to the PDO is the North Pacific index (NPI) (Trenberth and Hurrell [1994]). It measures the strength (atmospheric pressure) of the climatological Aleutian low at sea level. At

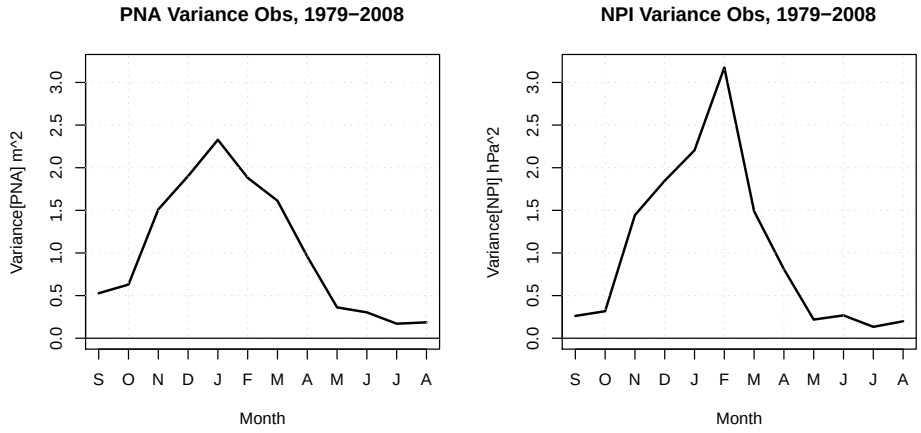

Figure 3.21: Observed variance of the PNA (left) and NPI (right).

times when the PNA is positive and the NPI negative, more low pressure systems tend to occur near the Aleutian islands. These cyclones advect relatively warm and moist air from lower latitudes poleward along the west-coast of North America. In this case, the atmospheric forcing is such that a positive PDO phase with warm SST anomalies in the north-eastern Pacific is likely to follow. I am therefore investigating how skillful the PNA and NPI is predicted by CHFP2 at the seasonal time scale.

PNA

The seasonal cycle of observed PNA variance shown in Figure 3.21 (left) peaks in January with an appreciable magnitude from November through March. On the other hand, the seasonal cycle of observed NPI variance (Figure 3.21, right) peaks in February, also with an appreciable magnitude from November through March.

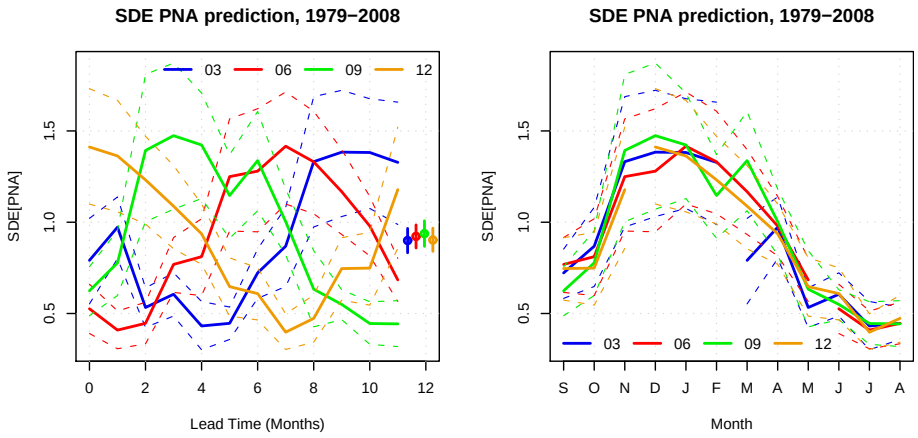

Figure 3.22: SDE (solid lines) and bootstrapped 95% confidence interval (dashed lines) between the predicted and the observed PNA-index as a function of lead time where the dots, lines on the right show the mean, 95% confidence interval over the forecast range (left panel) and target month (right panel) for four different start months of the forecast (03: March; 06: June; 09: September; 12: December).

Here, the PNA index is determined using the pointwise method following Wallace and Gutzler [1981], whereas the NPI is inferred from North Pacific sea level pressure averaged over 30°N–65°N, 160°E–140 °W, the area of the climatological Aleutian low. Both PNA and NPI are then normalized by their 30-year standard deviation covering the CHFP2 period for the observations and by the ensemble mean standard deviation for the predicted indices.

The 12-month averaged magnitudes of standard error in predicting the PNA over the course of a forecast in the order of 0.9 standard deviations (Table 3.6) are statistically indistinguishable and thus independent from the month the forecast is initialized (Figure 3.22, left). Rapid error growth in predicting the PNA is evident in October/November in all forecasts for all start months (Figure 3.22, right). Between November and March, forecast errors remain roughly the same and are reduced thereafter. The rise and drop off in standard error in predicting the PNA occurs at times when the seasonal cycle of observed PNA variance reaches appreciable values.

The performance of CHFP2 to predict the PNA index measured by the MSSS (Figure 3.23) is only significantly positive at lead zero of March initialized forecasts.

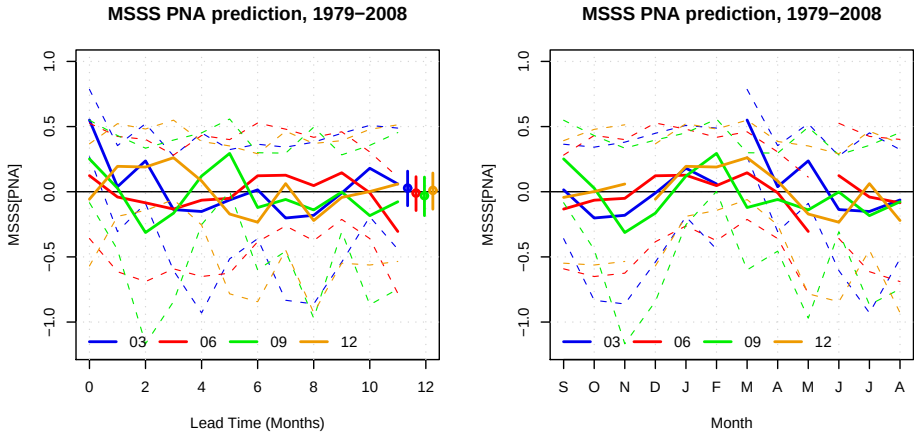

Figure 3.23: MSSS (solid lines) and bootstrapped 95% confidence interval (dashed lines) between the predicted and the observed PNA-index as a function of lead time where the dots, lines on the right show the mean, 95% confidence interval over the forecast range (left panel) and target month (right panel) for four different start months of the forecast (03: March; 06: June; 09: September; 12: December).

Table 3.6: Mean SDE over 12-month forecast range for the PNA (m), NPI (hPa) prediction.

Month	$\overline{SDE}$ PNA	$\overline{SDE}$ NPI
03	0.90	0.87
06	0.93	0.88
09	0.94	0.90
12	0.90	0.87

The MSSS ranges roughly between zero and 0.5 indicating that the variance of the predicted PNA is underestimated relative to the variance of the observed PNA. For all the forecast start months, the MSSS of the PNA averaged over the seasonal forecast range (Table 3.7) is statistically not distinguishable from zero, which means that the predicted PNA is no more skillful than a prediction inferred from the climatology.

CHFP2 PNA forecasts fare better when their correlation skill is considered (Figure 3.24). Because AC is less affected by the underestimated PNA variance than the MSSS. For all the forecast start months excluding September, correlation skill of the

Table 3.7: Mean MSSS over 12-month forecast range for the PNA, NPI prediction.

Month	$\overline{MSSS}$ PNA	$\overline{MSSS}$ NPI
03	0.03	0.02
06	-0.01	-0.01
09	-0.03	-0.05
12	0.01	-0.01

PNA averaged over the 12-month forecast range (Table 3.8) is significantly positive. PNA correlation skill stays significantly positive for December initialized forecasts (Figure 3.24) until March. This is comparable to the results of dynamical PNA predictions employing coupled climate models from different European centers (Palmer et al. [2004]). CHFP2 correlation skill averaged over the course of a seasonal forecast is significant when started in March, June or December. In some cases, CHFP2

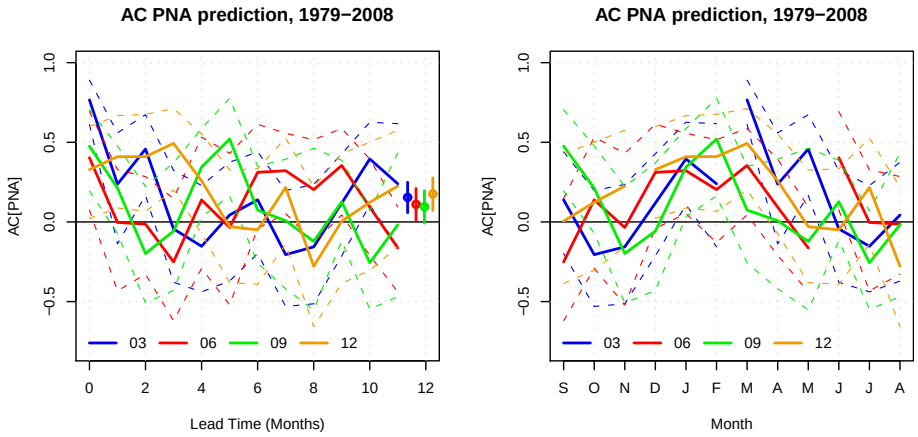

Figure 3.24: AC (solid lines) and bootstrapped 95% confidence interval (dashed lines) between the predicted and the observed PNA-index as a function of lead time where the dots, lines on the right show the mean, 95% confidence interval over the forecast range (left panel) and target month (right panel) for four different start months of the forecast (03: March; 06: June; 09: September; 12: December).

PNA predictions exhibit significantly positive correlation skill even at longer leads. September initialized forecasts, e.g., reach significantly positive AC values in January

and February. June initialized forecasts, e.g., reach significantly positive AC values in December, January and again later on in March. Finally, even March initialized forecasts reach significantly positive AC values ten months later in January.

Table 3.8: Mean AC over 12-month forecast range for the PNA, NPI prediction.

Month	$\overline{AC}$ PNA	$\overline{AC}$ NPI
03	0.16	0.19
06	0.11	0.18
09	0.10	0.11
12	0.18	0.18

NPI

As for the PNA, the 12-month averaged standard error magnitudes in predicting the NPI over the course of a forecast (Table 3.6) are statistically indistinguishable and therefore not dependent on the month the forecast is initialized (Figure 3.25). The onset of rapid error growth in predicting the NPI in October/November and the drop off leading up to May is similar to the PNA. However, the standard error of the CHFP2 predicted NPI peaks in February, along with the seasonal cycle of the variance of the observed NPI. The standard error of the predicted NPI as a function of month reaches very similar values independently of the start month of the forecast.

In terms of the variance measure MSSS, this system is not more successful at forecasting the NPI (Table 3.7) than the PNA, when the MSSS is averaged over the seasonal forecast range. Compared to the observed NPI variance, the predicted NPI variance is underestimated, which is reflected in an often low, but still positive MSSS (Figure 3.26).

CHFP2 is more successful at forecasting the sign of the NPI. This is evident in the 12-month averaged correlation skill (Table 3.8), which is significantly positive for all start months (Figure 3.27). By this measure, CHFP2 NPI forecasts fare better than PNA forecasts when correlation skill is considered. This result is new, since no previous work has yet investigated the prediction of the NPI employing a coupled climate model.

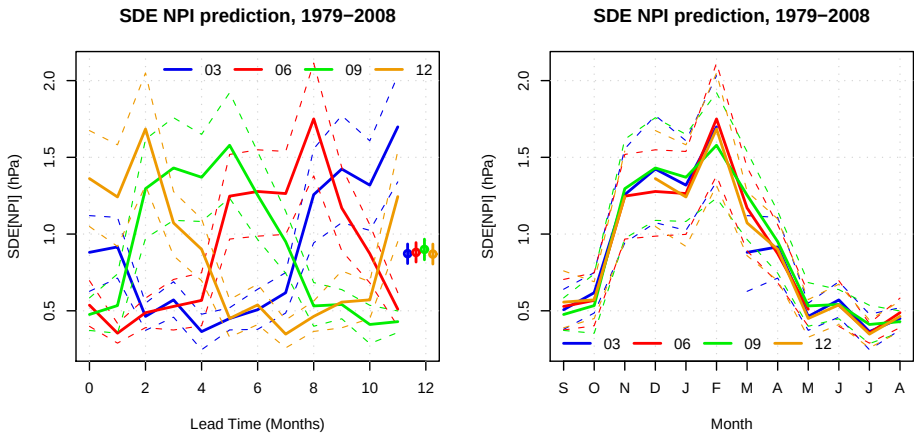

Figure 3.25: SDE (solid lines) and bootstrapped 95% confidence interval (dashed lines) between the predicted and the observed NPI as a function of lead time where the dots, lines on the right show the mean, 95% confidence interval over the forecast range (left panel) and target month (right panel) for four different start months of the forecast (03: March; 06: June; 09: September; 12: December).

3.2.5 Pacific Influences on North American Climate

In this chapter, the skill of CHFP2 to predict SST departures associated with the PDO and ENSO at the seasonal time scale has been discussed. On the other hand, CHFP2 skill of the PNA and the NPI has been established. The atmospheric response to Pacific SST anomalies seen, e.g., in the PNA index can influence North American climate. In this section, I am therefore investigating the ability of CHFP2 to predict Pacific influences on North American temperature and precipitation. First, the focus is on PDO, and then ENSO influences.

PDO Influence on North American Temperature and Precipitation

In order to derive the observed time series of the PDO influence on North American climate departures, the observed departures are projected onto the regression pattern of the observed PDO influence. A linear trend has been removed from the observational dataset so that the anomalies considered are not due to the effects of increasing greenhouse gases. The observation-based ERA40/ERA interim reanalyses (Uppala et al. [2005]) serve as the observational dataset.

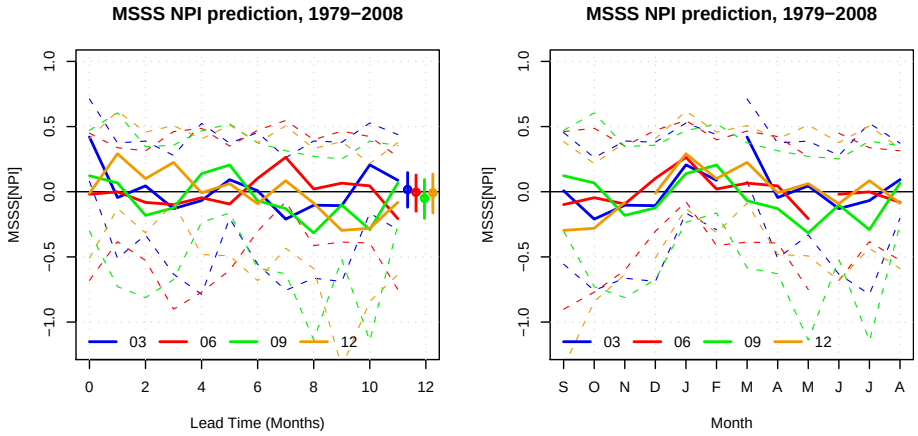

Figure 3.26: MSSS (solid lines) and bootstrapped 95% confidence interval (dashed lines) between the predicted and the observed NPI as a function of lead time where the dots, lines on the right show the mean, 95% confidence interval over the forecast range (left panel) and target month (right panel) for four different start months of the forecast (03: March; 06: June; 09: September; 12: December).

The part of anomalous North American surface temperature $T'(\vec{x},t)$ that is correlated with the PDO can be inferred from the linear regression of $T'(\vec{x},t)$ onto the PDO index $p_1(t)$. The regression coefficient at each grid point $\hat{r}(\vec{x})$ is estimated by the covariance between the temperature field and the PDO index, normalized by the variance of the PDO index

$$\hat{r}(\vec{x}) = \frac{\overline{p_1(t)T'(\vec{x},t)}}{\overline{p_1(t)^2}} \tag{3.1}$$

where the overlines represent the average of all the realizations over time. The observed time series $v(t)$ of the PDO influence on North American temperature is derived from the projection of the observed temperature anomalies $T'(\vec{x},t)$ onto the observed pattern of regression coefficients

$$v(t) = \frac{\langle T'(\vec{x},t)\hat{r}(\vec{x})\rangle}{\langle \hat{r}(\vec{x})^2\rangle} \tag{3.2}$$

where the angled brackets represent the area weighted average over North America. The predicted time series $f(t)$ of the PDO influence on North American temperature is derived similarly from the projection of the predicted North American temperature

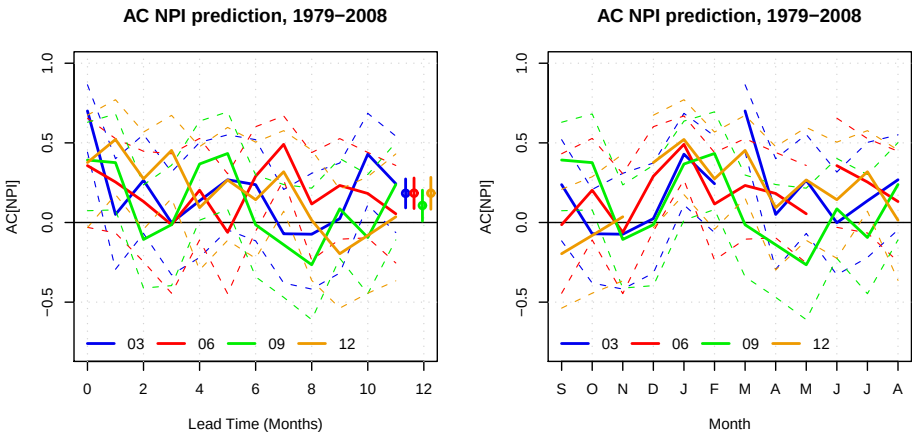

Figure 3.27: AC (solid lines) and bootstrapped 95% confidence interval (dashed lines) between the predicted and the observed NPI as a function of lead time where the dots, lines on the right show the mean, 95% confidence interval over the forecast range (left panel) and target month (right panel) for four different start months of the forecast (03: March; 06: June; 09: September; 12: December).

anomaly field $F'(\vec{x},t)$ onto the observed pattern of regression coefficients

$$f(t) = \frac{\langle F'(\vec{x},t)\hat{r}(\vec{x})\rangle}{\langle \hat{r}(\vec{x})^2\rangle} \tag{3.3}$$

where the angled brackets represent the area weighted average over North America. For the PDO influence on North American precipitation departures, the same mathematical framework is used.

The annual cycle of the observed variance of the index measuring PDO influence on North American temperature ($\hat{r}$ ranges between -1.2 K in the eastern part and 2.6 K in the western part of North America) is shown in Figure 3.28 (left). It reaches the highest values in December and January. For the observed PDO influence on precipitation over North America ($\hat{r}$ ranges between -16 mm/month along the northern west coast and 20 mm/month in the western and south-eastern United States) on the other hand, the variance has a small peak in January and dominant peak in June (Figure 3.28, right).

The CHFP2 predicted indices of PDO associated North American temperature and precipitation is verified against the observed influence inferred from the ERA40/ERA

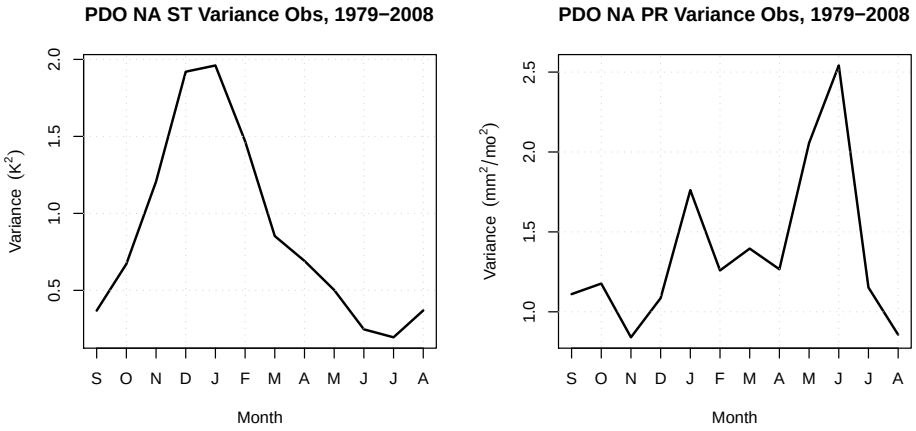

Figure 3.28: Observed variance of the PDO influence $v(t)$ on North American temperature (left) and precipitation (right).

interim dataset.

Temperature

CHFP2 performance to forecast the sign of temperature departures over North America associated with the PDO measured by correlation skill is shown in Figure 3.29. When the skill is averaged over the seasonal forecast range, the correlation skill of the CHFP2 predicted PDO influence on North American temperature departures is positive for all start months (Table 3.9) ranging between roughly 0.06 (June started forecast) and roughly 0.16 (December started forecast). For December initialized forecasts this measure is significantly above zero, while March, June, September initialized forecasts exhibit an AC that is statistically not distinguishable from zero. Correlation skill of forecasts started in December stays significantly positive during the first two months.

For reference, the standard error of the predicted PDO influence on North American temperature in seasonal hindcasts from CHFP2 verified against the observed influence can be consulted in Figure A.11 in the Appendix. The mean standard error over the course of a forecast reaches roughly 0.84–0.93 K (Table A.1). Maximal standard error is reached in winter (DJF), along with the seasonal cycle of the observed variance of this index. The fidelity of CHFP2 to forecast temperature anomalies over North America associated with the PDO measured by the MSSS can be consulted in

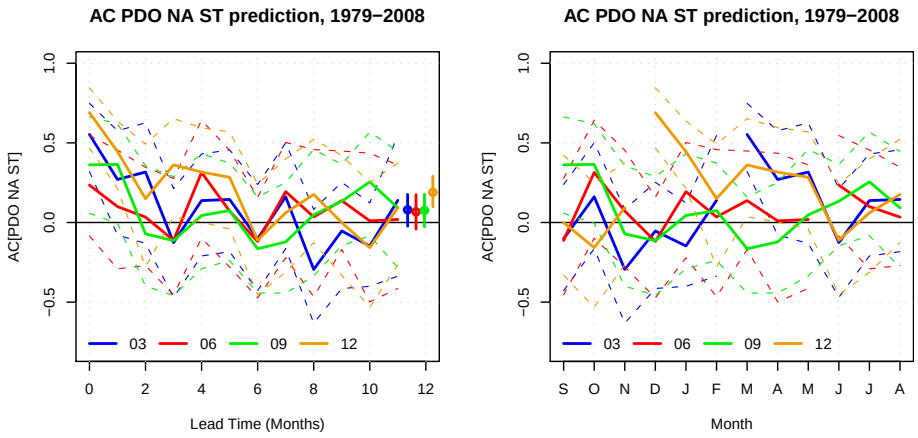

Figure 3.29: AC (solid lines) and bootstrapped 95% confidence interval (dashed lines) between the predicted and the observed PDO influence on North American temperature index as a function of lead time where the dots, lines on the right show the mean, 95% confidence interval over the forecast range (left panel) and target month (right panel) for four different start months of the forecast (03: March; 06: June; 09: September; 12: December).

Table 3.9: Mean AC over 12-month forecast range indicated by the overbar for the prediction of the PDO influence on North American temperature, precipitation, and of the ENSO influence on North American temperature, precipitation.

Month	$\overline{AC}$ PDO T	$\overline{AC}$ PDO PR	$\overline{AC}$ ENSO T	$\overline{AC}$ ENSO PR
03	0.14	0.21	0.22	0.25
06	0.06	0.23	0.20	0.27
09	0.13	0.15	0.29	0.27
12	0.16	0.20	0.20	0.25

the Appendix (Figure A.12). In this case, the MSSS is significantly negative for June initialized forecasts when averaged over the seasonal forecast range (Table A.2), when the observed variance of the considered index is relatively small and the variance of the predicted signal overestimated.

Precipitation

Finally, CHFP2 predicted PDO associated precipitation anomalies over the North American continent measured by correlation skill is shown in Figure 3.30. In this case, CHFP2 is able to skillfully predict the sign of the PDO influence on North American precipitation. For all start months, correlation skill is significantly positive when averaged over the seasonal forecast range. By this measure, CHFP2 reaches correlation skill values ranging between roughly 0.15 for September initialized forecasts, and roughly 0.23 for June initialized forecasts (Table 3.9). The correlation skill of forecasts of the PDO associated North American precipitation departures started in June stays significantly positive until October (lead month four). Forecasts that are started in different months reach significantly positive AC values in September and May at different lead times.

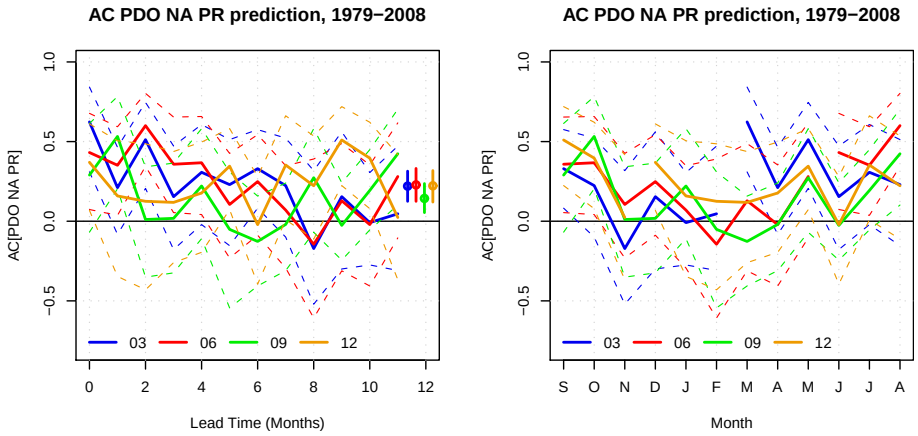

Figure 3.30: AC (solid lines) and bootstrapped 95% confidence interval (dashed lines) between the predicted and the observed PDO influence on North American precipitation index as a function of lead time where the dots, lines on the right show the mean, 95% confidence interval over the forecast range (left panel) and target month (right panel) for four different start months of the forecast (03: March; 06: June; 09: September; 12: December).

For reference, the evolution of the standard error in forecasting North American precipitation departures associated with the PDO is found in Figure A.13 in the Appendix. The standard error averaged over the course of a forecast (Table A.1) is of

a similar magnitude of roughly 1.1 mm/month for all start months. Along with the seasonal cycle of the variance of the observed index, the standard error growth peaks in January and June independently of the month the forecast is initialized. The fidelity of CHFP2 to forecast PDO associated precipitation anomalies over North America measured by the MSSS is found in the Appendix (Figure A.14). The MSSS of March and June initialized forecasts ranges roughly between zero and 0.5 until lead month four. This indicates that the variance of the predicted precipitation anomalies and thus their magnitude is underestimated compared to the observed. The MSSS is therefore close to zero when averaged over the seasonal forecast range (Table A.2).

To sum up the CHFP2 performance to forecast PDO influence over the North American continent, the 12-month averaged AC skill of the PDO associated North American temperature departures is significantly positive for one (December) out of four start months, whereas the 12-month averaged AC skill of PDO associated North American precipitation departures is significantly positive for all four start months (March, June, September, December). In CHFP2 at the seasonal time scale, the PDO is therefore a better predictor for North American precipitation than North American temperature when the correlation skill averaged over the course of a seasonal forecast is considered.

Explained Variance

In order to judge the potential usefulness of the discussed predictive skill of North American temperature and precipitation, it is worth considering the magnitude of the predicted signal relative to the magnitude of the total signal. One way to approach this issue is to infer the PDO-related variance from the temporal evolution of the North American regression pattern (the concerned variable regressed onto the observed PDO index) in the observation-based ERA40/ERA interim dataset. I thus show the seasonal cycle of the fraction of the variance of the PDO associated temperature, precipitation averaged over North America, divided by the total temperature, precipitation variance averaged over North America in Figure 3.31.

In ERA40/ERA interim, the PDO influence explains on average roughly 12% of the North American temperature variance (35% of the standard deviation). Here, the observed annual cycle of explained variance peaks in November (21%) and January (24%). For the PDO influence on North American temperature departures, predictive skill is therefore potentially most useful in November through March when this

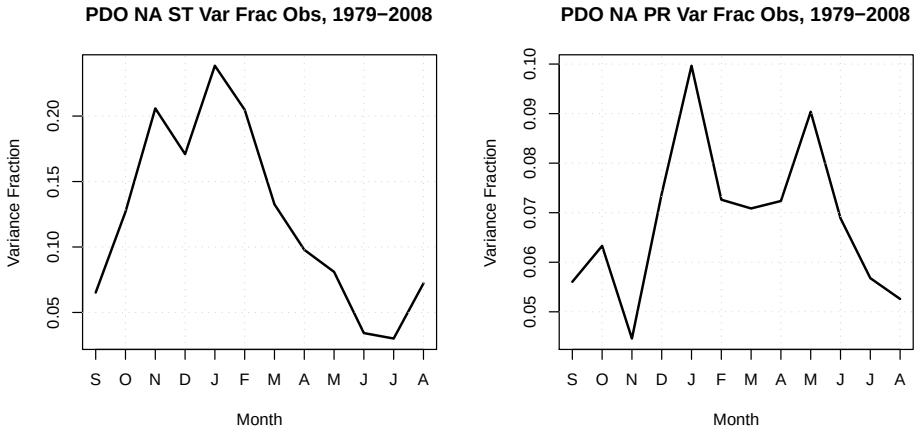

Figure 3.31: Explained variance of North American temperature (left) and precipitation (right) associated with the PDO in the observations.

influence is responsible for between 15% and 24% of the North American temperature variance for a perfect forecast. PDO associated North American temperature departures predicted by CHFP2 are skillful exclusively in December, January (zero, one month lead) and in March (zero lead) when the actual forecasts explain roughly 7.7%, 4.9% and 13.5% of the North American temperature variance (28%, 22% and 37% of the standard deviation).

On the other hand, the ERA40/ERA interim inferred PDO influence explains on average roughly 7% of the total North American precipitation variance (26% of the standard deviation). In this case, the observed annual cycle of explained variance peaks in October (6%), January (10%) and May (9%). For the PDO influence on North American precipitation departures, predictive skill is thus potentially most useful in the aforementioned months where the upper limit of the explained variance for a perfect forecast is enhanced. CHFP2 predicted PDO associated North American precipitation departures are skillful in October and in May for different lead months, when the actual forecasts explain up to roughly 0.8% (one month lead) and 1.1% (two month lead) of the North American precipitation variance (9% and 11% of the standard deviation).

ENSO Influence on North American Temperature and Precipitation

Following the same procedure used for the North Pacific influence on North American climate, the CHFP2 predicted influence of the tropical Pacific on North American climate is similarly verified against the observed influence inferred from ERA40/ERA interim. The annual cycle of the observed variance of the index measuring ENSO

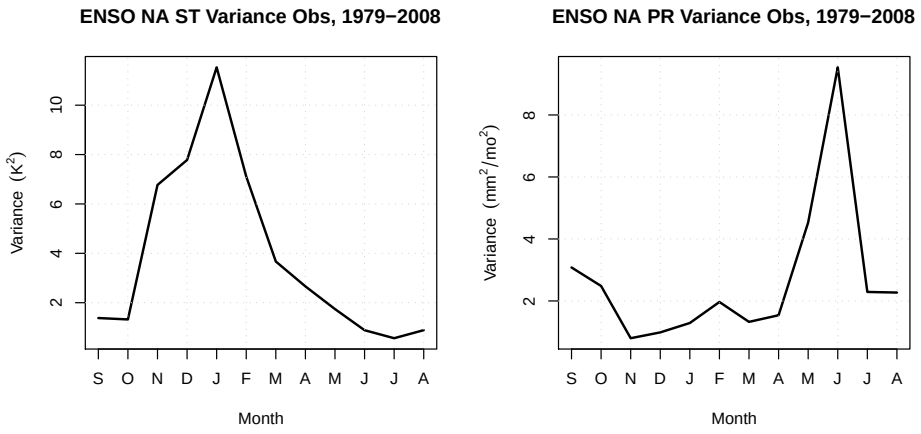

Figure 3.32: Observed variance of the ENSO influence $v(t)$ on North American temperature (left) and precipitation (right).

influence on North American temperature ($\hat{r}$ ranges between -0.6 K in the southern part and 0.9 K in the north-western part of North America) exhibits a sharp peak in January (Figure 3.32, left), when the variance of the corresponding PDO influence is also enhanced. On the other hand, the annual cycle of the variance of the observed ENSO influence on precipitation over North America ($\hat{r}$ ranges between -8 mm/month in the Great Lakes region and 20 mm/month in the south-eastern United States) peaks in June (Figure 3.28, right), along with the corresponding PDO influence, while it is relatively low in winter, when the corresponding PDO influence is more active (e.g., in January).

Temperature

The fidelity of CHFP2 to forecast ENSO associated temperature departures over North America measured by AC is shown in Figure 3.33. Averaged over the seasonal forecast range, correlation skill of CHFP2 to forecast the ENSO influence on

North American temperature departures is significantly positive, independent of the start month, and ranges between roughly 0.20 (June, December started forecast) and roughly 0.29 (September started forecast) (Table 3.9). The reason for the relatively high AC scores in winter is the fact that the ENSO signal is large and CHFP2 skill to forecast the sign of the PNA and NPI, i.e., the atmospheric ENSO reponse, is enhanced. High correlation skill in predicting the ENSO influence on North American temperature is also reached in boreal spring, when AC is significantly positive in March, April, May at different lead times for all start months.

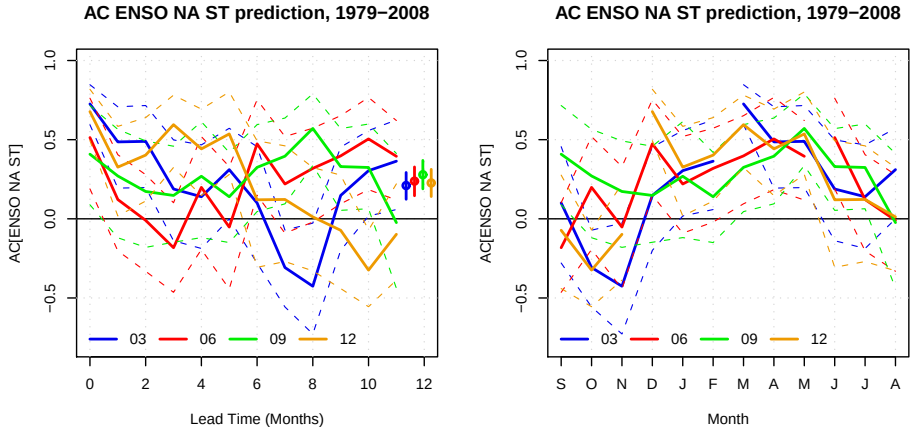

Figure 3.33: AC (solid lines) and bootstrapped 95% confidence interval (dashed lines) between the predicted and the observed ENSO influence on North American temperature index as a function of lead time where the dots, lines on the right show the mean, 95% confidence interval over the forecast range (left panel) and target month (right panel) for four different start months of the forecast (03: March; 06: June; 09: September; 12: December).

For reference, the standard error of the CHFP2 predicted ENSO influence on North American temperature verified against the observed influence can be consulted in the Appendix (Figure A.15). The standard error averaged over the course of a forecast is roughly 1.5–1.6 K (Table A.1). The error growth for all forecast start months peaks in January. The fidelity of CHFP2 to forecast ENSO associated temperature anomalies over North America measured by the MSSS is found in the Appendix (Figure A.16). Here, the highest MSSS is roughly 0.5. This indicates that the variance of the predicted North American temperature anomalies associated with ENSO and

thus their magnitude is underestimated compared to the observed. One reason for this bias is the fact that the ENSO magnitude in CanCM3, employed in CHFP2, is moderately below the observed. Another is that the variance of the ensemble mean will tend to become smaller as the magnitude of the predictable signal diminishes.

Precipitation

Finally, the correlation skill of CHFP2 to forecast the ENSO influence on precipitation departures over North America is shown in Figure 3.34. Averaged over the seasonal forecast range, the AC of this system is significantly positive and of roughly 0.26 for all start months (Table 3.9). However, in terms of ENSO associated North American winter (DJF) precipitation departures, e.g., they can only be skillfully predicted by forecasts initialized in December. Another case of significant correlation skill is evident in July at different lead times.

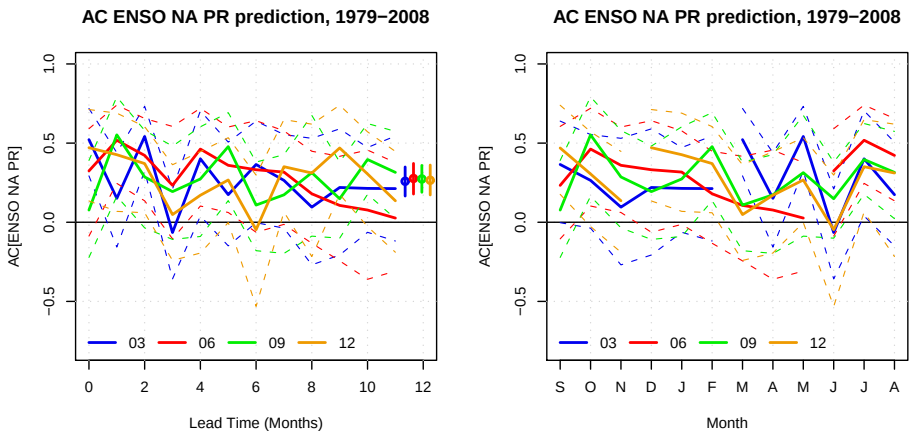

Figure 3.34: AC (solid lines) and bootstrapped 95% confidence interval (dashed lines) between the predicted and the observed ENSO influence on North American precipitation index as a function of lead time where the dots, lines on the right show the mean, 95% confidence interval over the forecast range (left panel) and target month (right panel) for four different start months of the forecast (03: March; 06: June; 09: September; 12: December).

For reference, the standard error of the CHFP2 predicted ENSO influence on North American precipitation verified against the observed influence can be consulted

in the Appendix (Figure A.17). Here, the standard error averaged over the course of a forecast is roughly 1.5 mm/month (Table A.1) for all start month. The SDE peaks in June independently of the start month. The performance of CHFP2 to forecast ENSO associated precipitation anomalies over North America measured by the MSSS is found in the Appendix (Figure A.18). As for temperature, the MSSS does not reach high values due to an underestimated variance of the predicted index considered relative to the observed. One origin of this variance bias is the ENSO magnitude in CHFP2, mentioned previously, that is moderately below the observed.

To sum up the ability of CHFP2 to forecast the ENSO influence over North America, seasonal CHFP2 forecasts of both ENSO associated temperature and precipitation departures are significantly positive for all start months in terms of correlation skill averaged over the 12-month forecast range. In CHFP2 at the seasonal time scale, ENSO is thus a good predictor for both North American temperature as well as precipitation.

Explained Variance

The potential usefulness of the predictive skill is again inferred from the ENSO-related variance of the concerned variable in ERA40/ERA interim, derived in a similar way as the PDO-related variance discussed previously. The seasonal cycles of the ENSO-related variance of both North American temperature and precipitation with respect to the total variance are shown in Figure 3.35. The observed ENSO influence explains roughly 11% of the North American temperature variance (33% of the standard deviation). Here, the observed seasonal cycle of explained variance peaks in November (23%) and January (27%). As for the PDO influence, for the ENSO influence on anomalous North American temperature, predictive skill is potentially most useful in November through March when this influence is responsible for between 11% and 27% of the North American temperature variance for a perfect forecast.

ENSO-related North American temperature departures in December, January and February, e.g., are skillfully predicted by CHFP2 forecasts initialized exclusively in December. In these months (DJF), the actual forecast explains roughly 4.7%, 3.2% and 2.8% of the North American temperature variance (22%, 18% and 17% of the standard deviation). On the other hand, ENSO associated North American temperature departures in spring (MAM), are skillfully predicted by all the forecasts independently of the start month. In this case (MAM), the actual forecast initialized

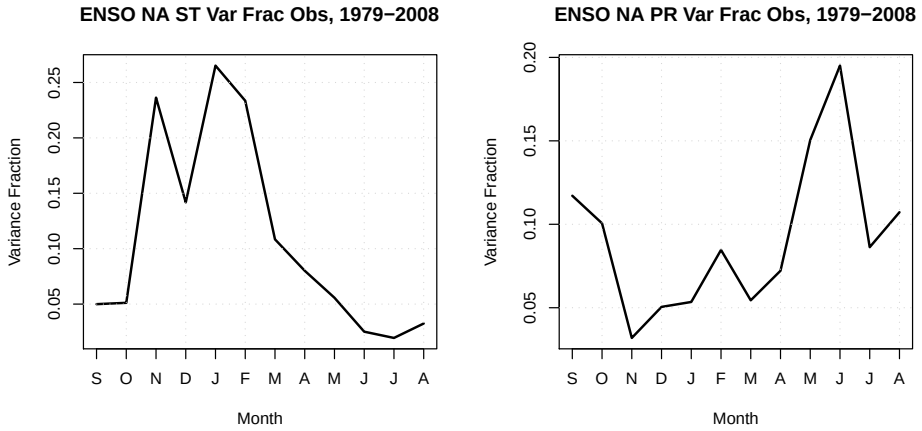

Figure 3.35: Explained variance of North American temperature (left) and precipitation (right) associated with ENSO in the observations.

in March explains roughly 17.0%, 2.2% and 1.3% of the North American temperature variance (41%, 15% and 11% of the standard deviation).

On the other hand, the ERA40/ERA interim inferred ENSO influence explains on average roughly 9% of the total North American precipitation variance (30% of the standard deviation). Here, the observed annual cycle of explained variance peaks in May (15%), June (20%) and September (12%). In contrast to the PDO influence, in terms of the ENSO influence on anomalous North American precipitation, predictive skill of a perfect forecast is potentially most useful in May, June and September and least useful in NDJFM. CHFP2 predicted North American precipitation departures associated with ENSO are skillful in May (March initialized forecasts) and in September (December initialized forecasts) when the actual forecasts explain 0.8% and 1.9% of the North American precipitation variance (9% and 14% of the standard deviation).

To sum up, I am highlighting the key results in this section on the CHFP2 prediction of the Pacific influence on North American climate.

- The PDO explains 12% and 7% of the North American temperature and precipitation variance. ENSO explains 11% and 9% of the North American temperature and precipitation variance.

- The PDO is a better predictor for North American precipitation (12-month

averaged AC scores skillful for all four start seasons) than temperature (12-month averaged AC scores skillful for one out of four start seasons).

- ENSO is a good predictor for both precipitation and temperature (12-month averaged AC scores skillful for all four start seasons).

3.3 Decadal Prediction

The PDO skill of DHFP1 on interannual and decadal time scales is inferred from a set of ten-year range hindcasts (i.e., retrospective "forecasts"). Forecasts with an ensemble size of ten are initialized on January 1st every five years from 1961–1996. The verification period for these eight CMIP5-type decadal forecasts during which they can be compared to the observational dataset extends therefore from 1961–2005. In this section, the skill of DHFP1 in predicting the evolution of the PDO is based on annual mean SST anomalies. At each grid point, a linear trend has been removed from the observed SSTs for the verification period prior to identifying the leading mode using EOFs.

In DHFP1, the SDE and MSSS in predicting the PDO is shown in (Figure 3.36, top). The MSSS varies substantially for different start years indicated by the bootstrapped 95% confidence interval. Over the course of a decadal PDO forecast, the MSSS never reaches values that are significantly positive. The MSSS average over the decadal forecast range (mean and confidence interval on the right in MSSS panel) is thus not statistically distinguishable from zero either. DHFP1 AC skill in predicting the PDO is positive during the first three years of the forecast before it falls below zero in the following year (Figure 3.36, bottom). The correlation skill in first year is the only case where PDO skill is significantly above zero. The average AC over the ten-year forecast range (on the right in AC panel) is roughly zero.

A different approach to express skill in decadal climate forecasts is taken in Figure 3.37. Here, the AC of the predicted PDO index averaged over lead time is shown (i.e., $\overline{0}$, $\overline{01}$, $\overline{012}$, $\overline{0123}$, $\overline{01234}$, ...). In this case, the correlation skill of the index averaged over lead time is positive during the first three years. Here, the bootstrapped 95% confidence interval indicates that the AC is significantly positive in the first three years reaching zero skill at roughly six years into the forecasts. This means that DHFP1 is expected to skillfully predict the future three year averaged evolution of the PDO index, but not the evolution of the index in each year individually.

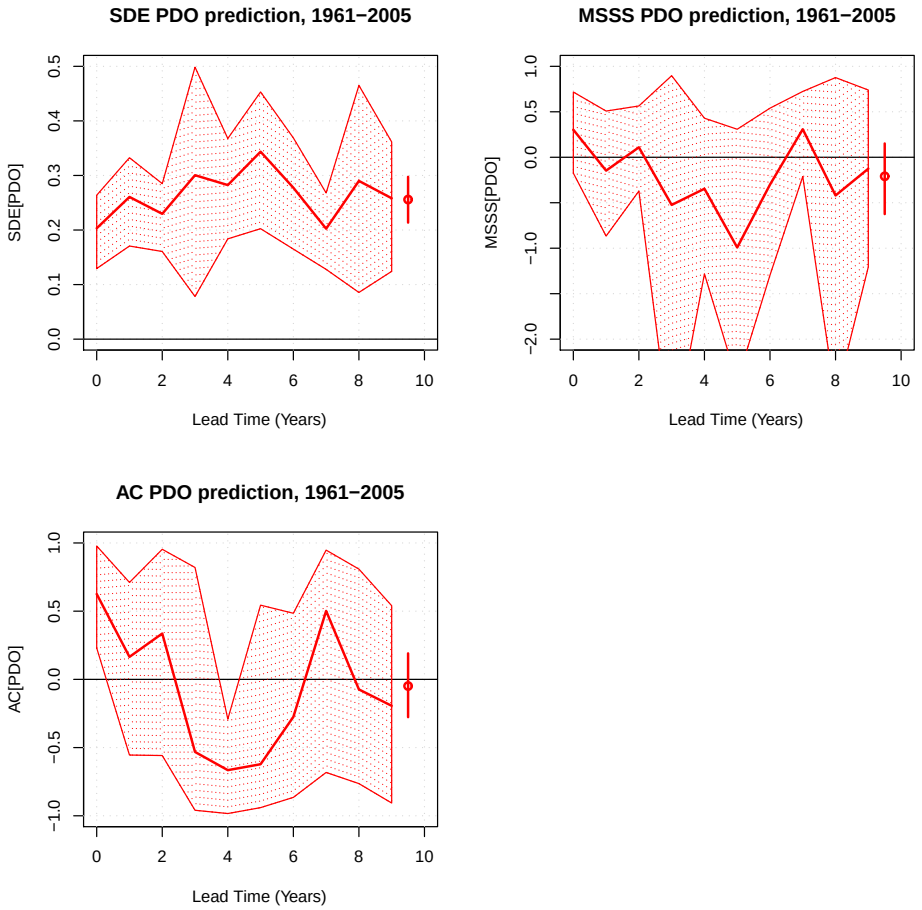

Figure 3.36: SDE, MSSS, AC and bootstrapped 95% confidence interval between the predicted and the observed PDO index as a function of lead time in years where the dots, lines on the right show the mean, 95% confidence interval over the forecast range.

3.4 Conclusions and Discussion

The skill of the first Canadian dynamical PDO prediction study employing a coupled climate model initialized with observations to predict the historical PDO evolution has been assessed. The extensive set of retrospective "forecasts" serves as a basis to investigate the extratropical climate prediction problem on seasonal to decadal time scales. The skill in these single-model hindcasts provides a benchmark on how skillful the future evolution of the PDO could be predicted by this climate data assimilation and prediction system once operational.

CHFP2 seasonal PDO forecasts measured by both the MSSS (mean roughly 0.23) and anomaly correlation skill (mean roughly 0.47) are significantly positive on a 95%

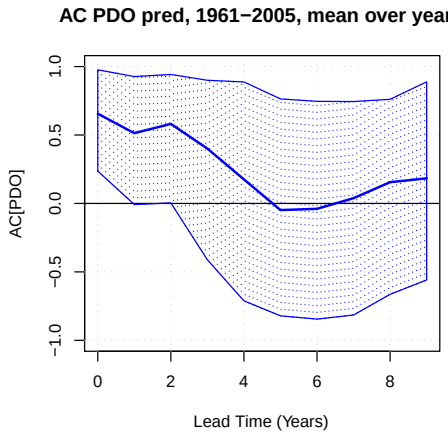

Figure 3.37: AC and bootstrapped 95% confidence interval between the predicted PDO index averaged over lead years and the observed PDO index averaged over lead years ($\overline{0}$, $\overline{01}$, $\overline{012}$, $\overline{0123}$, $\overline{01234}$, ...).

confidence level for all start months when averaged over the seasonal forecast range. This system is successful at predicting with significant skill the first 14 EOF modes of North Pacific SST departures that explain roughly 74% of the total variance. In this case, correlation skill of the predicted leading 14 EOF modes averaged over the seasonal forecast range stays significantly above zero independently of the season the forecast is initialized. Besides the PDO, CHFP2 therefore skillfully predicts the Victoria mode (second EOF mode of North Pacific SST departures) at the seasonal time scale. The Victoria mode coincides with dramatic ecological shifts in the northeast Pacific (Di Lorenzo et al. [2008]) whose prediction can be useful for other fields of research as well as societies in the region concerned. On the other hand, CHFP2 is less successful at predicting North Pacific SSTs, i.e., the combination of all the EOF modes, at the seasonal time scale. For all start months, CHFP2 North Pacific SST correlation skill averaged over the seasonal forecast range is significantly lower than its skill in predicting the PDO as well as the Victoria mode.

In CHFP2, seasonal PDO forecasts measured by AC are significantly less skillful than seasonal ENSO forecasts for all start seasons. However, correlation skill of the most skillful seasonal PDO forecast initialized in June is about as skillful (0.58) as the least skillful ENSO (0.62) forecast initialized in December. Their performance is statistically indistinguishable.

In this climate data assimilation and prediction system, seasonal PDO forecasts initialized in June are significantly more skillful than March initialized forecasts due to the PDO prediction barrier in May and June. The annual cycle of observed PDO

variance peaks in May and June when substantial North Pacific storm track activity coincides with a shallow North Pacific mixed layer. Enhanced PDO variance in May and June generated by atmospheric weather "noise" unpredictable at the seasonal time scale, appears to pose a prediction barrier for the PDO. March initialized forecasts show a degraded skill because they are initialized before the PDO prediction barrier in May and June. On the other hand, forecasts initialized in June during the PDO prediction barrier in May and June benefit from reduced weather "noise" leading to reduced standard error growth and thus a more skillful MSSS and AC.

Another potential mechanism that might affect ocean memory and thus limit extratropical predictive skill in CHFP2 at the seasonal time scale are the varying effects of storm track activity. Variations in North Pacific storminess appear to impact PDO skill by means of a lagged response of the ocean mixed layer to weather "noise" unpredictable at the seasonal time scale. In CHFP2, times of increasing North Pacific storm track activity are followed by times of reduced PDO skill. On the other hand, the North Pacific midwinter suppression of storm track activity with decreasing storminess is followed by a substantial recovery in PDO skill.

In addition to skill in Pacific SST, CHFP2 is also successful at predicting indices that measure the atmospheric circulation regime over the North Pacific and North America such as the PNA and NPI. Averaged over the course of a seasonal forecast, PNA AC skill is smaller than the PDO AC skill but significantly positive for forecasts initialized in March, June and December. Previous studies have focused primarily on short lead PNA forecasts (Palmer et al. [2004]). Some of the CHFP2 forecasts, however, produce skillful (AC) PNA predictions even at relatively long leads. This system is more successful at predicting the NPI as measured by AC than the PNA. Here, forecasts exhibit significant 12-month averaged AC skill independently of the start season.

The influence of Pacific SST on North American climate in the observation-based reanalysis varies over the course of a year. While PDO-related and ENSO-related North American temperature departures are usually most prominent in winter, North American precipitation departures associated with the PDO and ENSO are usually prominent in May and June as well.

CHFP2 is capable of predicting part of the influence of Pacific SST on North American climate. Measured by AC averaged over the seasonal forecast range, in CHFP2 the PDO is a better predictor for North American precipitation than temperature. In this case, only one out of four forecast start seasons produces a skillful

forecast of North American temperature departures associated with the PDO. On the other hand, all four forecast start seasons produce a skillful forecast of North American precipitation departures associated with the PDO. In CHFP2, ENSO is a better predictor for North American temperature than the PDO. Both ENSO and the PDO are, however, good predictors for North American precipitation. Averaged over the seasonal forecast range, CHFP2 predictions of both North American temperature and precipitation departures associated with ENSO are significantly positive for all start months.

In the observation-based reanalysis, the PDO influence explains on average roughly 12%, 7% of the total temperature, precipitation variance in North America (35%, 26% of the total temperature, precipitation standard deviation). While both the PDO associated temperature and precipitation departures explain the highest fraction of total variance in January (24%, 10%), only PDO associated precipitation departures exhibit a second peak in spring where the variance fraction in May reaches 9%. PDO associated North American temperature departures predicted by CHFP2 are skillful in December, January (zero, one month lead) and in March (zero lead) when the actual forecasts explain roughly 7.7%, 4.9% and 13.5% of the North American temperature variance (28%, 22% and 37% of the standard deviation). On the other hand, CHFP2 skillfully predicts PDO associated precipitation departures in May (two months lead) when the actual forecast explains roughly 1.1% of the North American precipitation variance (11% of the standard deviation).

Finally, the ENSO influence explains on average roughly 11%, 9% of the total North American temperature, precipitation variance in the reanalysis (33%, 30% of the total temperature, precipitation standard deviation). The ENSO-related temperature variance fraction peaks as expected in January (27%). The ENSO-related precipitation variance fraction, however, peaks in May (15%) and June (20%). CHFP2 prediction of ENSO associated North American temperature departures are skillful (initialized in December) during winter when the actual forecast explains roughly 4.7%, 3.2% and 2.8% of the North American temperature variance (22%, 18% and 17% of the standard deviation). On the other hand, CHFP2 prediction of ENSO-related North American precipitation departures are skillful in May (initialized in March) when the actual forecast explains 0.8% of the North American precipitation variance (9% of the standard deviation).

In DHFP1, PDO correlation skill in decadal forecasts is positive in the first three years followed by negative correlation between four and seven years with a recovery

eight years into the forecast. PDO AC skill is significantly positive exclusively during the first year of a DHFP1 forecast. Decadal PDO forecasts show correlation skill significantly above zero in the first three years when the index is averaged over lead years. In other words, DHFP1 is expected to skillfully predict the future three year averaged evolution of the PDO, but not the evolution in each year individually.

The discussed seasonal PDO prediction results based on single-model systems are likely to be outperformed by the two-model system in development with two coupled models based on different atmospheric models (CanAM3 and CanAM4). Multi-model ensemble climate data assimilation and prediction systems are known to be more skillful with a reduced uncertainty in both the tropics and extratropics than single-model systems (Kharin and Zwiers [2002], Palmer et al. [2004], Weisheimer et al. [2009]). In addition, three-dimensional ocean temperature and salinity assimilation before the start of each forecast could improve decadal forecasts of the PDO reported here, and such forecasts are being carried out for CMIP5. In recent years, more information on three-dimensional ocean conditions based on a network of floats like in the Argo project has become available shortly after the measurement has taken place. With an improved coverage of high-quality ocean observations, forecasts of the future evolution of extratropical modes of climate variability such as the PDO might be more skillful than in the discussed hindcasts.

Chapter 4

Conclusions and Discussion

In this thesis I have investigated the ability of 13 global climate models to reproduce observed characteristics of the PDO, the leading EOF mode of North Pacific SST anomalies. I have also investigated the tropical and extratropical origin of the PDO as well as its influence on climate departures over North America (first part). The skill of one such global climate model initialized with observations in predicting the future evolution of the PDO has also been assessed (second part).

In the first part of this thesis, I have shown that these 13 global climate models as a group are successful at realistically simulating the pattern of the PDO whose correlation with the observed pattern is roughly 0.8. The modeled magnitude of the PDO signal, measured by the variance of the PDO index, is overestimated by roughly 33%, and the index has more power at lower frequencies (is "redder") than inferred from the observational dataset. In the global climate models, the simulated response to ENSO forcing is delayed on average by about 1.5 months more than the observed response, a tendency that is consistent with model biases toward deeper oceanic mixed layers in winter and spring and weaker air-sea feedbacks in the winter half-year. Model biases in mixed layer depths and air-sea feedbacks are also associated with a model mean ENSO-related signal in the North Pacific whose amplitude is overestimated by roughly 30%. Finally, the simulated North Pacific variability is "redder" due to model errors originating in the tropics and extratropics.

These results have implications for the dynamical prediction of North Pacific climate departures based on climate data assimilation and prediction systems employing global climate models. Because the simulated North Pacific response lags ENSO unrealistically, seasonal forecasts may tend to exhibit insufficient North Pacific responses to developing El Niño and La Niña events in the first few forecast months. At longer

forecast lead times, North Pacific SST anomalies driven by ENSO may tend to be overestimated in models having an overly strong ENSO as the models drift away from observation-based initial conditions and this bias sets in. Finally, the relative preponderance of low frequency variability in the models suggests that climate forecasts may tend to overestimate decadal to multi-decadal variability in the North Pacific.

I have reported that the observed influence of the PDO on anomalous temperature over North America with warm anomalies often occurring in the north west and cold anomalies in the south east are the sum of both the north-south contrast in the ENSO-related and east-west contrast in the influence of the extratropical part of the PDO. The climate models as group capture this observed relationship reasonably well. Besides, the climate models realistically reproduce some larger-scale features of the influence of the PDO, its tropical Pacific related and, to a lesser extent, its extratropical part on North American precipitation departures.

In the second part of this thesis, I have established the performance of the first Canadian dynamical PDO prediction study employing a coupled climate model carefully initialized with observations (CHFP2). Based on an extensive set of hindcasts, this climate data assimilation and prediction system is successful at predicting the historical evolution of the PDO at the seasonal time scale. Both the MSSS (mean roughly 0.23) and anomaly correlation skill (mean roughly 0.47) of the PDO forecasts are significantly positive on a 95% confidence level (using the bootstrap) for all start seasons when averaged over the seasonal forecast range. In addition to the skill in the PDO, i.e., the leading EOF mode, CHFP2 is capable of forecasting the leading 14 EOF modes of North Pacific SST departures. In this case, 12-month averaged correlation skill of CHFP2 forecasts of the first 14 EOF modes of North Pacific SST departures, that explain roughly 74% of the total SST variance, is significantly above zero for all start seasons. On the other hand, CHFP2 is less successful at predicting North Pacific SSTs, i.e., the sum of all EOF modes, at the seasonal time scale. Here, CHFP2 North Pacific SST correlation skill averaged over the seasonal forecast range is significantly lower than its skill in predicting, e.g., the leading EOF mode, independently of the season the forecast is initialized.

CHFP2 is therefore also successful at predicting the Victoria mode, i.e., the second EOF mode of North Pacific SST departures, at the seasonal time scale. The Victoria mode coincides with dramatic ecological shifts in the northeast Pacific (Di Lorenzo et al. [2008]) not related to the PDO. Beyond the impacts on the physical state of the North Pacific, both the PDO and the Victoria mode also affect North Pacific

ecosystems. The prediction of the future evolution of the PDO and the Victoria mode can thus be useful for other fields of research as well as societies and stakeholders in the region concerned.

The annual cycle of observed PDO variance peaks in May and June when substantial North Pacific storm track activity coincides with a shallow oceanic mixed layer. Enhanced PDO variance in May and June generated by atmospheric weather "noise" unpredictable at the seasonal time scale appears to pose a prediction barrier for the PDO. Seasonal CHFP2 forecasts of the PDO initialized in June are thus significantly more skillful than March initialized forecasts. PDO skill depends not only on the start month but also varies as a function of the target month. Variations in North Pacific storminess appear to impact PDO skill by means of a lagged response of the ocean mixed layer to weather "noise". In CHFP2, times of increasing North Pacific storm track activity are followed by times of reduced PDO skill. On the other hand, the North Pacific midwinter suppression of storm track activity with decreasing storminess is followed by a substantial recovery in PDO skill.

Besides the discussed skill in tropical and extratropical Pacific SST, CHFP2 is successful at predicting indices measuring the atmospheric circulation regime over the North Pacific and North America such as the PNA and NPI that respond to Pacific SST departures. Averaged over the course of a seasonal forecast, PNA AC skill is smaller than the PDO AC skill but significantly positive for forecasts initialized in three out of four start seasons. Previous studies have focused primarily on short lead PNA forecasts (Palmer et al. [2004]). Some of the CHFP2 forecasts, however, produce skillful (AC) PNA predictions even at relatively long leads. Finally, CHFP2 is more successful at predicting the sign of the NPI measured by AC than the PNA. In this case, forecasts exhibit significant 12-month averaged AC skill initialized in all four start seasons.

In this thesis, I have shown that the influence of Pacific SST on North American climate in the observation-based reanalysis varies over the course of a year. Whereas PDO-related and ENSO-related North American temperature departures are usually most prominent in winter, North American precipitation departures associated with the PDO and ENSO are usually prominent in May and June as well. The PDO influence explains on average roughly 12%, 7% of the total temperature, precipitation variance in North America (35%, 26% of the total temperature, precipitation standard deviation), while the ENSO influence explains on average roughly 11%, 9% of the total North American temperature, precipitation variance (33%, 30% of the total

temperature, precipitation standard deviation).

I have verified CHFP2 forecasts against the observation-based reanalysis and found that this system is capable of predicting part of the influence of Pacific SST on North American climate. Measured by AC scores averaged over the seasonal forecast range, in CHFP2 the PDO is a better predictor for North American precipitation than temperature. In this case, only one out of four forecast start season produces a skillful forecast of North American temperature departures associated with the PDO. On the other hand, all four forecast start seasons produce a skillful forecast of North American precipitation departures associated with the PDO. In CHFP2, ENSO is a better predictor for North American temperature than the PDO. Both ENSO and the PDO are, however, good predictors for North American precipitation. Averaged over the seasonal forecast range, AC skill of CHFP2 predictions of both North American temperature and precipitation departures associated with ENSO are significantly positive for all start seasons.

The presented CHFP2 results show that seasonal climate forecasts over North America employing coupled ocean-atmosphere climate models benefit from initializing the coupled system with observations. This climate data assimilation and prediction system is expected to be skillful in forecasting future likelihoods of North American temperature departures from the long-term climatology such as cold spells or heat waves associated with ENSO and to a lesser extent the PDO. In addition, CHFP2 is expected to be skillful in forecasting future likelihoods of departures in North American precipitation such as floods or droughts associated with both ENSO and the PDO. The CHFP2 performance also indicates that climate data assimilation and prediction systems that are successful at predicting ENSO and the PDO are expected to produce more skillful seasonal climate forecasts over North America than systems that are less successful at predicting ENSO and the PDO.

The ability of DHFP1 to predict the PDO at the decadal time scale is very limited. PDO correlation skill is significantly positive exclusively during the first year of a decadal PDO forecast. Decadal PDO forecasts show correlation skill significantly above zero in the first three years when the predicted index is averaged over lead years. In other words, DHFP1 is expected to skillfully predict the future three year averaged evolution of the PDO, but not the evolution in each year individually.

Recent efforts on advancing extratropical climate prediction on seasonal, interannual and decadal time scales employing coupled climate models face multiple challenges. Due to the overall small signal to noise ratio in the extratropics, models,

initialization procedures and the quality of ocean observations need to be improved in order to be able to better predict some of the future climate departures from the climatology at the seasonal time scale and to extend skillful extratropical predictions beyond 12 months. In order to address the extratropical climate prediction problem, multi-model climate data assimilation and prediction systems are obviously needed to advance extratropical climate prediction. Multi-model ensembles are believed to provide more skillful tropical and extratropical climate predictions with a reduced uncertainty than single-model systems (Kharin and Zwiers [2002], Palmer et al. [2004], Weisheimer et al. [2009]).

Appendix A

Supplemental Information

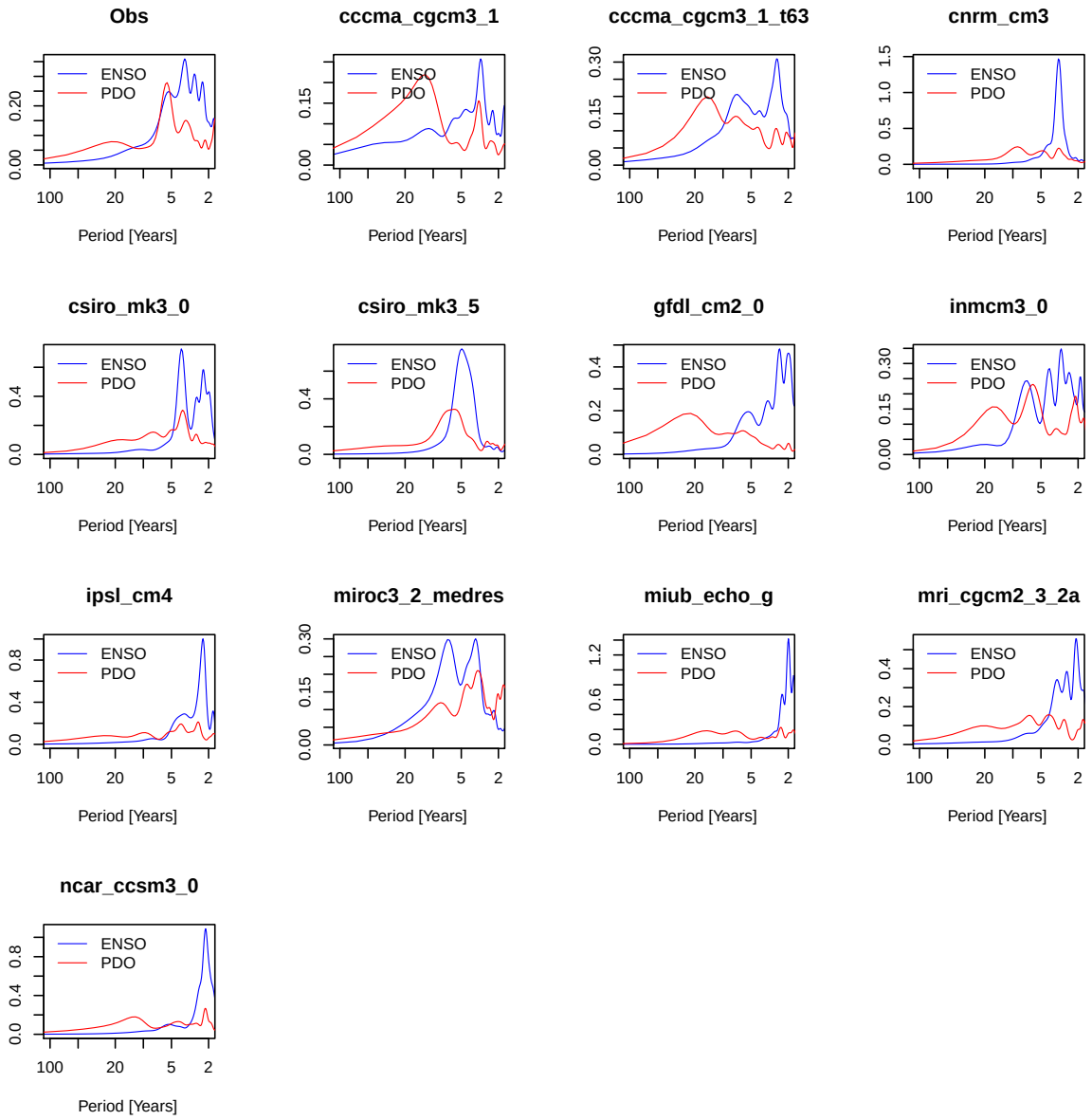

Figure A.1: Variance preserving (frequency·power) ENSO and PDO power spectra in the observations (ERSST3b) and individual models.

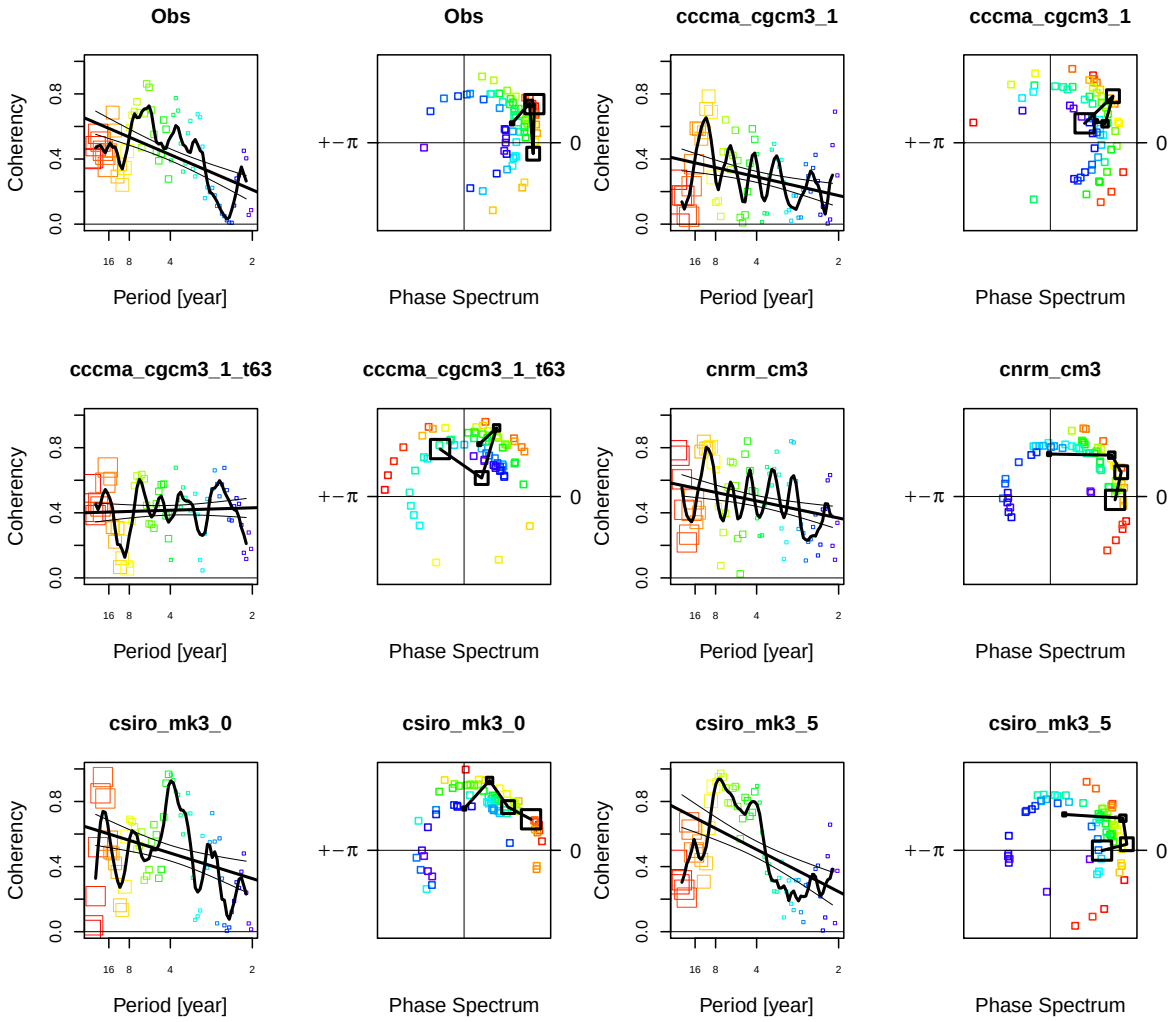

Figure A.2: Squared coherence and phase spectrum between ENSO and the PDO in the observations (ERSST3b) and individual models. The thick black line in the coherence panels shows the smoothed coherence, using a running mean window of 5 spectral bins of estimates of coherence (squares). The straight black line shows the linear regression of the smoothed coherence accompanied by the 95% confidence interval (thin black lines). The estimates of coherence (squares) are color coded, red indicates low frequencies, purple indicates high frequencies. The same applies to the phase spectrum. The phase spectrum displays the imaginary vs. the real part of the phase (from -π to π) between the two signals. Both components in the phase spectrum have been multiplied by 1-frequency yielding a spectral spiral. The phase of the corresponding coherency at low frequencies (red) is outside whereas the phase of the corresponding coherency at high frequencies (purple) is inside the spiral. Points at 0 represent an in phase relationship at the corresponding frequency whereas points at $\pm\pi$ represent an out of phase relationship. In the coherence plots, four different box sizes indicate the four spectral bins for which the corresponding boxes in the phase spectrum have been spatially averaged and displayed by black boxes that are connected by a black line.

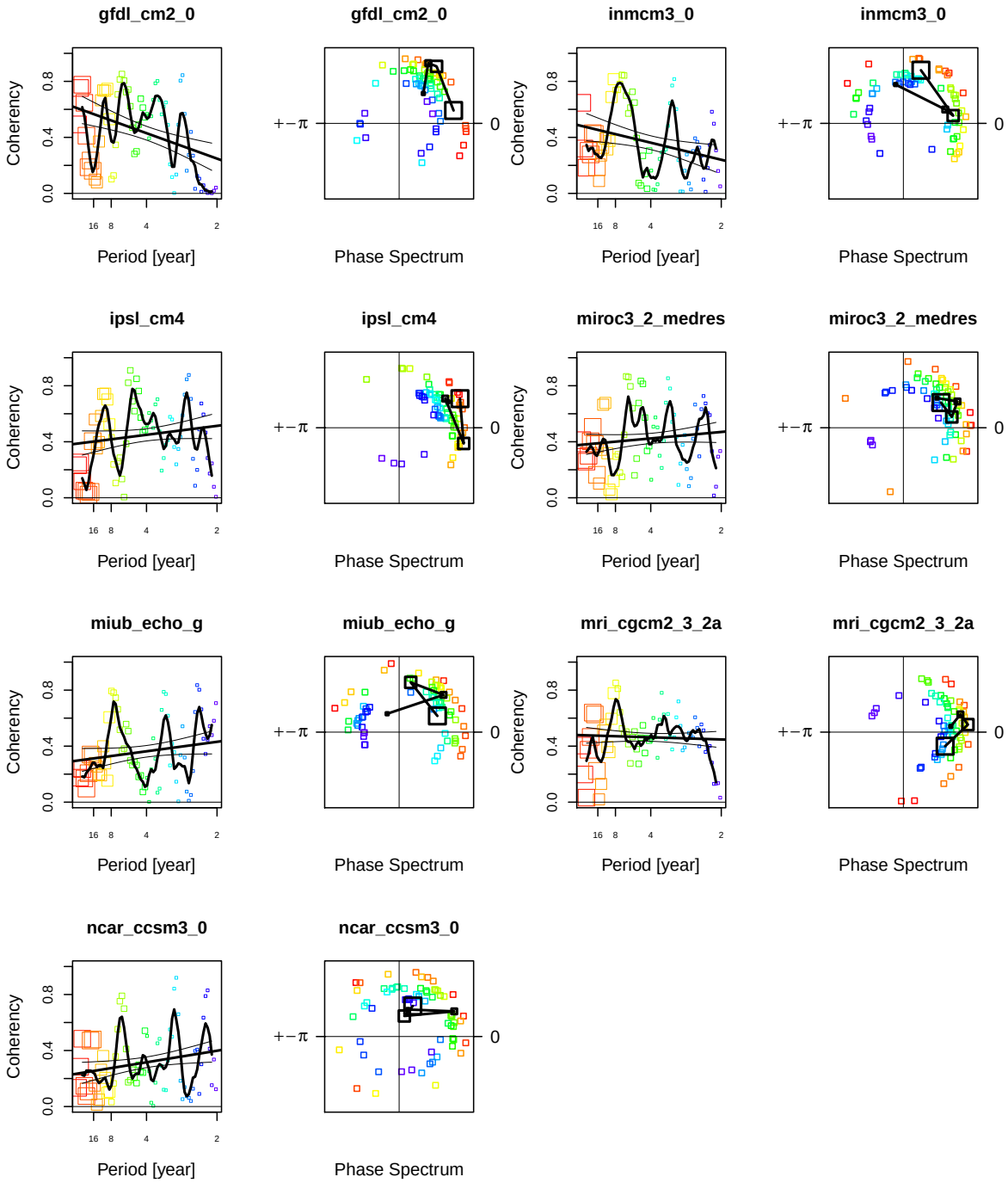

Figure A.3: Figure A.2 continued.

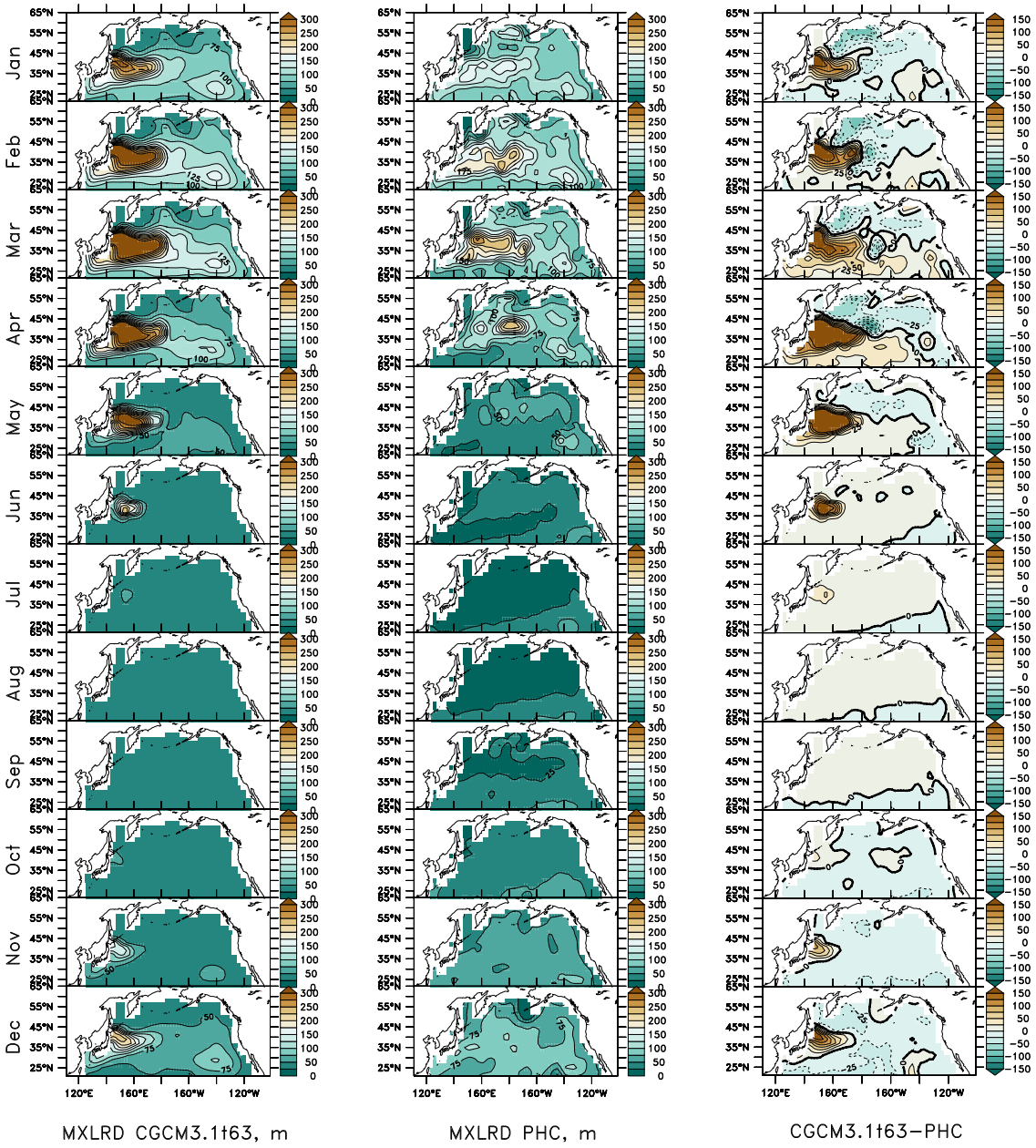

Figure A.4: North Pacific mixed layer depths in meters in the CGCM3.1t63 CMIP3 model (left) and observed (middle), and the difference between the model and observations (right).

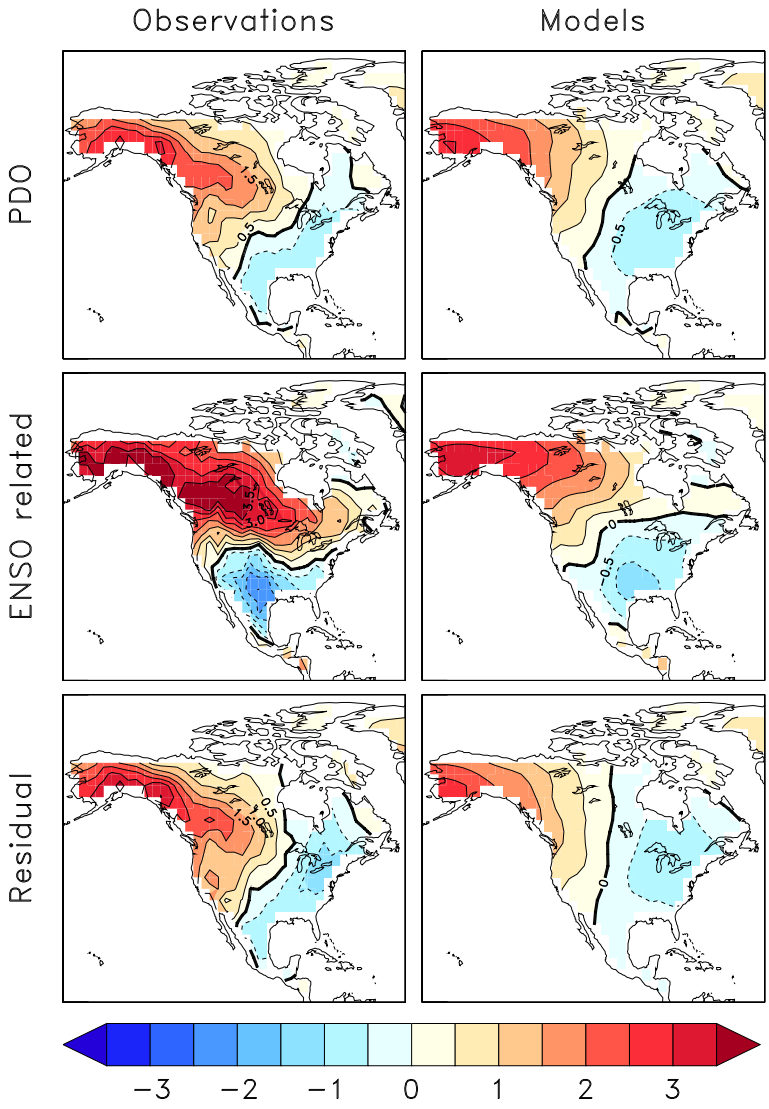

Figure A.5: Linear regression of anomalous surface temperature (K) onto $T_{PDO}(t)$ (top). Linear regression of anomalous surface temperature onto $T_{ENSO}(t)$ (middle). Linear regression of anomalous surface temperature onto $T_{RES}(t)$ where $T_{RES}(t) = T_{PDO}(t) - T_{ENSO}(t)$ (bottom).

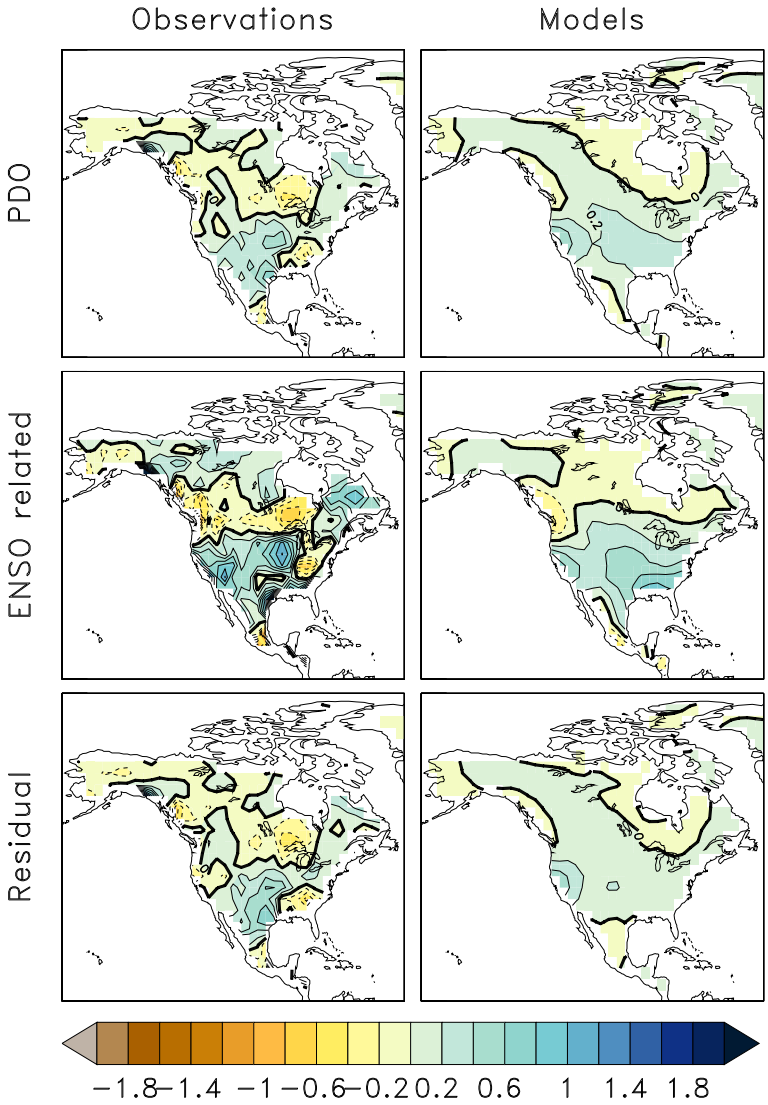

Figure A.6: As Figure A.5, but for anomalous precipitation (mm/d).

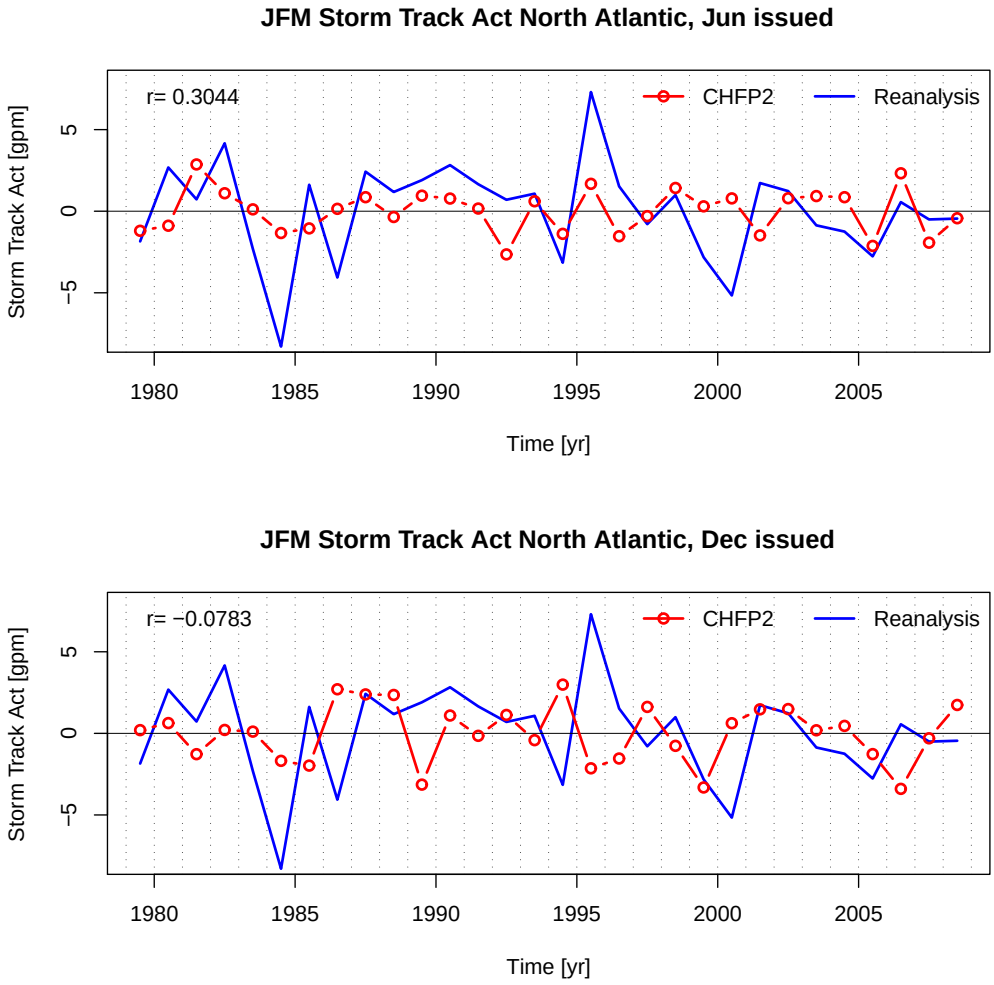

Figure A.7: North Atlantic annual storm track activity (mean of January, February, March) in ERA40/ERA interim (blue) and predicted by CHFP2 forecasts (red) issued in June (top), and December (bottom), respectively.

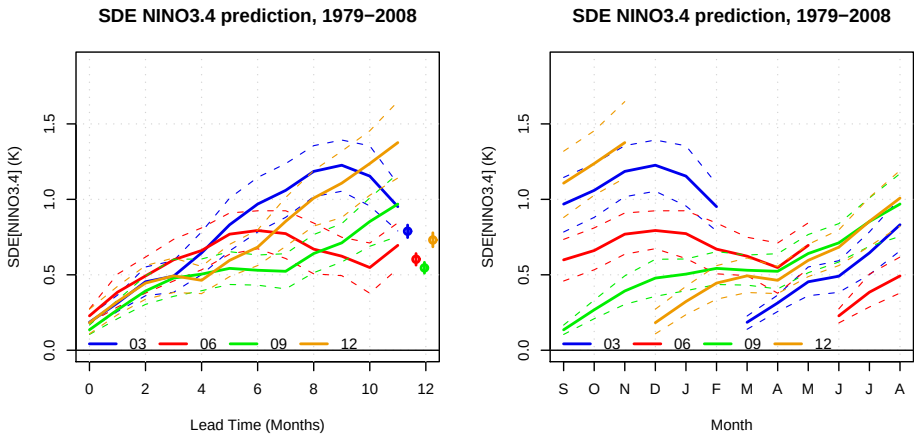

Figure A.8: SDE (solid lines) and bootstrapped 95% confidence interval (dashed lines) between the predicted and the observed NINO3.4 index as a function of lead time where the dots, lines on the right show the mean, 95% confidence interval over the forecast range (left panel) and target month (right panel) for four different start months of the forecast (03: March; 06: June; 09: September; 12: December).

Table A.1: Mean SDE over 12-month forecast range indicated by the overbar for the prediction of the PDO influence on North American temperature (K), precipitation (mm/mo), and of the ENSO influence on North American temperature (K), precipitation (mm/mo).

Month	$\overline{SDE}$ PDO T	$\overline{SDE}$ PDO PR	$\overline{SDE}$ ENSO T	$\overline{SDE}$ ENSO PR
03	0.91	1.11	1.69	1.47
06	0.93	1.10	1.68	1.43
09	0.91	1.14	1.69	1.46
12	0.84	1.13	1.64	1.45

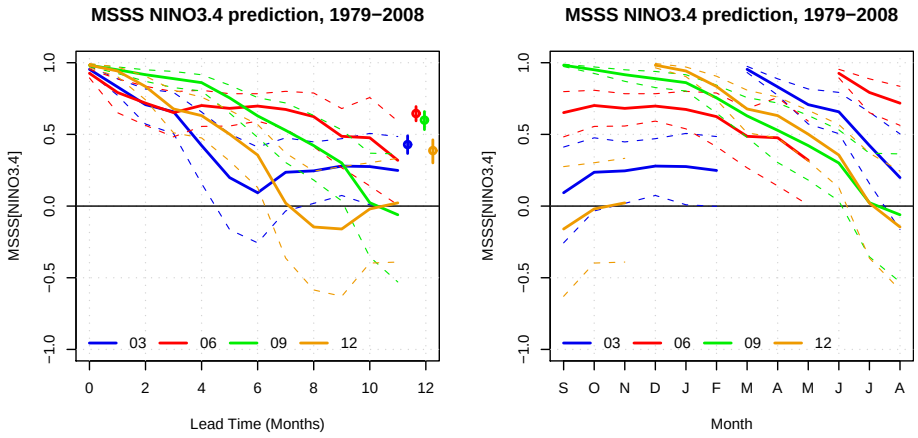

Figure A.9: MSSS (solid lines) and bootstrapped 95% confidence interval (dashed lines) between the predicted and the observed NINO3.4 index as a function of lead time where the dots, lines on the right show the mean, 95% confidence interval over the forecast range (left panel) and target month (right panel) for four different start months of the forecast (03: March; 06: June; 09: September; 12: December).

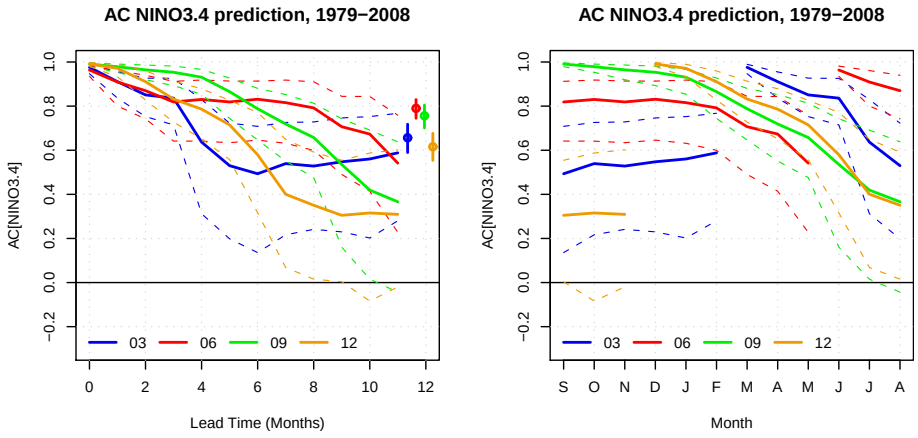

Figure A.10: AC (solid lines) and bootstrapped 95% confidence interval (dashed lines) between the predicted and the observed NINO3.4 index as a function of lead time where the dots, lines on the right show the mean, 95% confidence interval over the forecast range (left panel) and target month (right panel) for four different start months of the forecast (03: March; 06: June; 09: September; 12: December).

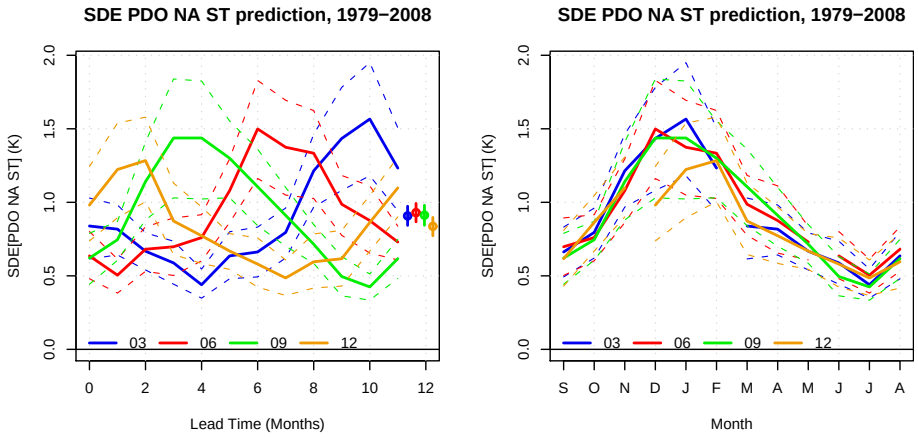

Figure A.11: SDE (solid lines) and bootstrapped 95% confidence interval (dashed lines) between the predicted and the observed PDO influence on North American temperature index as a function of lead time where the dots, lines on the right show the mean, 95% confidence interval over the forecast range (left panel) and target month (right panel) for four different start months of the forecast (03: March; 06: June; 09: September; 12: December).

Table A.2: Mean MSSS over 12-month forecast range indicated by the overbar for the prediction of the PDO influence on North American temperature, precipitation, and of the ENSO influence on North American temperature, precipitation.

Month	$\overline{MSSS}$ PDO T	$\overline{MSSS}$ PDO PR	$\overline{MSSS}$ ENSO T	$\overline{MSSS}$ ENSO PR
03	-0.09	0.05	0.04	0.06
06	-0.19	0.07	0.04	0.09
09	-0.09	0.00	0.09	0.06
12	0.00	0.06	0.06	0.09

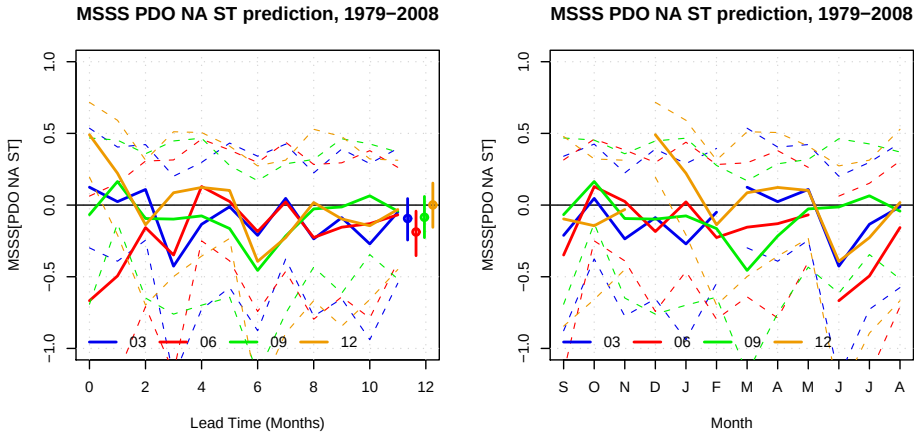

Figure A.12: MSSS (solid lines) and bootstrapped 95% confidence interval (dashed lines) between the predicted and the observed PDO influence on North American temperature index as a function of lead time where the dots, lines on the right show the mean, 95% confidence interval over the forecast range (left panel) and target month (right panel) for four different start months of the forecast (03: March; 06: June; 09: September; 12: December).

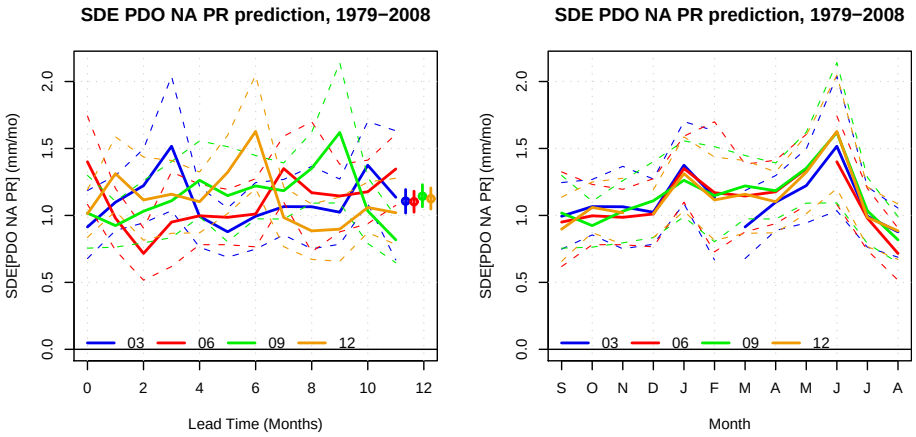

Figure A.13: SDE (solid lines) and bootstrapped 95% confidence interval (dashed lines) between the predicted and the observed PDO influence on North American precipitation index as a function of lead time where the dots, lines on the right show the mean, 95% confidence interval over the forecast range (left panel) and target month (right panel) for four different start months of the forecast (03: March; 06: June; 09: September; 12: December).

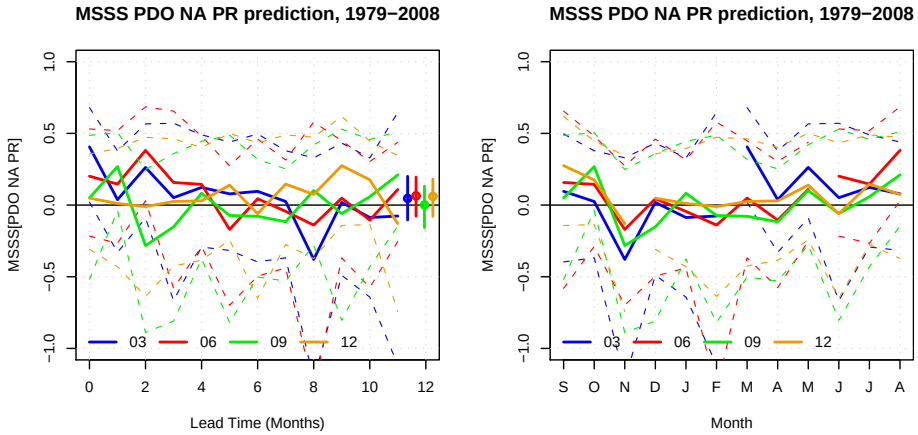

Figure A.14: MSSS (solid lines) and bootstrapped 95% confidence interval (dashed lines) between the predicted and the observed PDO influence on North American precipitation index as a function of lead time where the dots, lines on the right show the mean, 95% confidence interval over the forecast range (left panel) and target month (right panel) for four different start months of the forecast (03: March; 06: June; 09: September; 12: December).

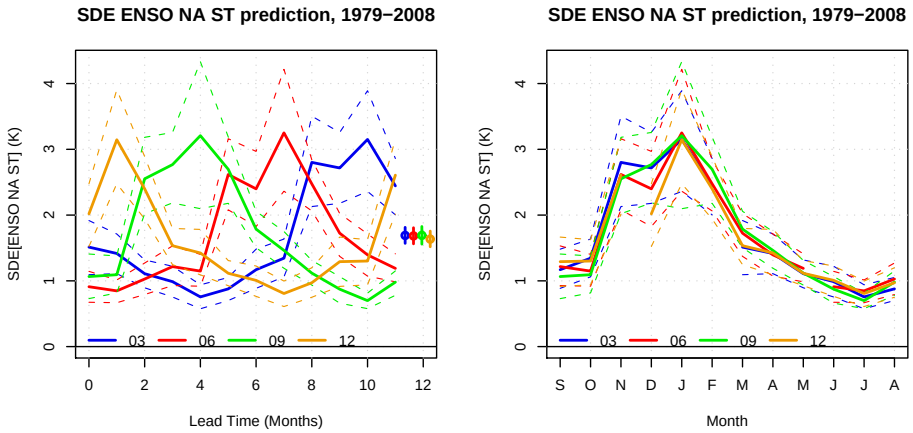

Figure A.15: SDE (solid lines) and bootstrapped 95% confidence interval (dashed lines) between the predicted and the observed ENSO influence on North American temperature index as a function of lead time where the dots, lines on the right show the mean, 95% confidence interval over the forecast range (left panel) and target month (right panel) for four different start months of the forecast (03: March; 06: June; 09: September; 12: December).

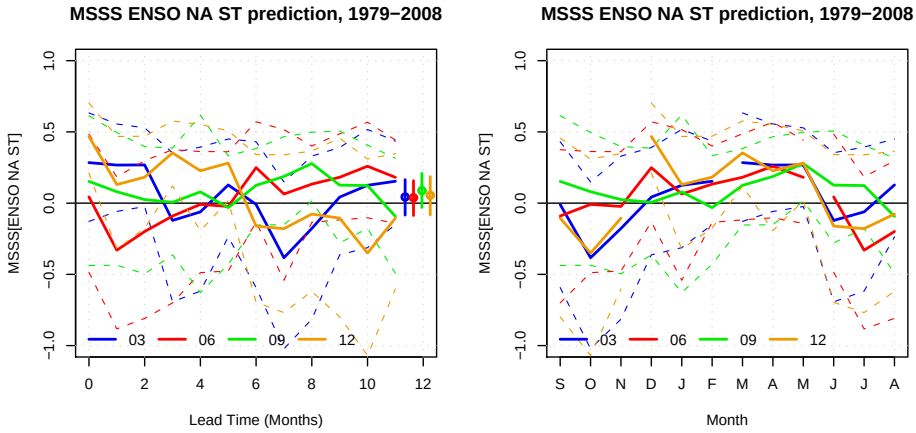

Figure A.16: MSSS (solid lines) and bootstrapped 95% confidence interval (dashed lines) between the predicted and the observed ENSO influence on North American temperature index as a function of lead time where the dots, lines on the right show the mean, 95% confidence interval over the forecast range (left panel) and target month (right panel) for four different start months of the forecast (03: March; 06: June; 09: September; 12: December).

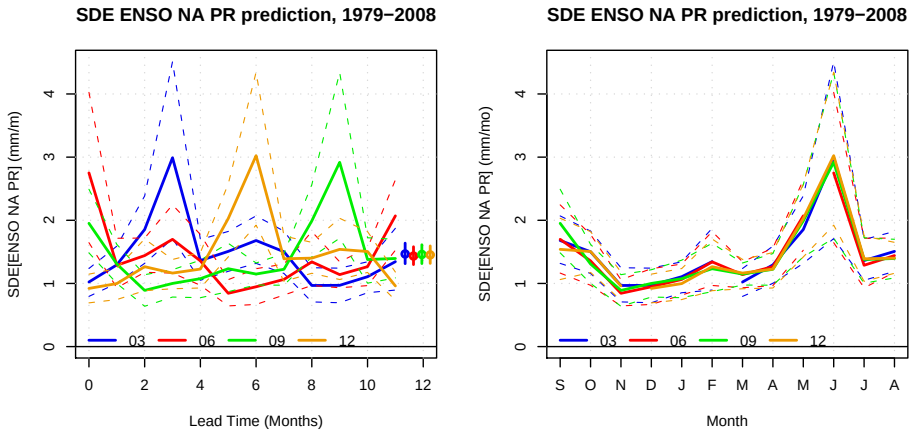

Figure A.17: SDE (solid lines) and bootstrapped 95% confidence interval (dashed lines) between the predicted and the observed ENSO influence on North American precipitation index as a function of lead time where the dots, lines on the right show the mean, 95% confidence interval over the forecast range (left panel) and target month (right panel) for four different start months of the forecast (03: March; 06: June; 09: September; 12: December).

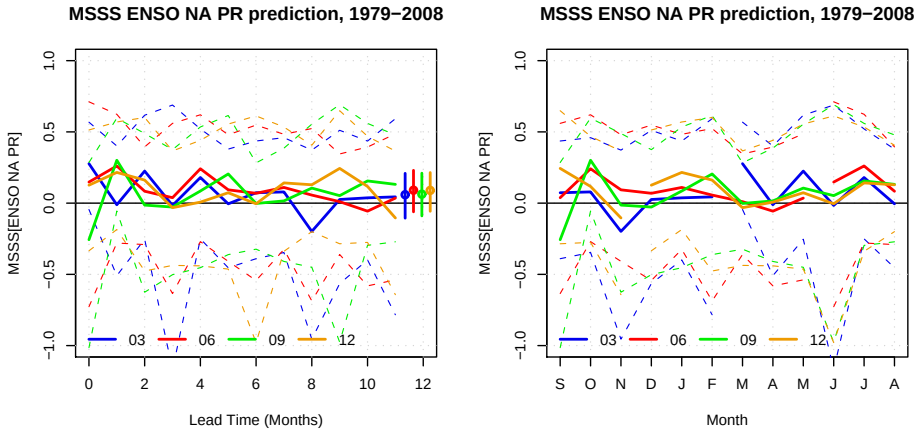

Figure A.18: MSSS (solid lines) and bootstrapped 95% confidence interval (dashed lines) between the predicted and the observed ENSO influence on North American precipitation index as a function of lead time where the dots, lines on the right show the mean, 95% confidence interval over the forecast range (left panel) and target month (right panel) for four different start months of the forecast (03: March; 06: June; 09: September; 12: December).

Bibliography

K. Achutarao and K. R. Sperber. ENSO simulation in coupled ocean-atmosphere models: are the current models better? *Climate Dynamics*, 27:1–15, 2006. doi: 10.1007/s00382-006-0119-7.

M. A. Alexander, C. Deser, and M. S. Timlin. The Reemergence of SST Anomalies in the North Pacific Ocean. *Journal of Climate*, 12:2419–2433, 1999.

M. A. Alexander, I. Bladé, M. Newman, J. R. Lanzante, N.-C. Lau, and J. D. Scott. The atmospheric bridge: The influence of enso teleconnections on air-sea interaction over the global oceans. *Journal of Climate*, 15:2205–2231, 2002.

T. R. Ault and S. St. George. The magnitude of decadal and multidecadal variability in north american precipitation. *Journal of Climate*, 23:842–850, 2010. doi: 10.1175/2009JCLI3013.1.

T. P. Barnett, M. Latif, E. Kirk, and E. Roeckner. On ENSO Physics. *Journal of Climate*, pages 487–516, 1991.

T. P. Barnett, D. W. Pierce, R. Saravanan, N. Schneider, D. Dommenget, and M. Latif. Origins of the midlatitude Pacific decadal variability. *Geophysical Research Letters*, 26:1453–1456, 1999. doi: 10.1029/1999GL900278.

F. Biondi, A. Gershunov, and D. R. Cayan. North pacific decadal climate variability since 1661. *Journal of Climate*, 14:5–10, 2001.

G. J. Boer. Long time-scale potential predictability in an ensemble of coupled climate models. *Climate Dynamics*, 23:29–44, 2004. doi: 10.1007/s00382-004-0419-8.

G. J. Boer. Decadal potential predictability of twenty-first century climate. *Climate Dynamics*, pages 1–15, 2010. doi: 10.1007/s00382-010-0747-9.

G. J. Boer and S. J. Lambert. Multi-model decadal potential predictability of precipitation and temperature. *Geophysical Research Letters*, 35:5706, 2008. doi: 10.1029/2008GL033234.

N. A. Bond, J. E. Overland, M. Spillane, and P. Stabeno. Recent shifts in the state of the North Pacific. *Geophysical Research Letters*, 30:2183, 2003.

D. R. Cayan, M. D. Dettinger, H. F. Diaz, and N. E. Graham. Decadal variability of precipitation over western north america. *Journal of Climate*, 11:3148–3166, 1998.

M. Christoph, U. Ulbrich, and P. Speth. Midwinter suppression of northern hemisphere storm track activity in the real atmosphere and in gcm experiments. *Journal of the Atmospheric Sciences*, 54:1589–1599, 1997.

C. Deser, A. S. Phillips, and M. A. Alexander. Twentieth century tropical sea surface temperature trends revisited. *Geophysical Research Letters*, 37:L10701, 2010.

E. Di Lorenzo, N. Schneider, K. M. Cobb, P. J. S. Franks, K. Chhak, A. J. Miller, J. C. McWilliams, S. J. Bograd, H. Arango, E. Curchitser, T. M. Powell, and P. Rivière. North Pacific Gyre Oscillation links ocean climate and ecosystem change. *Geophysical Research Letters*, 35:8607, 2008.

N. J. Dunstone and D. M. Smith. Impact of atmosphere and sub-surface ocean data on decadal climate prediction. *Geophysical Research Letters*, 37:2709, 2010. doi: 10.1029/2009GL041609.

C. Frankignoul and K. Hasselmann. Stochastic climate models, part II. Application to sea-surface temperature anomalies and thermocline variability. *Tellus*, 29:289–305, 1977.

J. C. Fyfe, N. P. Gillett, and D. W. J. Thompson. Comparing variability and trends in observed and modelled global-mean surface temperature. *Geophysical Research Letters*, 37:L16802, 2010.

S. T. Gray, J. L. Betancourt, C. L. Fastie, and S. T. Jackson. Patterns and sources of multidecadal oscillations in drought-sensitive tree-ring records from the central and southern rocky mountains. *Geophysical Research Letters*, 30(6):1316–, March 2003.

D. Gu and S. G. H. Philander. Interdecadal Climate Fluctuations That Depend on Exchanges Between the Tropics and Extratropics. *Science*, 275:805–807, 1997. doi: 10.1126/science.275.5301.805.

E. Guilyardi. El Niño mean state seasonal cycle interactions in a multi-model ensemble. *Climate Dynamics*, 26:329–348, 2006. doi: 10.1007/s00382-005-0084-6.

IPCC. *Climate Change 2007: The Physical Science Basis. Contribution of Working Group I to the Fourth Assessment Report of the Intergovernmental Panel on Climate Change.* Cambridge University Press, Cambridge, United Kingdom and New York, NY, USA., 2007.

E. Kalnay, M. Kanamitsu, R. Kistler, W. Collins, D. Deaven, L. Gandin, M. Iredell, S. Saha, G. White, J. Woollen, Y. Zhu, A. Leetmaa, B. Reynolds, M. Chelliah, W. Ebisuzaki, W. Higgins, J. Janowiak, K. C. Mo, C. Ropelewski, J. Wang, R. Jenne, and D. Joseph. The NCEP/NCAR 40-Year Reanalysis Project. *Bulletin of the American Meteorological Society*, 77:437–472, 1996.

A. B. Kara, P. A. Rochford, and H. E. Hurlburt. An optimal definition for ocean mixed layer depth. *Journal of Geophysical Research*, 105:16803–16822, 2000. doi: 10.1029/2000JC900072.

V. V. Kharin and F. W. Zwiers. Climate predictions with multimodel ensembles. *Journal of Climate*, 15:793–799, 2002.

M. Latif. On North Pacific Multidecadal Climate Variability. *Journal of Climate*, 19: 2906–2915, 2006. doi: 10.1175/JCLI3719.1.

M. Latif and T. P. Barnett. Causes of Decadal Climate Variability over the North Pacific and North America. *Science*, 266:634–637, 1994. doi: 10.1126/science.266.5185.634.

D. R. Legates and C. J. Willmott. Mean seasonal and spatial variability in gauge-corrected, global precipitation. *International Journal of Climatology*, 10:111–127, 1990. doi: 10.1002/joc.3370100202.

N. J. Mantua, S. R. Hare, Y. Zhang, J. M. Wallace, and R. C. Francis. A Pacific Interdecadal Climate Oscillation with Impacts on Salmon Production. *Bulletin of the American Meteorological Society*, 78:1069–1079, 1997.

G. J. McCabe, M. A. Palecki, and J. L. Betancourt. Pacific and Atlantic Ocean influences on multidecadal drought frequency in the United States. *Proceedings of the National Academy of Science*, 101:4136–4141, 2004.

G. A. Meehl and A. Hu. Megadroughts in the Indian Monsoon Region and Southwest North America and a Mechanism for Associated Multidecadal Pacific Sea Surface Temperature Anomalies. *Journal of Climate*, 19:1605–1623, 2006. doi: 10.1175/JCLI3675.1.

C. S. Meinen and M. J. McPhaden. Observations of Warm Water Volume Changes in the Equatorial Pacific and Their Relationship to El Niño and La Niña. *Journal of Climate*, 13:3551–3559, 2000.

W. J. Merryfield. Changes to ENSO under CO2 Doubling in a Multimodel Ensemble. *Journal of Climate*, 19:4009–4027, 2006. doi: 10.1175/JCLI3834.1.

W. J. Merryfield, W.-S. Lee, G. J. Boer, V. V. Kharin, B. Pal, J. F. Scinocca, and G. M. Flato. The first coupled historical forecasting project (chfp1). *Atmosphere-Ocean*, 48:263–283, 2010.

T. D. Mitchell and P. D. Jones. An improved method of constructing a database of monthly climate observations and associated high-resolution grids. *International Journal of Climatology*, 25:693–712, 2005.

A. H. Monahan, J. C. Fyfe, M. H. P. Ambaum, D. B. Stephenson, and G. R. North. Empirical orthogonal functions: The medium is the message. *Journal of Climate*, 22:6501–6514, 2009. doi: 10.1175/2009JCLI3062.1.

G. W. K. Moore, G. Holdsworth, and K. Alverson. Climate change in the north pacific region over the past three centuries. *Nature*, 420:401–403, 2002.

H. Nakamura. Midwinter suppression of baroclinic wave activity in the pacific. *Journal of the Atmospheric Sciences*, 49:1629–1642, 1992.

M. Newman. Interannual to decadal predictability of tropical and north pacific sea surface temperatures. *Journal of Climate*, 20:2333–2356, 2007. doi: 10.1175/JCLI4165.1.

M. Newman, G. P. Compo, and M. A. Alexander. ENSO-Forced Variability of the Pacific Decadal Oscillation. *Journal of Climate*, 16:3853–3857, 2003.

J. E. Overland, J. Alheit, A. Bakun, J. W. Hurrell, D. L. Mackas, and A.J. Miller. Climate controls on marine ecosystems and fish populations. *Journal of Marine Systems*, 79:305–315, 2010. doi: 10.1016/j.jmarsys.2008.12.009.

T. N. Palmer, F. J. Doblas-Reyes, R. Hagedorn, A. Alessandri, S. Gualdi, U. Andersen, H. Feddersen, P. Cantelaube, J-M. Terres, M. Davey, R. Graham, P. Délécluse, A. Lazar, M. Déqué, J-F. Guérémy, E. Díez, B. Orfila, M. Hoshen, A. P. Morse, N. Keenlyside, M. Latif, E. Maisonnave, P. Rogel, V. Marletto, and M. C. Thomson. Development of a european multi-model ensemble system for seasonal to interannual prediction (demeter). *Bulletin of the American Meteorological Society*, 85: 853–872, 2004. doi: 10.1175/BAMS-85-6-853.

S. Park, M. A. Alexander, and C. Deser. The impact of cloud radiative feedback, remote enso forcing, and entrainment on the persistence of north pacific sea surface temperature anomalies. *Journal of Climate*, 19(23):6243–6261, 2006.

V. Pavan and F. J. Doblas-Reyes. Multi-model seasonal hindcasts over the euro-atlantic: skill scores and dynamic features. *Climate Dynamics*, pages 611–625, 2000.

S. Penny, G. H. Roe, and D. S. Battisti. The source of the midwinter suppression in storminess over the north pacific. *Journal of Climate*, 23:634–648, 2010. doi: 10.1175/2009JCLI2904.1.

S. Power and R. Colman. Multi-year predictability in a coupled general circulation model. *Climate Dynamics*, 26:247–272, 2006. doi: 10.1007/s00382-005-0055-y.

S. Power, M. Haylock, R. Colman, and X. Wang. The predictability of interdecadal changes in enso activity and enso teleconnections. *Journal of Climate*, 19:4755–4771, 2006. doi: 10.1175/JCLI3868.1.

N. A. Rayner, D. E. Parker, E. B. Horton, C. K. Folland, L. V. Alexander, D. P. Rowell, E. C. Kent, and A. Kaplan. Global analyses of sea surface temperature, sea ice, and night marine air temperature since the late nineteenth century. *Journal of Geophysical Research (Atmospheres)*, 108:4407, 2003. doi: 10.1029/2002JD002670.

R. W. Reynolds, N. A. Rayner, T. M. Smith, D. C. Stokes, and W. Wang. An improved in situ and satellite sst analysis for climate. *Journal of Climate*, 15: 1609–1625, 2002.

D. P. Rowell. Assessing Potential Seasonal Predictability with an Ensemble of Multidecadal GCM Simulations. *Journal of Climate*, 11:109–120, 1998.

S. Saha, S. Nadiga, C. Thiaw, J. Wang, W. Wang, Q. Zhang, H. M. Van den Dool, H.-L. Pan, S. Moorthi, D. Behringer, D. Stokes, M. Pea, S. Lord, G. White, W. Ebisuzaki, P. Peng, and P. Xie. The ncep climate forecast system. *Journal of Climate*, 19:3483–3517, 2006. doi: 10.1175/JCLI3812.1.

N. Schneider and B. D. Cornuelle. The Forcing of the Pacific Decadal Oscillation. *Journal of Climate*, 18:4355–4373, 2005.

N. Schneider, A. J. Miller, M. A. Alexander, and C. Deser. Subduction of decadal north pacific temperature anomalies: Observations and dynamics. *Journal of Physical Oceanography*, 29:1056–1070, 1999.

F. B. Schwing, R. Mendelssohn, S. J. Bograd, J. E. Overland, M. Wang, and S. Ito. Climate change, teleconnection patterns, and regional processes forcing marine populations in the pacific. *Journal of Marine Systems*, 79:245–257, 2010. doi: 10.1016/j.jmarsys.2008.11.027.

J. D. Shakun and J. Shaman. Tropical origins of north and south pacific decadal variability. *Geophysical Research Letters*, 36:L19711, 2009.

D. M. Smith, S. Cusack, A. W. Colman, C. K. Folland, G. R. Harris, and J. M. Murphy. Improved Surface Temperature Prediction for the Coming Decade from a Global Climate Model. *Science*, 317:796–799, 2007. doi: 10.1126/science.1139540.

T. M. Smith, R. W. Reynolds, T. C. Peterson, and J. Lawrimore. Improvements to noaas historical merged landocean surface temperature analysis (1880–2006). *Journal of Climate*, 21:2283–2296, 2008. doi: 10.1175/2007JCLI2100.1.

M. Steele, R. Morley, and W. Ermold. Phc: A global ocean hydrography with a high-quality arctic ocean. *Journal of Climate*, 14:2079–2087, 2001.

C. Strong and G. Magnusdottir. The Role of Tropospheric Rossby Wave Breaking in the Pacific Decadal Oscillation. *Journal of Climate*, 22:1819–1833, 2009. doi: 10.1175/2008JCLI2593.1.

Y. Tang, R. Kleeman, A. M. Moore, J. Vialard, and A. Weaver. An off-line, numerically efficient initialization scheme in an oceanic general circulation model for el niño-southern oscillation prediction. *Journal of Geophysical Research*, 2004.

D. W. J. Thompson, J. M. Wallace, P. D. Jones, and J. J. Kennedy. Identifying signatures of natural climate variability in time series of global-mean surface temperature: Methodology and insights. *Journal of Climate*, 22(22):6120–6141, 2009.

K. E. Trenberth and J. W. Hurrell. Decadal atmosphere-ocean variations in the Pacific. *Climate Dynamics*, 9:303–319, 1994. doi: 10.1007/BF00204745.

K. E. Trenberth, G. W. Branstator, D. Karoly, A. Kumar, N.-C. Lau, and C. Ropelewski. Progress during TOGA in understanding and modeling global teleconnections associated with tropical sea surface temperatures. *Journal of Geophysical Research*, 103:14291–14324, 1998. doi: 10.1029/97JC01444.

A. Troccoli, M. A. Balmaseda, J. Segschneider, J. Vialard, D. L. T. Anderson, K. Haines, T. Stockdale, F. Vitart, and A. D. Fox. Salinity adjustments in the presence of temperature data assimilation. *Monthly Weather Review*, 130:89–102, 2002.

S. M. Uppala, P. W. KÅllberg, A. J. Simmons, U. Andrae, V. D. C. Bechtold, M. Fiorino, J. K. Gibson, J. Haseler, A. Hernandez, G. A. Kelly, X. Li, K. Onogi, S. Saarinen, N. Sokka, R. P. Allan, E. Andersson, K. Arpe, M. A. Balmaseda, A. C. M. Beljaars, L. V. D. Berg, J. Bidlot, N. Bormann, S. Caires, F. Chevallier, A. Dethof, M. Dragosavac, M. Fisher, M. Fuentes, S. Hagemann, E. Hólm, B. J. Hoskins, L. Isaksen, P. A. E. M. Janssen, R. Jenne, A. P. McNally, J.-F. Mahfouf, J.-J. Morcrette, N. A. Rayner, R. W. Saunders, P. Simon, A. Sterl, K. E. Trenberth, A. Untch, D. Vasiljevic, P. Viterbo, and J. Woollen. The ERA-40 re-analysis. *Quarterly Journal of the Royal Meteorological Society*, 131:2961–3012, 2005. doi: 10.1256/qj.04.176.

D. J. Vimont, D. S. Battisti, and A. C. Hirst. Footprinting: A seasonal connection between the tropics and mid-latitudes. *Geophysical Research Letters*, 28(20):3923–3926, 2001.

H. von Storch and F. W. Zwiers. *Statistical analysis in climate research*. Cambridge University Press, 1999.

J. M. Wallace and David S. Gutzler. Teleconnections in the geopotential height field during the northern hemisphere winter. *Monthly Weather Review*, pages 784–812, 1981.

B. Wang, R. Wu, and R. Lukas. Annual adjustment of the thermocline in the tropical pacific ocean. *Journal of Climate*, pages 596–616, 2000.

A. Weisheimer, F. J. Doblas-Reyes, T. N. Palmer, A. Alessandri, A. Arribas, M. Déqué, N. Keenlyside, M. MacVean, A. Navarra, and P. Rogel. ENSEMBLES: A new multi-model ensemble for seasonal-to-annual predictions - Skill and progress beyond DEMETER in forecasting tropical Pacific SSTs. *Geophysical Research Letters*, 36:21711, 2009. doi: 10.1029/2009GL040896.

S.-W. Yeh and B. P. Kirtman. The North Pacific Oscillation-ENSO and internal atmospheric variability. *Geophysical Research Letters*, 31:13206, 2004. doi: 10.1029/2004GL019983.

B. Yu and F. W. Zwiers. The impact of combined ENSO and PDO on the PNA climate: a 1,000-year climate modeling study. *Climate Dynamics*, 29:837–851, 2007. doi: 10.1007/s00382-007-0267-4.

B. Yu, G. Boer, F. Zwiers, and W. Merryfield. Covariability of sst and surface heat fluxes in reanalyses and cmip3 climate models. *Climate Dynamics*, pages 1–17, 2009. doi: 10.1007/s00382-009-0669-6.